



# Is a scaling factor required to obtain closure between measured and modelled atmospheric O<sub>4</sub> absorptions? - A case study for two days during the MADCAT campaign

Thomas Wagner<sup>1</sup>, Steffen Beirle<sup>1</sup>, Nuria Benavent<sup>2</sup>, Tim Bösch<sup>3</sup>, Kai Lok Chan<sup>4</sup>, Sebastian Donner<sup>1</sup>, Steffen Dörner<sup>1</sup>, Caroline Fayt<sup>5</sup>, Udo Frieß<sup>6</sup>, David García-Nieto<sup>2</sup>, Clio Gielen<sup>5\*</sup>, David González-Bartolomé<sup>7</sup>, Laura Gomez<sup>7</sup>, François Hendrick<sup>5</sup>, Bas Henzing<sup>8</sup>, Jun Li Jin<sup>9</sup>, Johannes Lampel<sup>6</sup>, Jianzhong Ma<sup>10</sup>, Kornelia Mies<sup>1</sup>, Mónica Navarro<sup>7</sup>, Enno Peters<sup>4\*\*</sup>, Gaia Pinardi<sup>5</sup>, Olga Puente-dura<sup>7</sup>, Janis Puķīte<sup>1</sup>, Julia Remmers<sup>1</sup>, Andreas Richter<sup>3</sup>, Alfonso Saiz-Lopez<sup>2</sup>, Reza Shaiganfar<sup>1</sup>, Holger Sihler<sup>1</sup>, Michel Van Roozendael<sup>5</sup>, Yang Wang<sup>1</sup>, Margarita Yela<sup>7</sup>

<sup>1</sup> Max Planck Institute for Chemistry, Mainz, Germany

<sup>2</sup> Department of Atmospheric Chemistry and Climate, Institute of Physical Chemistry Rocasolano (CSIC), Spain.

<sup>3</sup> University of Bremen, Germany

<sup>4</sup> Meteorological Institute, Ludwig-Maximilians-Universität München, Germany

<sup>5</sup> Royal Belgian Institute for Space Aeronomy (BIRA-IASB), Brussels, Belgium

<sup>6</sup> University of Heidelberg, Germany

<sup>7</sup> Instituto Nacional de Técnica Aeroespacial (INTA), Spain

<sup>8</sup> TNO, Netherlands Institute for Applied Scientific Research

<sup>9</sup> CMA Meteorological Observation Center, China

<sup>10</sup> Chinese Academy of Meteorological Science, China

\* currently at the Institute of Astronomy, KU Leuven, Belgium

\*\* Now at Institute for protection of maritime infrastructures, Bremerhaven, Germany

## Abstract

In this study the consistency between MAX-DOAS measurements and radiative transfer simulations of the atmospheric O<sub>4</sub> absorption is investigated on two mainly clear days during the MAD-CAT campaign in Mainz, Germany, in Summer 2013. In recent years several studies indicated that measurements and radiative transfer simulations of the atmospheric O<sub>4</sub> absorption can only be brought into agreement if a so-called scaling factor (<1) is applied to the measured O<sub>4</sub> absorption. However, many studies, in particular based on direct sun light measurements, came to the opposite conclusion, that there is no need for a scaling factor. Up to now, there is no explanation for the observed discrepancies between measurements and simulations. Previous studies inferred the need for a scaling factor from the comparison of the aerosol optical depth derived from MAX-DOAS O<sub>4</sub> measurements with that derived from coincident sun photometer measurements. In this study a different approach is chosen: the measured O<sub>4</sub> absorption at 360 nm is directly compared to the O<sub>4</sub> absorption obtained from radiative transfer simulations. The atmospheric conditions used as input for the radiative transfer simulations were taken from independent data sets, in particular from sun photometer and ceilometer measurements at the measurement site. The comparisons are performed for two selected clear days with similar aerosol optical depth but very different aerosol properties. For both days not only the O<sub>4</sub> absorptions are compared, but also all relevant error sources of the spectral analysis, the radiative transfer simulations as well as the extraction of the input parameters used for the radiative transfer simulations are quantified. One important result obtained from the analysis of synthetic spectra is that the O<sub>4</sub> absorptions derived from the



49 spectral analysis agree within 1% with the corresponding radiative transfer simulations. The  
50 performed tests and sensitivity studies might be useful for the analysis and interpretation of  
51 O<sub>4</sub> MAX-DOAS measurements in future studies.  
52 Different comparison results are found for both days: On 18 June, measurements and  
53 simulations agree within their (rather large) errors (the ratio of simulated and measured O<sub>4</sub>  
54 absorptions is found to be  $1.01 \pm 0.16$ ). In contrast, on 8 July measurements and simulations  
55 significantly disagree: For the middle period of that day the ratio of simulated and measured  
56 O<sub>4</sub> absorptions is found to be  $0.71 \pm 0.12$ , which differs significantly from unity. Thus for that  
57 day a scaling factor is needed to bring measurements and simulations into agreement. One  
58 possible reason for the comparison results on 18 June is the rather large aerosol extinction  
59 (and its large uncertainty) close to the surface, which has a large effect on the radiative  
60 transfer simulations. Besides the inconsistent comparison results for both days, also no  
61 explanation for a O<sub>4</sub> scaling factor could be derived in this study. Thus similar, but more  
62 extended future studies should be performed, which preferably include more measurement  
63 days, more instruments and should be supported by more detailed independent aerosol  
64 measurements. Also additional wavelengths should be included. The MAX-DOAS  
65 measurements collected during the recent CINDI-2 campaign are probably well suited for that  
66 purpose.

## 67 1 Introduction

68  
69 Observations of the atmospheric absorption of the oxygen collision complex (O<sub>2</sub>)<sub>2</sub> (in the  
70 following referred to as O<sub>4</sub>, see Greenblatt et al. (1990)) are often used to derive information  
71 about atmospheric light paths from remote sensing measurements of scattered sun light (made  
72 e.g. from ground, satellite, balloon or airplane). Since atmospheric radiative transport is  
73 strongly influenced by scattering on aerosol and cloud particles, information on the presence  
74 and properties of clouds and aerosols can be derived from O<sub>4</sub> absorption measurements.  
75 Early studies based on O<sub>4</sub> measurements focussed on the effect of clouds (e.g. Erle et al.,  
76 1995; Wagner et al., 1998; Winterrath et al., 1999; Acarreta et al., 2004; Snee et al., 2008;  
77 Heue et al., 2014; Gielen et al., 2014; Wagner et al., 2014), which is usually stronger than that  
78 of aerosols. Later also aerosol properties were derived from O<sub>4</sub> measurements, in particular  
79 from Multi-AXis- (MAX-) DOAS measurements (e.g. Hönninger et al., 2004; Wagner et al.,  
80 2004; Wittrock et al., 2004; Friess et al., 2004; Irie et al. Clémer 2010; Friess et al., 2016 and  
81 references therein). For the retrieval of aerosol profiles usually forward model simulations for  
82 various assumed aerosol profiles are compared to measured O<sub>4</sub> slant column densities (SCD,  
83 the integrated O<sub>4</sub> concentration along the atmospheric light path). The aerosol profile  
84 associated with the best fit between the forward model and measurement results is considered  
85 as the most probable atmospheric aerosol profile (for more details, see e.g. Frieß et al., 2006).  
86 Note that in some cases no unique solution might exist, if different atmospheric aerosol  
87 profiles lead to the same O<sub>4</sub> absorptions. MAX-DOAS aerosol retrievals are typically  
88 restricted to altitudes below about 4 km; see Friess et al. (2006).  
89 About ten years ago, Wagner et al. (2009) suggested to apply a scaling factor (SF <1) to the  
90 O<sub>4</sub> SCDs derived from MAX-DOAS measurements at 360 nm in Milano in order to achieve  
91 agreement with forward model simulations. They found that on a day with low aerosol load  
92 the measured O<sub>4</sub> SCDs were larger than the model results, even if no aerosols were included  
93 in the model simulations. If, however, the measured O<sub>4</sub> SCDs were scaled by a SF of 0.81,  
94 good agreement with the forward model simulations (and nearby AERONET measurements)  
95 was achieved. Similar findings were then reported by Clémer et al. (2010), who suggested a  
96 SF of 0.8 for MAX-DOAS measurements in Beijing. Interestingly, they applied this SF to  
97 four different O<sub>4</sub> absorption bands (360, 477, 577, and 630 nm).  
98



While with the application of a SF the consistency between forward model and measurements was substantially improved, both studies could not provide an explanation for the physical mechanism behind such a SF. In the following years several research groups applied a SF in their MAX-DOAS aerosol profile retrievals. However, a similarly large fraction of studies (including direct sun measurements and aircraft measurements, see Spinei et al. (2015)) did not find it necessary to apply a SF to bring measurements and forward model simulations into agreement. An overview on the application of a SF in various MAX-DOAS publications after 2010 is provided in Table 1. Up to now, there is no community consensus on whether or not a SF is needed for measured O<sub>4</sub> DSCDs. This is a rather unfortunate situation, because this ambiguity directly affects the aerosol results derived from MAX-DOAS measurements and thus the general confidence in the method.

So far, most of the studies deduced the need for a SF in a rather indirect way: aerosol extinction profiles derived from MAX-DOAS measurements using different SF are usually compared to independent data sets (mostly AOD from sun photometer observations) and the SF leading to the best agreement is selected. In many cases SF between 0.75 and 0.9 were derived.

In this study, we follow a different approach: similar to Ortega et al. (2016) we directly compare the measured O<sub>4</sub> SCDs with the corresponding SCDs derived from a forward model. For this comparison, atmospheric conditions which are well characterised by independent measurements are chosen. Such a procedure allows in particular quantifying the influence of the errors of the individual processing steps.

One peculiarity of this comparison is that the measured O<sub>4</sub> SCDs are first converted into their corresponding air mass factors (AMF), which are defined as the ratio of the SCD and the vertical column density (VCD, the vertically integrated concentration) (Solomon et al., 1987).

$$AMF = \frac{SCD}{VCD} \quad (1)$$

The ‘measured’ O<sub>4</sub> AMF is then compared to the corresponding AMF derived from radiative transfer simulations for the atmospheric conditions during the measurements:

$$AMF_{measured}^? = AMF_{simulated} \quad (2)$$

The conversion of the measured O<sub>4</sub> SCDs into AMFs is carried out to ensure a simple and direct comparison between measurements and forward model simulations. Here it should be noted that in addition to the AMFs also so-called differential AMFs (dAMFs) will be compared in this study. The dAMFs represent the difference between AMFs for measurements at non-zenith elevation angles  $\alpha$  and at 90° for the same elevation sequence:

$$dAMF_{\alpha} = AMF_{\alpha} - AMF_{90^{\circ}} \quad (3)$$

For the comparison between measured and simulated O<sub>4</sub> (d)AMFs, two mostly clear days (18 June and 08 July 2013) during the Multi Axis DOAS Comparison campaign for Aerosols and Trace gases (MADCAT) campaign are chosen ([http://joseba.mpch-mainz.mpg.de/mad\\_cat.htm](http://joseba.mpch-mainz.mpg.de/mad_cat.htm)). As discussed in more detail in section 4.2.2, based on the ceilometer and sun photometer measurements, three periods on each of both days are selected, during which the variation of the aerosol profiles was relatively small (see Table 2). In addition to the aerosol profiles, also other atmospheric properties are averaged during these periods before they are used as input for the radiative transfer simulations.



The comparison is carried out for the O<sub>4</sub> absorption band at 360 nm, which is the strongest O<sub>4</sub> absorption band in the UV. In principle also other O<sub>4</sub> absorption bands (e.g. in the visible spectral range) could be chosen, but these bands are not covered by the wavelength range of the MPIC instrument. Thus they are not part of this study.

Deviations between forward model and measurements can have different reasons: In the following an overview on these error sources and the way they are investigated in this study are given:

a) Calculation of O<sub>4</sub> profiles and O<sub>4</sub> VCDs (eq. 1):

Profiles and VCDs of O<sub>4</sub> are derived from pressure and temperature profiles. The errors of the pressure and temperature profiles are quantified by sensitivity studies and by the comparison of the extraction results derived from different groups/persons (see Table 3).

b) Calculation of O<sub>4</sub> (d)AMFs from radiative transfer simulations:

Besides differences between the different radiative transfer codes, the dominating error sources are the uncertainties of the input parameters. They are investigated by sensitivity studies and by the comparison of extracted input data by different groups/persons. Also the effects of operating different radiative transfer models by different groups are investigated.

c) Analysis of the O<sub>4</sub> (d)AMFs from MAX-DOAS measurements:

Uncertainties of the spectral analysis results are caused by errors and imperfections of the measurements/instruments, by the dependence of the analysis results on the specific fit settings, and the uncertainties of the O<sub>4</sub> cross sections. They are investigated by systematic variation of the DOAS fit settings (for measured and synthetic spectra), and by comparison of analysis results obtained from different groups and/or instruments.

The paper is organised as follows: in section 2, information on the selected days during the MADCAT campaign, on the MAX-DOAS measurements, and on the data sets from independent measurements is provided. Section 3 presents initial comparison results for the selected days using standard settings. In section 4 the uncertainties associated with each of the various processing steps of the spectral analysis and the forward model simulations are quantified. Section 5 presents a summary and conclusions.

## 2 MADCAT campaign, MAX-DOAS instruments and other data sets used in this study

The Multi Axis DOAS Comparison campaign for Aerosols and Trace gases (MADCAT) ([http://joseba.mpch-mainz.mpg.de/mad\\_cat.htm](http://joseba.mpch-mainz.mpg.de/mad_cat.htm)) took place in June and July 2013 on the roof of the Max-Planck-Institute for Chemistry in Mainz, Germany. The main aim of the campaign was to compare MAX-DOAS retrieval results of several atmospheric trace gases like NO<sub>2</sub>, HCHO, HONO, CHOCHO as well as aerosols. The measurement location was at 150m above sea level at the western edge of the city of Mainz.

### 2.1 MAX-DOAS instruments

During the MADCAT campaign, 11 MAX-DOAS instruments were operated by different groups; an overview can be found at the website <http://joseba.mpch-mainz.mpg.de/equipment.htm>. The main viewing direction of the MAX-DOAS instruments was towards north-west (51° with respect to North). Measurements at this viewing direction were the main focus of this study, but a few comparisons using the ‘standard settings’ (see section 3) were also carried out for three other azimuth angles (141°, 231°, 321°, see Fig. A2 I in appendix A1). Each elevation sequence contains the following elevation angles: 1, 2, 3, 4, 5, 6, 8, 10, 15, 30 and 90°. In this study, in addition to the MPIC instrument, also spectra from 3 other MAX-DOAS instruments were analysed. The instrumental details are given in Table



4. The spectra of the MPIC instrument are available at the website [http://joseba.mpch-mainz.mpg.de/e\\_doc\\_zip.htm](http://joseba.mpch-mainz.mpg.de/e_doc_zip.htm).

## 2.2 Additional data sets

In order to constrain the radiative transfer simulations, independent measurements and data sets were used. In particular, information on atmospheric pressure, temperature and relative humidity, as well as aerosol properties is used. In addition to local in situ measurements from air quality monitoring stations and remote sensing measurements by a ceilometer and a sun photometer, also ECMWF reanalysis data were used. An overview on these data sets is given in Table 5. The data sets used in this study are available at the websites [http://joseba.mpch-mainz.mpg.de/a\\_doc\\_zip.htm](http://joseba.mpch-mainz.mpg.de/a_doc_zip.htm) and [http://joseba.mpch-mainz.mpg.de/c\\_doc\\_zip.htm](http://joseba.mpch-mainz.mpg.de/c_doc_zip.htm).

## 2.3 RTM simulations

Several radiative transfer models are used to calculate  $O_4$  (d)AMFs for the selected days. As input, vertical profiles of temperature, pressure, relative humidity and aerosol extinction extracted from the independent data sets (see section 2.2 and 4) were used. The vertical resolution is high in the lowest layers and decreases with increasing altitude (see Table A1 in appendix A1). The upper boundary of the vertical grid is set to 1000 km. The lower boundary of the model grid represents the surface elevation of the instrument (150 m above sea level). For the ‘standard run’, a surface albedo of 5% is assumed and the aerosol optical properties are described by a Henyey-Greenstein phase function with an asymmetry parameter of 0.68 and a single scattering albedo of 0.95. Both values represent typical urban aerosols (see e.g. Dubovik et al., 2002). Ozone absorption was not considered, because it is very small at 360 nm. The MADCAT campaign took place around summer solstice. Thus the same dependence of the solar zenith angle (SZA) and relative azimuth angle (RAZI) on time is used for both days (see Table A2 in the appendix A1). The input data used for the radiative transfer simulations are available at the website [http://joseba.mpch-mainz.mpg.de/d\\_doc\\_zip.htm](http://joseba.mpch-mainz.mpg.de/d_doc_zip.htm). In the following sub-sections the different radiative transfer models used in this study are described.

### 2.3.1 MCARTIM

The full spherical Monte Carlo radiative transfer model MCARTIM (Deutschmann et al., 2011) explicitly simulates individual photon trajectories including the photon interactions with molecules, aerosol particles and the surface. In this study two versions of MCARTIM are used: version 1 and version 3. Version 1 is a 1-D scalar model. Version 3 can also be run in 3-D and vector modes. In version 1 Rotational Raman scattering (RRS) is partly taken into account: the RRS cross section and phase function are explicitly considered for the determination of the photon paths, but the wavelength redistribution during the RRS events is not considered. In version 3 RRS can be fully taken into account. If operated in the same mode (1-D scalar) both models show excellent agreement.

### 2.3.2 LIDORT

Linearized Discrete Ordinate Radiative Transfer (LIDORT) forward model (Spurr et al., 2001; Spurr et al., 2008) is based on the discrete ordinate method to solve the radiative transfer equation (e.g.: Chandrasekhar, 1960; Chandrasekhar, 1989; Stamnes et al., 1988).





This model considers a pseudo-spherical multi-layered atmosphere including several anisotropic scatters. The formulation implemented corrects for the atmosphere curvature in the solar and single scattered beam, however the multiple scattering term is treated in the plane-parallel approximation. The properties of each of the atmospheric layers are considered homogenous in the corresponding layer. Using finite differences for the altitude derivatives, this linearized code converts the problem into a linear algebraic system. Through first order perturbation theory, it is able to provide radiance field and radiance derivatives with respect to atmospheric and surface variables (Jacobians) in a single call. LIDORT was used in several studies to derive vertical profiles of aerosols and trace gases from MAX-DOAS (e.g. Clémer et al., 2010; Hendrick et al., 2014; Franco et al., 2015).

### 2.3.3 SCIATRAN

The RTM SCIATRAN (Rozanov et al. 2014) was used in its full-spherical mode including multiple scattering but without polarization. In the operation mode used here, SCIATRAN solves the transfer equations using the discrete ordinate method. In this study, SCIATRAN was used by two groups: The IUP Bremen group used v3.8.3 for the for the O<sub>4</sub> dAMFs simulations (without Raman scattering). The MPIC group used v3.6.11 for the calculation of synthetic spectra (see Section 2.4) and for the O<sub>4</sub> dAMFs simulations (including Raman scattering).

## 2.4 Synthetic spectra

In addition to AMFs and dAMFs, also synthetic spectra were simulated. They are analysed in the same way as the measured spectra, which allows the investigation of two important aspects:

a) The derived O<sub>4</sub> dAMFs from the synthetic spectra can be compared to the O<sub>4</sub> dAMFs obtained directly from the radiative simulations using the same settings. In this way the consistency of the spectral analysis results and the radiative transfer simulations is tested.

b) Sensitivity tests can be performed varying several fit parameters, e.g. the spectral range or the DOAS polynomial, and their effect on the derived O<sub>4</sub> dAMFs can be assessed.

Synthetic spectra are simulated using SCIATRAN taking into account rotational Raman scattering. The basic simulation settings are the same as for the RTM simulations of the O<sub>4</sub> (d)AMFs described above. In order to minimise the computational effort, for the profiles of temperature, pressure, relative humidity and aerosol extinction the input data for only two periods (18 June: 11:00 – 14:00, 08 July: 7:00 – 11:00, see Table 2) are used for the whole. Thus ‘perfect’ agreement with the measurements can only be expected for the two selected periods. Aerosol optical properties (phase function and single scattering albedo) are taken from AERONET measurements of the two selected days. Although the wavelength dependencies of both quantities (and also for the aerosol extinction) are considered, it should be noted that the associated uncertainties are probably rather large, since the optical properties in the UV had to be extrapolated from measurements in the visible spectral range. Moreover, the phase functions were not available as fully consolidated AERONET level 2.0 data, but only as level 1.5 data.

Spectra were simulated at a spectral resolution of 0.01 nm and convolved with a Gaussian slit function of 0.6 nm full width at half maximum (FWHM), which is similar to those of the measurements. For the generation of the spectra the trace gas absorptions of O<sub>3</sub>, NO<sub>2</sub>, HCHO, and O<sub>4</sub> are considered (see Table A3 in appendix A1). The assumed tropospheric profiles of NO<sub>2</sub> and HCHO are similar to those retrieved from the MAX-DOAS observations during the



selected periods. Time series of the tropospheric VCDs of NO<sub>2</sub> and HCHO for the two selected days are shown in Fig. A1 in appendix 1. Two sets of synthetic spectra were simulated, one taking into account the temperature dependence of the O<sub>4</sub> cross section and the other not. For the case without considering the temperature dependence the O<sub>4</sub> cross section for 293 K is used. In addition to spectra without noise, also spectra with noise (sigma of the noise is assumed as  $7.5 \cdot 10^{-4}$  times the intensity) were simulated. The synthetic spectra are available at the website [http://joseba.mpch-mainz.mpg.de/f\\_doc\\_zip.htm](http://joseba.mpch-mainz.mpg.de/f_doc_zip.htm).

### 3 Strategies used in this studies and comparison results for ‘standard settings’

#### 3.1 Selection of days

For the comparison of measured and simulated O<sub>4</sub> dAMFs, two mostly clear days during the MADCAT campaign (18 June and 8 July 2013) were selected. On both days the AOD measured by the AERONET sun photometer at 360 nm is between 0.25 and 0.4 (see Fig. 1). In spite of the similar AOD, very different aerosol properties at the surface are found on the two days: on 18 June much higher concentrations of large aerosol particles (PM<sub>2.5</sub> and PM<sub>10</sub>) are found. These differences are also represented by the large differences of the Ångström parameter for long wavelengths (440 – 870 nm) on both days. Also the aerosol height profiles are different: On 8 July rather homogenous profiles with a layer height of about 2 km occur. On 18 June the aerosol profiles reach to higher altitudes, but the highest extinction is found close to the surface. Also the temporal variability of the aerosol properties, especially the near-surface concentrations, is much larger on 18 June.

#### 3.2 Different levels of comparisons

The comparison between the forward model and MAX-DOAS measurements is performed in different depth for different subsets of the measurements:

- a) A quantitative comparison of O<sub>4</sub> AMFs and O<sub>4</sub> dAMFs is performed for 3° elevation angle at the standard viewing direction (51° with respect to North) for the middle periods of both selected days. During these periods the uncertainties of the measurement and the radiative transfer simulations are smallest. These comparisons thus constitute the core of the comparison exercise and all sensitivity studies are performed for these two periods. The elevation angle of 3° is selected because for such a low elevation angle the atmospheric light paths and thus the O<sub>4</sub> absorption are rather large. Moreover, as can be seen in Fig. 2, the O<sub>4</sub> (d)AMFs for 3° are very similar to those for 1° and 6°, especially on 8 July 2013. This finding indicates that possible uncertainties of the calibration of the elevation angles of the instruments can be neglected. Here it is interesting to note that on 18 June even slightly lower O<sub>4</sub> (d)AMFs are found for the low elevation angles. This is in agreement with the finding of high aerosol extinction in a shallow layer above the surface (see Fig. 1). The azimuth angle of 51° is chosen, because it was the standard viewing direction during the MADCAT campaign and measurements for this direction are available from different instruments.
- b) The quantitative comparison for 3° elevation and azimuth of 51° is also extended to the periods prior and after the middle periods of the selected days. However, to minimise the computational efforts, some sensitivity studies are not carried out for the first and last periods.
- c) The comparison is extended to more elevation angles (1°, 3°, 6°, 10°, 15°, 30°, 90°) and azimuth angles (51°, 141°, 231°, 321°). For this comparison only the standard settings for the DOAS analysis and the radiative transfer simulations are applied (see Tables 6 and 7). The comparison results for the MPIC MAX-DOAS measurements are shown in appendix A2. The



purpose of this comparison is to check whether for other viewing angles similar results are found as for  $3^\circ$  elevation at  $51^\circ$  azimuth direction.

### 3.3 Quantitative comparison for $3^\circ$ elevation in standard azimuth direction

Fig. 3 presents a comparison of the measured and simulated  $O_4$  (d)AMFs for  $3^\circ$  elevation and  $51^\circ$  azimuth on both days. For the spectral analysis and the radiative transfer simulations the respective ‘standard settings’ (see Tables 6 and 7) were used. On 8 July the simulated  $O_4$  (d)AMFs systematically underestimate the measured  $O_4$  (d)AMFs by up to 40%. Similar results are also obtained for other elevation and azimuth angles (see appendix A1), the differences becoming smaller towards higher elevation angles. In contrast, no systematic underestimation is observed for most of 18 June. For some periods of that day the simulated  $O_4$  (d)AMFs are even larger than the measured  $O_4$  (d)AMFs. However, here it should be noted that the aerosol extinction profile of the ‘standard settings’ (using linear extrapolation below 180 m where no ceilometer data are available) probably underestimates the aerosol extinction close to the surface. If instead a modified aerosol profile with strongly increased aerosol extinction below 180 m and the maximum AOD during that period is used (see Fig. A31 in appendix A5) the corresponding (d)AMFs fall below the measured  $O_4$  (d)AMFs (green curves in Fig. A4 in appendix A2). More details on the extraction of the aerosol extinction profiles are given in section 4.2.2 and appendix A5).

The average ratio of simulated to measured (d)AMFs (for the standard settings) during the middle periods on both days are given in Table 8. For 18 June they are close to unity, for 8 July they are much lower (0.83 for the AMF, and 0.69 for the dAMF).

## 4 Estimation of the uncertainties of the different processing steps

There are 3 major processing steps, for which the uncertainties are quantified in this section:

- a) The determination of the  $O_4$  height profiles and corresponding  $O_4$  vertical column densities.
- b) The simulation of  $O_4$  (d)AMFs by the forward model
- c) The analysis of  $O_4$  (d)AMFs from the MAX-DOAS measurements.

### 4.1 Determination of the vertical $O_4$ profile and the $O_4$ VCD

The  $O_4$  VCD is required for conversion of measured (d)SCDs into (d)AMFs (eq. 1). The accuracy of the calculated  $O_4$  height profile and the  $O_4$  VCD depends in particular on two aspects:

- a) is profile information on temperature, pressure and (relative) humidity available?
- b) what is the accuracy of these data sets?

Additional uncertainties are related to the details of the calculation of the  $O_4$  concentration and  $O_4$  VCDs from these profiles. Both error sources are investigated in the following sub sections.

#### 4.1.1 Extraction of vertical profiles of temperature and pressure

For the two selected days during the MADCAT campaign two data sets of temperature and pressure are available: surface measurements close to the measurement site and vertical profiles from ECMWF ERA-Interim re-analysis data (see Table 5). Both data sets are used to derive the  $O_4$  concentration profiles for the three selected periods on both days. The general procedure is that first the temperature profiles are determined. In a second step, the pressure





profiles are derived from the temperature profiles and the measured surface pressure. For the temperature profile extraction, three height layers are treated differently:

-below 1 km

Between the surface (~150 m above sea level) and 1 km, the temperature is linearly interpolated between the average of the in situ measurements of the respective period and the ECMWF data at 1 km (see next paragraph). This procedure is used to account for the diurnal variation of the temperature close to the surface. Here it is important to note that for this surface-near layer the highest accuracy is required, because a) the maximum  $O_4$  concentration is located near the surface, and b) the MAX-DOAS measurements are most sensitive close to the surface.

-1 km to 20 km

In this altitude range, the diurnal variation of the temperature becomes very small. Thus the average of the four ECMWF profiles of each day is used (for simplicity, a 6<sup>th</sup> order polynomial is fitted to the ECMWF data).

-Above 20 km

In this altitude range the accuracy of the temperature profile is not critical and thus the ECMWF temperature profile for 00:00 UTC of the respective day is used for simplicity.

The temperature profiles for 8 July 2013 extracted in this way are shown in Fig. 4 (left). Close to the surface the temperature variation during the day is about 10 K.

In the next step, the pressure profiles are determined from the surface pressure (obtained from the in situ measurements) and the extracted temperature profiles according to the ideal gas law. In principle the effect of atmospheric humidity could also be taken into account, but the effect is very small for surface-near layers and is thus ignored here. The derived pressure profiles for 8 July 2013 are shown in Fig. 4 (right). Excellent agreement with the corresponding ECMWF pressure profiles is found.

Here it should be noted that in principle also the ECMWF pressure profiles could be used. However, we chose to determine the pressure profiles from the surface pressure and the extracted temperature profiles, because this procedure can also be applied if no ECMWF data (or other information on temperature and pressure profiles) is available.

If no profile data (e.g. from ECMWF) are available, temperature and pressure profiles can also be extrapolated from surface measurements e.g. by assuming a constant lapse rate of -0.65 K / 100 m for the altitude range between the surface and 12 km, and a constant temperature above 12 km (as stated above, uncertainties at this altitude range have only a negligible effect on the  $O_4$  VCD). If no measurements or model data are available at all, a fixed temperature and pressure profile can be used, e.g. the US standard atmosphere (United States Committee on Extension to the Standard Atmosphere, 1976).

A comparison of the different temperature profiles for two selected periods on both days is shown in Fig. 5. For 8 July (right), rather good agreement is found, but for 18 June (left) the agreement is worse (differences up to 20 K). Of course, the differences between the true and the US standard atmosphere profiles can become even larger, depending on location and season. So the use of a fixed temperature and pressure profile should always be the last choice. In contrast, the simple extrapolation from surface values can be very useful if no profile data are available, because the uncertainties of this method are usually smallest at low altitudes, where the bulk of  $O_4$  is located.

#### 4.1.2 Calculation of $O_4$ concentration profiles and $O_4$ VCDs

From the temperature and pressure profiles the oxygen ( $O_2$ ) concentration is calculated. Here also the effect of the atmospheric humidity profiles should be taken into account (see below), because it can have a considerable effect on the surface-near layers. Finally, the square of the oxygen concentration is calculated and used as proxy for the  $O_4$  concentration (see Greenblatt



et al., 1990). The uncertainties of the derived  $O_4$  concentration (and the corresponding  $O_4$  VCD) caused by the uncertainty of the input profiles is estimated by varying the input parameters. The following uncertainties are derived:

- The variation of the temperature (whole profile) by about 2K leads to variations of the  $O_4$  concentration (or  $O_4$  VCD) by about 0.8%.
- The variation of the surface pressure by about 3 hPa leads to variations of the  $O_4$  concentration (or  $O_4$  VCD) by about 0.7%.
- The effect of uncertainties of the relative humidity depends strongly on temperature: For surface temperatures of 0°C, 10°C, 20°C, 30°C, and 35°C a variation of the relative humidity of 30% leads to variations of the  $O_4$  concentration (or  $O_4$  VCDs) of about 0.15%, 0.3%, 0.6%, 1.2%, and 1.6%, respectively. If the effect of atmospheric humidity is completely ignored (dry air is assumed), the resulting  $O_4$  concentrations (or  $O_4$  VCDs) are systematically overestimated by about 0.3%, 0.7%, 1.3%, 2.5%, and 4% for surface temperatures of 0°C, 10°C, 20°C, 30°C, and 35°C, respectively (assuming a relative humidity of 70%). In this study we used the relative humidity measured by the in situ sensors. We took these values not only for the surface layers, but also for the whole troposphere. Here it should be noted that the related uncertainties of the absolute humidity decrease quickly with altitude because the absolute humidity itself decrease quickly with altitude. Since both selected days were warm or even hot summer days, we estimate the uncertainty of the  $O_4$  concentration and  $O_4$  VCDs due to uncertainties of the relative humidity to 1% and 0.4% on 18 June and 8 July, respectively. Assuming that the uncertainties of the three input parameters are independent, the total uncertainty related to these factors is estimated to be about 1.5%.

Further uncertainties arise from the procedure of the vertical integration of the  $O_4$  concentration profiles. We tested the effect of using different vertical grids and altitude ranges. It is found that the vertical grid should not be coarser than 100 m (for which a deviation of the  $O_4$  VCD of 0.3% compared to a much finer grid is found). If e.g. a vertical grid with 500 m layers is used, the deviation increases to about 1.3%. The integration should be performed over an altitude range up to 30 km. If lower maximum altitudes are used, the  $O_4$  VCD will be substantially underestimated: deviations of 0.1 %, 0.5 %, and 11% are found if the integration is performed only up to 25 km, 20 km, and 10 km, respectively. Here it should be noted that the exact consideration of the altitude of the measurement site is also very important: A deviation of 50 m already leads to a change of the  $O_4$  VCD by 1%. For the MADCAT measurements the altitude of the instruments is  $150\text{m} \pm 20\text{m}$ .

Finally, the effects of individual extraction and integration procedures are investigated by comparing the results from different groups (see Fig. 6, and Fig. A5 in appendix A3). Except for some extreme cases, the extracted temperatures typically differ by less than 3 K below 10 km. However, the deviations are typically larger for the profiles extrapolated from the surface values and in particular for the US standard atmosphere (up to > 10 K below 10 km). Also the variations of the extracted pressure profiles are in general rather small (< 1% below 10 km, except one obvious outlier). Also here the deviations of the profiles extrapolated from the surface values and especially the US standard atmosphere are much larger (up to > 5 % below 10 km). The resulting deviations of the  $O_4$  concentration from the different extractions are typically <3% below 10 km (and up to > 20 % below 10 km for the US standard atmosphere). In Fig. 7 the  $O_4$  VCDs calculated for the  $O_4$  profiles extracted from the different groups and for the profiles extrapolated from the surface values and the US standard atmosphere are shown. The VCDs for the profiles extracted by the different groups agree within 2.5%. The deviations for the profiles extrapolated from the surface values are only slightly larger (typically within 3%), but show a large variability throughout the day, which is caused by the systematic increase of the surface temperature during the day (with temperature inversions in the morning on the two selected days). The deviations of the US standard atmosphere are up to 5% (but can of course be larger for other seasons and locations).



Together with the uncertainties related to the input data sets, the total uncertainty of the O<sub>4</sub> VCDs determined for both selected days is estimated as 3%.

## 4.2 Uncertainties of the O<sub>4</sub> (d)AMFs derived from radiative transfer simulations

The most important errors of the simulated O<sub>4</sub> (d)AMFs are related to the uncertainties of the input parameters used for the simulations, in particular the aerosol properties. Further uncertainties are caused by imperfections of the radiative transfer models. These error sources are discussed and quantified in the following sub sections.

### 4.2.1 Uncertainties of the O<sub>4</sub> (d)AMFs caused by uncertainties of the input parameters

In this section the effect of the uncertainties of various input parameters on the O<sub>4</sub> (d)AMFs is investigated. The general procedure is that the input parameters are varied individually and the corresponding changes of the O<sub>4</sub> (d)AMFs compared to the standard settings are quantified.

First, the effect of the O<sub>4</sub> profile shape is investigated. In contrast to the effect of the (absolute) profile shape on the O<sub>4</sub> VCD (section 4.1), here the effect of the relative profile shape on the O<sub>4</sub> AMF is investigated. The O<sub>4</sub> (d)AMFs simulated for the O<sub>4</sub> profiles extracted by the different groups (and for those derived from the US standard atmosphere and the profiles extrapolated from the surface values, see section 4.1) are compared to those for the MPIC O<sub>4</sub> profiles (using the standard settings). The corresponding ratios are shown in Fig. A6 and Table A4 in appendix A4. For the O<sub>4</sub> profiles extracted by the different groups, and for O<sub>4</sub> profiles extrapolated from the surface values, small variations are found (typically < 2%). For the O<sub>4</sub> standard atmosphere larger deviations (up to 7%) are derived.

Next the effect of the aerosol extinction profile is investigated. In this study, aerosol extinction profiles are derived from the combined ceilometer and sun photometer measurements (see Table 5). In short, the ceilometer measurements of the attenuated backscatter are scaled by the simultaneously measured aerosol optical depth (AOD) from the sun photometer to obtain the aerosol extinction profile. Also the self-attenuation of the aerosol is taken into account. The different steps are illustrated in Fig. 8 and described in detail in appendix A5. In the extraction procedure, several assumptions have to be made: First, the ceilometer profiles have to be extrapolated for altitudes below 180 m, for which the ceilometer is not sensitive. Furthermore, they have to be averaged over several hours and are in addition vertically smoothed (above 2 km) to minimise the rather large scatter. Finally, above 5 to 6 km (depending on the ceilometer profiles) the extinction is set to zero because of the further increasing scatter and the usually small extinctions. Another assumption is that the LIDAR ratio is independent of altitude, which is typically not strictly fulfilled (the LIDAR ratio describes the ratio between the extinction and backscatter probabilities of the molecules and aerosol particles).

Some of these uncertainties are quantified by sensitivity studies, in particular the effect of the extrapolation below 180 m and the altitude above which the aerosol extinction is set to zero. Other uncertainties, like the effect of the assumption of a constant LIDAR ratio are more difficult to quantify without further information. While a constant LIDAR ratio is probably a good assumption for 8 July, for 18 June the surface measurements indicate that the aerosol properties strongly change with time. Thus the LIDAR ratio might also vary stronger with altitude on that day. The effect of temporal averaging and smoothing is probably negligible for 8 July, because similar height profiles are found for all three periods of that day, but on 18 June the effect might be more important.

Fig. 9 shows a comparison of the aerosol extinction profiles extracted by the different groups for the three periods on both days. Especially on 8 July systematic differences are found.



They are caused by the different altitudes, above which the aerosol extinction is set to zero. In combination with the scaling of the profiles with the AOD obtained from the sun photometer, this also influences the extinction values close to the surface. Deviations up to 18% are found for the first period of 8 July. These deviations also have an effect on the corresponding  $O_4$  (d)AMFs, where higher values are obtained for the profiles (INTA and IUPB 300m) which were extracted for a larger altitude range (Fig. A7 and Table A5 in the appendix A4). Here it is interesting to note that these differences are not related to the direct effect of the aerosol extinction at high altitude, but to the corresponding (via the scaling with the AOD) decrease of the aerosol extinction close to the surface. Larger deviations (up to 4%) are found for 8 July, while the deviations on 18 June are within 3%.

In Fig. A8 and Table A6 in appendix A4, the effect of the different extrapolations of the aerosol extinction profile below 180 m on the  $O_4$  (d)AMFs is quantified. Similar deviations (up to 5 %) are found for both days.

In Fig. A9 and Table A7 in appendix A4, the effect of different single scattering albedos (between 0.9 and 1) on the  $O_4$  (d)AMFs is quantified. The effect on the  $O_4$  (d)AMFs is up 4 % on 18 June and up to 2 % on 8 July 2013.

The impact of the aerosol phase function is investigated in two ways: First, simulation results are compared for Henyey Greenstein phase functions with different asymmetry parameters. The corresponding results are shown in Fig. A10 and Table A8 in appendix A4. The differences of the  $O_4$  (d)AMFs for the different aerosol phase functions are rather strong: up to 3% for the  $O_4$  AMFs and up to 8% for the  $O_4$  dAMFs (larger uncertainties for the dAMFs are found because of the strong influence of the phase function on the 90° observations). Here it should be noted that the actual deviations from the true phase function might be even larger.

In order to better estimate these uncertainties, also simulations for phase functions derived from the sun photometer measurements based on Mie theory (in the following referred to as Mie phase functions) were performed. A comparison of these Mie phase functions with the Henyey Greenstein phase functions is shown in Fig. 10. Large differences, especially in forward direction are obvious. The  $O_4$  (d)AMFs for the Mie phase functions are compared to the standard simulations (using the HG phase function for an asymmetry parameter of 0.68) in Fig. A11 and Table A9 in Appendix A4. Again rather large deviations are found, which are larger on 18 June (up to 9 %) than on 8 July (up to 5%).

In Fig. A12 and Table A10 in Appendix A4, the effect of different surface albedos on the  $O_4$  (d)AMFs is quantified. For the considered variations (0.03 to 0.1) the changes of the  $O_4$  (d)AMFs are within 2 %.

#### 4.2.2 Uncertainties of the $O_4$ (d)AMFs caused by imperfections of the radiative transfer models

The radiative transfer models used in this study are well established and showed very good agreement in several intercomparison studies (e.g. Hendrick et al., 2006; Wagner et al., 2007; Lorente et al., 2017). Nevertheless, they are based on different methods and use different approximations (e.g. with respect to the Earth's sphericity). Thus we compared the simulated  $O_4$  (d)AMFs for both days in order to estimate the uncertainties associated to these differences. In Fig. A13 and Table A11 (appendix A4), the comparison results are shown. They agree within a few percent with slightly larger differences for 18 June (up to 6 %) than for 8 July (up to 3 %).

So far, all radiative transfer simulations were carried out without considering polarisation. Thus in Fig. A14 and Table A12 in appendix A4, the results with and without considering polarisation are compared. The corresponding differences are very small (<1%).

#### 4.2.3 Summary of uncertainties of the $O_4$ AMF from radiative transfer simulations



604

605 Table 9 presents and overview on the different sources of uncertainties of the simulated O<sub>4</sub>  
606 (d)AMFs derived from the comparison of the results from different groups and the sensitivity  
607 studies. The uncertainties are expressed as relative deviations from the results for the standard  
608 settings (see Table 6) derived by MPIC using MCARTIM.

609 In general, larger uncertainties are found for the O<sub>4</sub> dAMFs compared to the O<sub>4</sub> AMFs. This is  
610 expected because the uncertainties of the O<sub>4</sub> dAMFs contain the uncertainties of two  
611 simulations (at 90° elevation and at low elevation). Another general finding is that the  
612 uncertainties on 18 June are larger than on 8 July. This finding is mainly related to the larger  
613 uncertainties due to the aerosol phase function, which has an especially strong forward peak  
614 on 18 June. Also the error contributions from the O<sub>4</sub> profile extraction, the choice of the  
615 radiative transfer model and the extrapolation of the aerosol extinction below 180 m are larger  
616 on 18 June than on 8 July. These higher uncertainties are probably mainly related to the high  
617 aerosol extinction close to the surface on 18 June (see section 5.1, and appendices A2 and  
618 A5).

619 For the total uncertainties two values are given in Table 9: The ‘average deviation’ is the sum  
620 of all systematic deviations of the individual uncertainties (the corresponding mean of the  
621 maximum and minimum values). The second quantity (the ‘range of uncertainties’) is  
622 calculated from half the individual uncertainty ranges by assuming that they are independent.

623 Finally, it should be noted that for some error sources (e.g. the effects of the surface albedo or  
624 the single scattering albedo) the given numbers probably overestimate the true uncertainties,  
625 while for others, e.g. the uncertainties related to the aerosol extinction profiles or the phase  
626 functions they possibly underestimate the true uncertainties (although reasonable assumptions  
627 were made). The two latter error sources are especially large for 18 June. The differences  
628 between both days are discussed in more detail in section 5.

629

### 630 4.3 Uncertainties of the spectral analysis

631

632 The uncertainties of the spectral analysis are caused by different effects:

633 -the specific settings of the spectral analysis like the fit window or the degree of the  
634 polynomial. Of particular interest is the effect of choosing different O<sub>4</sub> cross sections as well  
635 as its temperature dependence.

636 -the properties (and imperfections) of the MAX-DOAS instruments

637 -the effect of different analysis software and implementations

638 -the effect of the wavelength dependence of the AMF across the fit window.

639 These error sources are discussed and quantified in the following sub sections.

640

641

#### 642 4.3.1 Comparison of O<sub>4</sub> (d)AMFs derived from the synthetic spectra with O<sub>4</sub> (d)AMFs 643 directly obtained from the radiative transfer simulations

644

645 Synthetic spectra for both selected days were simulated using the radiative transfer model  
646 SCIATRAN (for details see section 2.4 and Table A3 in appendix A1). While spectra for the  
647 whole day are simulated (for the viewing geometry see Table A2 in appendix A1) it should be  
648 noted that the aerosol properties during the middle periods are used also for the whole day (to  
649 minimise the computational efforts). The spectra are analysed using the standard settings and  
650 the derived O<sub>4</sub> (d)SCDs are converted to O<sub>4</sub> (d)AMFs using eq. 1. In addition to the spectra,  
651 also O<sub>4</sub> (d)AMFs at 360 nm are simulated directly by the RT models using exactly the same  
652 settings. These O<sub>4</sub> (d)AMFs are used to test whether the spectral retrieval results are indeed  
653 representative for the simulated O<sub>4</sub> (d)AMFs at 360 nm.





Spectra are simulated with and without considering the temperature dependence of the  $O_4$  cross section. Also one version of synthetic spectra with added random noise is processed.

First, the synthetic spectra are analysed using the standard settings (see Table 7). Examples of the  $O_4$  fits for synthetic (and measured) spectra are shown in Fig. 11.

In Fig. 12 the ratios of the  $O_4$  (d)AMFs derived from the synthetic spectra versus those directly obtained from the radiative transfer simulations at 360 nm are shown. In the upper part (a) the results for synthetic spectra considering the temperature dependence of the  $O_4$  cross section are presented (without noise). Systematically enhanced ratios are found in the morning and evening, while for most of the day the ratios are close to unity. The higher values in the morning and evening are probably partly caused by the increased light paths through higher atmospheric layers (with lower temperatures) when the solar zenith angle is high. Interestingly, if the temperature dependence of the  $O_4$  cross section is not taken into account (Fig. 12 b), still slightly enhanced ratios during the morning and evening are found, which can not be explained anymore by the temperature dependence of the  $O_4$  cross section. Thus we speculate whether part of the enhanced values at high SZA are probable caused by the wavelength dependence of the  $O_4$  AMFs. Nevertheless, for most of the day the ratio is very close to unity indicating that for  $SZA < 75^\circ$  the  $O_4$  (d)AMFs obtained from the spectral analysis are almost identical to the  $O_4$  (d)AMFs directly obtained from the radiative transfer simulations (at 360 nm).

In Fig. 12 c results for spectra with added random noise (without consideration of the temperature dependence of the  $O_4$  cross section) are shown. On average similar results as for the spectra without noise (Fig. 12 b) are found but the results now show a large scatter. From these results and also the spectral analyses (Fig. 11) we conclude that the noise added to the synthetic spectra overestimates that of the real measurements.

In Table A13 in appendix A4 the average ratios for the middle periods on both selected days are shown. They deviate from unity by up to 2% indicating that the wavelength dependence of the  $O_4$  (d)AMF is negligible for the considered cases for  $SZA < 75^\circ$ .

#### 4.3.2 Sensitivity studies for different fit parameters

In this section the effect of the choice of several fit parameters on the derived  $O_4$  (d)AMFs is investigated using both measured and synthetic spectra. Only one fit parameter is varied for each individual test, and the results are compared to those for the standard fit parameters (see Table 7).

First the fit window is varied. Besides the standard fit window (352 to 387 nm), which contains two  $O_4$  bands, also two fit windows towards shorter wavelengths are tested: 335 – 374 nm (including two  $O_4$  bands) and 345 – 374 nm (including one  $O_4$  band at 360 nm). The ratios of the derived  $O_4$  (d)AMFs versus those for the standard analysis are shown in Fig. A15 and Table A14 in appendix A2. On 18 June rather large deviations of the  $O_4$  (d)AMFs are found for both measured (-12%) and synthetic spectra (-5%) for the spectral range 335 to 374 nm. On 8 July the corresponding differences are smaller (-6% and -2% for measured and synthetic spectra, respectively). For the spectral range 345 – 374 nm, smaller differences of only up to 1% are found for both days. The reason for the larger deviations on 18 June for the spectral range 335 – 374 nm is not clear. One possible reason could be the differences of the Ångström parameters (see Fig. 1) and phase functions (see Fig 10).

In Fig. A16 and Table A15 the results for different degrees of the polynomial used in the spectral analysis are shown. For the measured spectra systematically higher  $O_4$  (d)AMFs (up to 6%) than for the standard analysis are found when using lower polynomial degrees. For the synthetic spectra the effect is smaller (<3%).

In Fig. A17 and Table A16 the results for different intensity offsets are shown. Again, for the measured spectra systematically higher  $O_4$  (d)AMFs (up to 16%) than for the standard



analysis are found when reducing the order of the intensity offset, while for the synthetic spectra the effect is smaller ( $<3\%$ ).

In Fig. A18 and Table A17 the results for spectral analyses with only one Ring spectrum are shown. In contrast to the standard analysis, which includes two Ring spectra (one for clear and one for cloudy sky, see Wagner et al., 2009), only the Ring spectrum for clear sky is used. For both selected days, only small deviations (within 2%) compared to the standard analysis are found.

#### 4.3.3 Sensitivity studies using different trace gas absorption cross sections

In this section the impact of different trace gas absorption cross sections on the derived  $O_4$  (d)AMFs is investigated.

In Fig. A19 and Table A18 the results for using two  $NO_2$  cross sections (294 and 220 K) compared to the standard analysis (using only a  $NO_2$  cross section for 294 K) are shown. The results are almost the same as for the standard analysis.

In Fig. A20 and Table A19 the results for using an additional wavelength-dependent  $NO_2$  cross section compared to the standard analysis (using only one  $NO_2$  cross section) are shown. The second  $NO_2$  cross section is calculated by multiplying the original cross section with wavelength (Pukite et al., 2010). Again, only small deviations of the results from the standard analysis (1% for the measured spectra, and 2% for the synthetic spectra) are found.

In Fig. A21 and Table A20 results for using and additional wavelength-dependent  $O_4$  cross sections compared to the standard analysis (using only one  $O_4$  cross section) are shown. The second  $O_4$  cross section is calculated like for  $NO_2$ , but also an orthogonalisation with respect to the original  $O_4$  cross section (at 360 nm) is performed. The derived  $O_4$  (d)AMFs are almost identical to those from the standard analysis (within 1%).

For the spectral retrieval of HONO in a similar spectral range, a significant impact of water vapour absorption around 363 nm was found in Wang et al. (2017c) and Lampel et al. (2017).

In Fig. A22 and Table A21 the  $O_4$  results for including a  $H_2O$  cross section (Polyansky et al., 2018) compared to the standard analysis (using no  $H_2O$  cross section) are shown. The results are almost identical to those from the standard analysis (within 1%).

In Fig. A23 and Table A22 the results for including a HCHO cross section (Polyansky et al., 2018) compared to the standard analysis (using no HCHO cross section) are shown. Especially for 18 June a large systematic effect is found: the  $O_4$  dAMFs are by 4 % or 6 % smaller than for the standard analysis for measured and synthetic spectra, respectively. On 8 July the underestimation is smaller (2% and 3% for measured and synthetic spectra, respectively).

#### 4.3.4 Effect of using different $O_4$ cross sections

In Fig. A24 and Table A23 the results for different  $O_4$  cross sections are compared to the standard analysis (using the Thalman  $O_4$  cross section). The results for both days are almost identical. For the real measurements, the derived  $O_4$  dAMFs using the Hermans and Greenblatt cross sections are by 3% smaller or 8 % larger than those for the standard analysis, respectively. However, if the Greenblatt  $O_4$  cross section is allowed to shift during the spectral analysis, the overestimation can be largely reduced to only +3 %. This confirms findings from earlier studies (e.g. Pinardi et al., 2013) that the wavelength calibration of the original data sets is not very accurate.

For the synthetic spectra slightly different results than for the real measurements are found for the Hermans  $O_4$  cross section. The reason for these differences is not clear. However, here it should be noted that the temperature dependent  $O_4$  absorption in the synthetic spectra does probably not exactly represent the true atmospheric  $O_4$  absorption.



#### 4.3.5 Effect of the temperature dependence of the O<sub>4</sub> cross section

The new set of O<sub>4</sub> cross sections provided by Thalman and Volkamer (2013) allows to investigate the temperature dependence of the atmospheric O<sub>4</sub> absorptions in detail. They provide O<sub>4</sub> cross sections measured at five temperatures (203, 233, 253, 273, 293 K) covering the range of temperatures relevant for atmospheric applications. Using these cross sections, the effect of the temperature dependence of the O<sub>4</sub> absorptions is investigated in two ways:

a) In a first test, synthetic spectra are simulated for different surface temperatures assuming a fixed lapse rate. These spectra are then analysed using the O<sub>4</sub> cross section for 293 K (which is usually used for the spectral analysis of O<sub>4</sub>). From this study the magnitude of the effect of the temperature dependence of the O<sub>4</sub> cross section on MAX-DOAS measurements can be quantified.

b) In a second test, measured and synthetic spectra for both selected days are analysed with O<sub>4</sub> cross sections for different temperatures. From this study it can be seen to which degree the temperature dependence of the O<sub>4</sub> cross section can be already corrected during the spectral analysis (if two O<sub>4</sub> cross sections are used simultaneously).

For the first study, MAX-DOAS spectra are simulated in a simplified way:

- Atmospheric temperature profiles are constructed for surface temperatures between 220 K and 310 K in steps of 10 K assuming a fixed lapse rate of  $-0.656 \text{ K} / 100 \text{ m}$ .

- For each altitude layer (vertical extension: 20 m below 500 m, 100 m between 500 m and 2 km, 200 m between 2 km and 12 km, 1 km above) the O<sub>4</sub> concentrations (calculated from the US standard atmosphere) are multiplied with the corresponding differential box-AMFs calculated for typical atmospheric conditions and viewing geometries (see Fig. A25 in appendix A4).

- High resolution absorption spectra are calculated by applying the Beer-Lambert-law for each height layer using the O<sub>4</sub> cross section of the respective temperature (interpolated between the two adjacent temperatures of the Thalman and Volkamer data set).

- The derived high resolution spectra are convolved with the instrument slit function (FWHM of 0.6 nm).

- The logarithm of the ratio of the spectra for the low elevation and zenith is calculated and analysed using the O<sub>4</sub> cross section for 293 K.

- The derived O<sub>4</sub> dAMFs are divided by the corresponding dAMFs directly obtained from the radiative transfer simulations.

These calculated ratios as function of the surface temperature are shown in Fig. 13. A strong and systematic dependence on the surface temperature is found (15 % for a change of the surface temperature between 240 and 310 K). However, except for measurements at polar regions, the deviations are usually small. Since for both selected days the temperatures were rather high (indicated by the two coloured horizontal bars in the figure), the effect of the temperature dependence of the O<sub>4</sub> absorption for the middle periods of both days is very small ( $-1$  to  $-2\%$  for 18 June, and  $0$  to  $+1\%$  on 8 July). It should be noted that the results shown in Fig. 13 are obtained for generalised settings of the radiative transfer simulations. Thus it is recommended that future studies should investigate the effect of the temperature dependence in more detail and using the exact viewing geometry for individual observations. However, since the temperatures on both selected days were rather high, for this study the simplifications of the radiative transfer simulations have no strong influence on the derived results.

In the second test the measured and synthetic spectra are analysed using O<sub>4</sub> cross sections for different temperatures. The corresponding results are shown in Fig. A26 and Table A24.

If only the O<sub>4</sub> cross section at low temperature (203 K) is used, the derived O<sub>4</sub> AMFs and dAMFs are by about 16% and 30% smaller than for the standard analysis (using the O<sub>4</sub> cross



section for 293 K). These results are consistently obtained for the measured and synthetic spectra. If, however, two  $O_4$  cross sections (for 203 and 293 K) are simultaneously included in the analysis, different results are obtained for the measured and synthetic spectra: for the measured spectra the derived  $O_4$  (d)AMFs agree within 4% with those from the standard analysis. In contrast, for the synthetic spectra, the derived  $O_4$  (d)AMFs are systematically smaller (by about 6 to 18 %). This finding was not expected, because exactly the same cross sections were used for both the simulation and the analysis of the synthetic spectra. Detailed investigations (see appendix A4) led to the conclusion that there is a slight inconsistency in the temperature dependence of the  $O_4$  cross sections from Thalman et al. (2013): The ratio of the peak values of the cross section at 360 and 380 nm changes in a non-continuous way between 253 and 223 K (see Fig. A27 in appendix A4). The reason for this inconsistency is currently not known. If these two  $O_4$  bands are included in the spectral analysis (as for the standard settings), the convergence of the spectral analysis strongly depends on the ability to fit both  $O_4$  bands well. Thus the fit results for both  $O_4$  cross sections are mainly determined by the relative strengths of both  $O_4$  bands (see Fig. A27 in appendix A4). If instead a smaller wavelength ranges is used containing only one absorption band (345 – 374 nm), the derived  $O_4$  (d)AMFs are in rather good agreement with the results of the analysis (using only the  $O_4$  cross section for 293 K), see Table A25 in appendix A4. In that case, the convergence of the fit mainly depends on the temperature dependence of the line width. It should be noted that the non-continuous temperature dependence of the  $O_4$  absorption cross section only affects the analysis of the synthetic spectra, because for the simulation of the spectra all  $O_4$  cross sections for temperatures between 223 and 293 K were used. For the measured spectra, no problems are found, because in the spectral analysis only the  $O_4$  cross sections for 223 and 293 K were used.

In Fig. A28 in appendix A4 the ratios of both fit coefficients (for 203 and 293 K) as well as the derived effective temperatures for the analyses of measured and synthetic spectra are shown. For the measured spectra the ratios are close to zero and the derived temperatures are close to 300K for most of the time (except in early morning and evening), because the effective atmospheric temperature for both days is close to the temperature of the high temperature  $O_4$  cross section (293 K) (see Fig. 13). Similar results (at least around noon) are also obtained for the synthetic spectra if the narrow spectral range (345 – 374 nm) is used. For the standard fit range (including two  $O_4$  bands), however, the ratios are much higher again indicating the effect of the inconsistency of the temperature dependence of the  $O_4$  cross sections (see Fig. A27 in appendix A4).

#### 4.3.6 Results from different instruments and analyses by different groups

In this section the effects of using measurements from different instruments and having these spectra analysed by different groups are investigated. For that purpose three different procedures are followed: First, MPIC spectra are analysed by other groups; second, the spectra from non-MPIC instruments are analysed by the respective group; third, the spectra from other instruments are analysed by MPIC.

In Fig. 14a and Table A25 (in appendix A4) the comparison results of the analysis of MPIC spectra by other groups versus the analysis of MPIC spectra by MPIC are shown. Especially for 18 June rather large differences (between –6% / +5%) to the MPIC standard analysis are found. Interestingly the largest differences are found in the morning when the aerosol extinction close to the surface was strongest. On 8 July smaller differences (between –6% and –1%) are found.

In Fig. 14b and Table A25 (in appendix A4) the comparison results of the analysis of spectra from other instruments by MPIC versus the analysis of MPIC spectra by MPIC are shown. For this comparison all analyses are performed in the spectral range 335 – 374 nm, because



the standard spectral range (352 – 387 nm) is not covered by all instruments. Again, the largest differences are found for 18 June (up to  $\pm 11\%$ ). For 8 July the differences reach up to  $\pm 6\%$ , but for this day only a few measurements in the morning are available.

In Fig. 14c and Table A25 (in appendix A4) the comparison results of the analysis of spectra from other instruments by the respective group versus the MPIC analysis by MPIC (standard analysis) is shown. From this exercise the combined effects of different instrumental properties and retrievals can be estimated. Interestingly, the observed differences are only slightly larger than those for the analysis of the spectra from the different instruments by MPIC (Fig. 14b). This indicates that the largest errors are related to the differences of the different instruments and not to the settings and implementations of the different retrievals. For the middle period of 18 June the uncertainties are within 12%. This range is also assumed for 8 July.

#### 4.3.7 Summary of uncertainties of the O<sub>4</sub> AMF from the spectral analysis

Table 10 presents an overview on the different sources of uncertainties of the measured O<sub>4</sub> (d)AMFs obtained in the previous sub-sections. The uncertainties are expressed as relative deviations from the results for the standard settings (see Table 7) derived by MPIC from spectra of the MPIC instrument

Like for the simulation results, in general, larger uncertainties are found for the O<sub>4</sub> dAMFs compared to the O<sub>4</sub> AMFs. This is expected because the uncertainties of the O<sub>4</sub> dAMFs contain the uncertainties of two analyses (at 90° elevation and at low elevation). Also, the uncertainties on 18 June are again larger than on 8 July. This finding was not expected, but is possibly related to the higher trace gas abundances (see Fig. 1 and Table A3 in appendix A1) and the higher aerosol extinction close to the surface on 18 June.

Another interesting finding is that the uncertainties of the spectral analysis of O<sub>4</sub> are dominated by the effect of instrumental properties up to  $\pm 12\%$  in the morning of 18 June. Further important uncertainties are associated with the choice of the wavelength range, the degree of the polynomial and the intensity offset. In contrast, the exact choices of the trace gas cross sections (including their wavelength- and temperature dependencies) play only a minor role (up to a few percent). Excellent agreement (within  $\pm 1\%$ ) is in particular found for the O<sub>4</sub> analysis of the synthetic spectra using the standard settings and the directly simulated O<sub>4</sub> (d)AMFs at 360 nm. This indicates that the O<sub>4</sub> (d)AMFs retrieved in the wavelength range 352 – 387 nm are indeed representative for radiative transfer simulations at 360 nm.

As for the uncertainties of the simulated O<sub>4</sub> (d)AMFs, the uncertainties of the spectral analysis are also split into a systematic and a random term: the systematic deviations of the O<sub>4</sub> dAMFs from those of the standard settings are about +1% and –1.5% for 18 June and 8 July, respectively. The range of uncertainty is calculated from the uncertainty ranges of the different error sources by assuming that they are all independent. The uncertainty ranges for 18 June and 8 July are calculated as  $\pm 12.5\%$  and  $\pm 10.8\%$ , respectively.

## 5 Discussion and conclusions

The comparison results for both days are different: On 18 June (except in the evening) measurements and simulations agree within errors (the a ratio of simulated and measured O<sub>4</sub> dAMFs is  $1.01 \pm 0.16$ ). In contrast, on 8 July measurements and simulations significantly disagree: Taking into account the errors of the VCD calculation (3%), the radiative transfer simulations ( $1 \pm 6.1\%$ ) and the spectral analysis ( $-1.5 \pm 10.8\%$ ) for the middle period of that day results in a ratio of simulated and measured O<sub>4</sub> dAMFs of  $0.71 \pm 0.12$ , which differs significantly from unity. On 18 June larger uncertainties both for the measurements and radiative transfer simulations exist, mainly related to the high aerosol concentration close to





the surface. A summary of the most important differences between both days is given in section 5.1.

A large part of this study was dedicated to the extraction of input information for the radiative transfer simulations and to the quantification of the errors of the radiative transfer simulations and spectral retrievals. In particular, the analysis of synthetic spectra indicated that the  $O_4$  results derived from the spectral analysis using the standard settings are consistent with the simulated  $O_4$  air mass factors within 1%.

Based on this study, also recommendations for similar future studies are derived (see section 5.2). In general, the largest errors sources arise from spectral analyses (partly related to imperfections of the MAX-DOAS instruments) and the uncertainties of the aerosol phase functions and extinction profiles. Even if the aerosol extinction profiles could be better constraint, e.g. using results from Raman LIDARs or high spectral-resolution LIDARs (HSRL), the uncertainties of the aerosol phase function will remain a critical error source. Future measurements should in particular try to minimize these error sources. Here it should be noted that the general larger errors obtained for 18 June are probably not representative for typical measurement conditions. For example, during the CINDI-2 campaign (<http://www.tropomi.eu/data-products/cindi-2>) the deviations of the  $O_4$  spectral analysis results were much smaller than those for 18 June.

The main conclusion from this study is that on one of the two selected days during the MADCAT campaign (08 July) a scaling factor (of about  $0.71 \pm 0.12$ ) is needed to bring measurements and forward model into agreement. As long as the reason for this deviation is not understood, it is, however, unclear, how representative these findings are for other measurements (e.g. from other platforms, at other locations/seasons, for other aerosol loads, and other wavelengths). Thus further studies spanning a large variety of measurement conditions and also including other wavelengths are recommended.

## 5.1 Important differences between both days

On both selected days similar aerosol AOD were measured. Also the diurnal variation of the SZA was similar because of the proximity to summer solstice. However, also many differences are found for the two days, which are discussed below.

### a) temperature, pressure, wind:

On 18 June surface pressure was lower by about 13 hPa and surface temperature was higher by about 7K than on 8 June, respectively. These differences were explicitly taken into account in the calculation of the  $O_4$  profiles / VCDs, the radiative transfer simulations and the interpretation of the spectral analyses. Thus they can very probably not explain the different comparison results on the two days.

On both days, wind was mainly blowing from East-North-East, but on 18 June it was blowing from West before about 08:00 and after 20:00 UTC. Wind speeds were lower on 18 June (between 1 and 2 m/s) than on 8 July (between 1 and 3 m/s).

### b) aerosol properties:

The in situ aerosol measurements show very different abundances and properties of aerosols close to the ground for the selected days. On 18 June much larger concentrations of larger aerosol particles are found, which cannot be measured by the ceilometer, because the lowest detecting altitude is 180m. Thus it can be concluded that the enhanced aerosol concentration on 18 June is confined to a shallow layer at the surface. In general the aerosol concentrations close to the surface are more variable on 18 June than on 8 July. The high aerosol concentrations close to the surface probably also affect the LIDAR ratio, which is thus more



variable on 18 June. Since a constant LIDAR ratio is used for the extraction of the aerosol extinction profiles, also the uncertainties of the aerosol profile are probably larger on 18 June. Similarly, also the phase function derived from the sun photometer (for the integrated aerosol profile) is probably less representative for the low elevation angles on 18 June because different aerosol size distributions probably existed at different altitudes. Finally, the Ångström parameter derived from AERONET observations is different for both days, especially for large wavelengths, which is in qualitative agreement with the higher in situ aerosol concentrations of large particles on 18 June. Also a larger forward peak of the derived aerosol phase function is found for 18 June. Both effects probably cause larger uncertainties on 18 June.

#### c) spectral analysis

Larger uncertainties of the spectral analysis are found for 18 June compared to 8 July. This finding was surprising, but was also partly reproduced by the analysis of the synthetic spectra. One possible explanation is the smaller wavelength dependence of aerosol scattering at low altitudes on 18 June, which mainly affects measurements at low elevation angles. When analysed versus a zenith reference, for which the broad band wavelength dependency is much stronger (because of the larger contribution from Rayleigh scattering), larger deviations can be expected (e.g. because of differences of instrumental straylight, or the different detector saturation levels). On 18 June also higher (about doubled) NO<sub>2</sub> and HCHO concentrations are present compared to 8 July possibly leading to increased spectral interferences with the O<sub>4</sub> absorption, but this effect is expected to be small.

## 5.2 Recommendations

Based on the findings of this comparison study, recommendations for similar future studies are derived. Part of them are also of interest for the interpretation of O<sub>4</sub> measurements in general.

#### a) VCD calculation

Temperature and pressure profiles representative for individual days should be used. If such profiles are not available, also profiles extrapolated from surface measurements can be used. They are not ‘perfect’ but usually the associated errors are at the percent level. The vertical grid for the integration of the O<sub>4</sub> profile should not be coarser than 100m. The integration should be carried out up to an altitude of at least 30 km. The exact height of the instrument position needs to be taken into account.

#### b) Radiative transfer simulations

If available appropriate phase functions (e.g. from Mie calculations) should be used. Here it is important to note that even if appropriate asymmetry parameters are available, the often used HG parameterisation becomes very imprecise for forward scattering geometries.

#### c) Spectral analysis

The spectral range should cover the two O<sub>4</sub> bands at 360 and 380 nm. An intensity offset should be included in the analysis. If the surface temperature differs strongly (more than 25K) from 300K the effect of the temperature dependence of the O<sub>4</sub> absorption should be considered.



1009 d) Preferred scenarios for future studies  
 1010 In particular the uncertainties related to aerosols should be minimised. For example,  
 1011 measurements at rather low AOD ( $\leq 0.1$ ) and with low temporal variability should be selected.  
 1012 Aerosol profiles should be derived from LIDARs/ceilometers which are sensitive down to very  
 1013 shallow altitudes (low overlap ranges). If possible, Raman LIDARs or high spectral-  
 1014 resolution LIDARs (HSRL) should be used, because from such observations the aerosol  
 1015 extinction profile can be derived without the assumption of a LIDAR ratio. Also sun  
 1016 photometer measurements should be available. Besides AOD and the Ångström parameter  
 1017 also information on the phase function and single scattering albedo from these measurements  
 1018 should be used.  
 1019 It would be interesting to cover other meteorological conditions (e.g. low temperatures),  
 1020 viewing geometries (e.g. low SZA), surface albedos (e.g. snow and ice) and wavelengths (e.g.  
 1021 477, 577, and 630 nm).  
 1022 In order to minimise the effects of instrumental properties, the instruments should be well  
 1023 calibrated and should have low straylight levels. At least two instruments should be operated  
 1024 at the same site. Based on the above criteria, measurements during the CINDI-2 campaign are  
 1025 probably well suited for a similar study.

## 1026 1027 1028 **Acknowledgments** 1029

1030 We are thankful for several external data sets which were used in this study: Temperature and  
 1031 pressure profiles from the ERAInterim reanalysis data set were provided by the European  
 1032 Centre for Medium-Range Weather Forecasts. In situ measurements of trace gas and aerosol  
 1033 concentrations as well as meteorological data were performed by the environmental  
 1034 monitoring services of the States of Rhineland-Palatinate and Hesse (<http://www.luft-rlp.de>  
 1035 and <https://www.hlnug.de/themen/luft/luftmessnetz.html>). We thank M. O. Andreae and  
 1036 Günther Schebeske for operating the Ceilometer and the AERONET instrument at the Max  
 1037 Planck Institute for Chemistry.

1038  
1039  
1040  
1041  
1042  
1043  
1044  
1045  
1046  
1047  
1048  
1049  
1050  
1051  
1052  
1053  
1054  
1055  
1056  
1057  
1058  
1059

**Tables**

Table 1 Overview on studies which did not apply a scaling factor (upper part) or did apply a scaling factor (lower part) to the measured O<sub>4</sub> dSCDs. Besides the initial studies proposing a scaling factor (Wagner et al., 2009; Clémer et al., 2010) only studies after 2010 are listed.

Reference	Measurement type	Location and period	O <sub>4</sub> band (nm)	Scaling factor
<b>Studies which did not apply a scaling factor*</b>				
Peters et al., 2012a	MAX-DOAS	Western Pacific Ocean (Oct 2009)	360, 477	1
Spinei et al. 2015	Direct sun DOAS	JPL, USA (Jul 2007) Pullman, USA (Sep – Nov 2007, Jul – Nov 2011) Fairbanks, USA (Mar-Apr 2011) Huntsville, USA (Aug 2008) Richland, USA (Apr-Jun 2008) Greenbelt, USA (May 2007, 2012-2014) Cabauw, The Netherlands (Jun-Jul 2009)	360, 477	1
Spinei et al., 2015	Airborne DOAS	Subtropical Pacific Ocean (Jan 2012)	360, 477	1
Ortega et al., 2016	MAX-DOAS	Cape Cod, USA (Jul 2012)	360, 477	1
Schreier et al., 2016	MAX-DOAS	Zugspitze, Germany (Apr-Jul 2003) Pico Espeio, Venezuela (2004 - 2009)	360	1
Seyler et al., 2017	MAX-DOAS	German Bight (2013-2016)	360, 477	1
Wang et al., 2017a,b	MAX-DOAS	Wuxi, China (2011 - 2014)	360	1
Gielen et al., 2017	MAX-DOAS	Bujumbura, Burundi (2013-2015)	360, 477	1
Franco et al., 2015	MAX-DOAS	Jungfraujoch (2010 –2012)	360	1
<b>Studies which did apply a scaling factor</b>				
Wagner et al., 2009	MAX-DOAS	Milano, Italy Sep 2013 (FORMAT II)	360	0.81
Clémer et al., 2010	MAX-DOAS	Beijing, China Jul 2008 – Apr 2009	360, 477, 577, 630	0.80
Irie et al., 2011	MAX-DOAS	Cabauw, The Netherlands Jul-Jun 2009 (CINDI-I)	360, 477	0.75±0.1
Merlaud et al., 2011	Airborne DOAS	Arctic Apr 2008 POLARCAT)	360	0.89
Vlemmix et al., 2011	MAX-DOAS	Cabauw, The Netherlands Jul-Oct 2009 (CINDI-I)	477	0.8
Zieger et al., 2011	Overview on MAX-DOAS	Cabauw, The Netherlands Jul-Oct 2009 (CINDI-I)	360 (MPIC) 477 (BIRA) 477 (IUPHD) 477 (JAMSTEC)	0.83 0.75 0.8 0.8*
Wang et al., 2014	MAX-DOAS	Xianghe, China (2010 - 2013)	360	0.8
Kanaya et al., 2014	MAX-DOAS	Cape Hedo, Japan (2007 – 2012) Fukue, Japan (2008 – 2012) Yokosuda, Japan (2007 – 2012) Gwangju, Korea (2008 – 2012) Hefei, China (2008 – 2012) Zvenigorod, Russia (2009 – 2012)	477 477 477 477 477 477	0.8 0.8 0.8 0.8 0.8 0.8



Hendrick et al., 2014	MAX-DOAS	Beijing, China (2008 - 2009) Xianghe, China (2010 - 2012)	360	0.8
Vlemmix et al., 2015	MAX-DOAS	Beijing, China (2008 - 2009) Xianghe, China (2010 - 2012)	360, 477	0.8
Irie et al., 2015	MAX-DOAS	Tsukuba, Japan (Oct 2010)	477	elevation dependent scaling factor**
Wang et al., 2016	MAX-DOAS	Madrid, Spain (Mar – Sep 2015)	360	0.83
Friess et al., 2016	MAX-DOAS	Cabauw, The Netherlands Jul-Jul 2009 (CINDI-I)	477 (AOIFM) 477 (BIRA) 477 (IUPHD) 477 (JAMSTEC) 360 (MPIC)	0.8 0.8 1 0.8*** 0.77

\*The authors of part of these studies were probably not aware that a scaling factor was applied by other groups.

\*\*SF =  $1 / (1 + EA/60)$

\*\*\*SF is varied during profile inversion

Table 2 Periods on both selected days, which are used for the comparisons.

day	1 <sup>st</sup> period	2 <sup>nd</sup> period	3 <sup>rd</sup> period
18 June 2013	8:00 – 11:00 UTC	11:00 – 14:00 UTC	14:00 – 19:00 UTC
8 July 2013	4:00 – 7:00 UTC	7:00 – 11:00 UTC	11:00 – 19:00 UTC

Table 3 Participation of the different groups in the different analysis steps

Abreviation	Institution	Determination of the O <sub>4</sub> profile and VCD	Extraction of aerosol profiles	Radiative transfer simulations	Spectral analysis
BIRA	BIRA/IASB, Brussels, Belgium				•
CMA	Meteorological Observation Center, Beijing, China			•	•
CSIC	Department of Atmospheric Chemistry and Climate, Institute of Physical Chemistry Rocasolano (CSIC), Spain.	•			•
INTA	Instituto Nacional de Tecnica Aeroespacial, Spain	•	•	•	•
IUP-B	University of Bremen, Germany		•	•	•
IUP-HD	University of Heidelberg, Germany				•
LMU	Ludwig-Maximilians-Universität München, Germany	•	•		
MPIC	MPI for chemistry, Mainz, Germany	•	•	•	•





Table 4 Overview on properties of MAX-DOAS instruments participating in this study

Institute / Instrument type	Spectral range (nm)	Spectral resolution (FWHM, nm)	Spectral range per detector pixel (nm)	Detector type / temperature	Integration time of individual spectra (s)	Reference
BIRA / 2-D scanning MAX-DOAS	300 - 386	0.49	0.04	2-D back-illuminated CCD, 2048 x 512 pixels / -40 °C	60	Clémer et al., 2010
IUP-Bremen / 2-D scanning MAX-DOAS	308 - 376	0.43	0.05	2-D back-illuminated CCD, 1340 x 400 pixels / -35 °C	20	Peters et al., 2012b
IUP-Heidelberg / 1-D scanning MAX-DOAS	294 - 459	0.59	0.09	AvaSpec-ULS 2048 pixels back-thinned Hamamatsu CCD S11071-1106 / 20°C	60	Lampel et al., 2015
MPIC / 4-azimuth MAX-DOAS	320 – 457	0.67	0.14	2-D back-illuminated CCD, 1024 x 255 Pixels / -30°C	10 s	Krautwurst, 2010



1105 Table 5 Independent data sets used to constrain the atmospheric properties during both  
1106 selected days.

Measurement / data set	Measured quantities	Derived quantities	Temporal / spatial resolution	Source / reference
Ceilometer	Attenuated backscatter profiles* at 1064 nm	Aerosol extinction profiles at 360 nm	30s** / 15 m	Wiegner and Geiß, 2012
AERONET sun photometer	Solar irradiances, Sky radiances	Aerosol optical depth, single scattering albedo, phase function	Typical integration time: 2 to 15 min	Holben et al., 2001, <a href="https://aeronet.gsfc.nasa.gov/">https://aeronet.gsfc.nasa.gov/</a>
Surface measurements air quality stations in Mainz Mombach	temperature, pressure, rel. humidity		1h	<a href="http://www.luft-rlp.de">http://www.luft-rlp.de</a>
Surface measurements air quality stations in Mainz and Wiesbaden	pm <sub>2.5</sub> pm <sub>10</sub>		1h (Mainz stations)  30 min (Wiesbaden stations)***	<a href="http://www.luft-rlp.de">http://www.luft-rlp.de</a>  <a href="https://www.hlnug.de/themen/luft/luftmessnetz.html">https://www.hlnug.de/themen/luft/luftmessnetz.html</a>
ECMWF ERA-Interim reanalysis	temperature, Pressure, rel. humidity		Average over the area 49.41°-50.53° N, 7.88°-9.00° E, every 6 h	(Dee et al., 2011)

1107 \*no useful signal below 180m due to limited overlap

1108 \*\*Here 15 min averages are used.

1109 \*\*\*Stations in Mainz: Parcusstrasse, Zitadelle, Mombach; Stations in Wiesbaden: Schierstein,  
1110 Ringkirche, Süd

1111

1112

1113

1114

1115 Table 6 Standard settings for the radiative transfer simulations

Parameter	Standard setting
Temperature and pressure profile	MPIC extraction
O <sub>4</sub> profile	MPIC extraction
Surface albedo	5 %
Aerosol single scattering albedo	0.95
Aerosol phase function	HG model with asymmetry parameter of 0.68
Aerosol extinction profile	MPIC extraction with linear interpolation < 180 m
Polarisation	Not considered
Raman scattering	Partly considered for synthetic spectra

1116

1117

1118

1119 Table 7 Standard settings for the DOAS analysis of O<sub>4</sub>.

Parameter	Value, Remark / Reference
Spectral range	352 – 387 nm
Degree of DOAS polynomial	5
Degree of intensity offset polynomial	2
Fraunhofer reference spectrum	08 July, 10:05:35, SZA: 32.37°, elevation angle: 90° (this spectrum is used for both days)
Wavelength calibration	Fit to high resolution solar spectrum using Gaussian slit function
Shift / squeeze	The measured spectrum is shifted and squeezed against all other spectra
Ring spectrum 1	Normal Ring spectrum calculated from DOASIS
Ring spectrum 2	Ring spectrum 1 multiplied by $\lambda^{-4}$
O <sub>3</sub> cross section	223 K, Bogumil et al. (2003)
NO <sub>2</sub> cross section	294 K, Vandaele et al. (1997)
BrO cross section	223 K, Fleischmann et al. (2004)
O <sub>4</sub> cross section	293 K, Thalman and Volkamer (2013)

1120

1121

1122 Table 8 Average ratios (simulation results divided by measurements) of the O<sub>4</sub> (d)AMFs for  
1123 both middle periods of the selected days.

Period	18.06.2013, 11:00 – 14:00	08.07.2013, 7:00 – 11:00
AMF ratio	0.97	0.83
DAMF ratio	0.94	0.69

1124

1125

1126 Table 9 Summary of uncertainties of the simulated O<sub>4</sub> (d)AMFs for the middle periods of  
1127 both selected days. The two numbers left and right of the ‘/’ indicate the minimum and  
1128 maximum deviations.

	O <sub>4</sub> AMF		O <sub>4</sub> dAMF	
	18 June	8 July	18 June	8 July
<b>Effects of RTM</b>				
Radiative transfer model	-1% / +2%	0% / +1%	-1% / +5%	0% / +3%
Polarisation	0% / 0%	0% / 0%	0% / 0%	0% / +1%
<b>Effects of input parameters</b>				
O <sub>4</sub> profile extraction	0% / + 2%	0% / + 1%	0% / + 4%	0% / + 2%
Single scattering albedo	-1% / + 3%	-1% / + 1%	-1% / + 3%	-1% / + 1%
Phase function	-3% / +3%	-2% / 0%	-5% / + 9%	-5% / +2%
Aerosol profile extraction	-1% / + 1%	-2% / + 2%	-2% / + 1%	-4% / + 4%
Extrapolation below 180 m	0% / + 2%	-1% / + 1%	-1% / + 4%	-2% / + 2%
Surface albedo	0% / + 2%	0% / + 1%	0% / + 2%	-1% / + 0%
<b>Total uncertainty</b>				
Average deviation (from results for standard settings)	+4.5%	+0.5%	+8.5%	1%
Range of uncertainty	±4.4%	±2.8%	±8.7%	±6.1%

1129



1130 Table 10 Summary of uncertainties of the measured O<sub>4</sub> (d)AMFs for the middle periods of  
 1131 both selected days. The two numbers left and right of the ‘/’ indicate the minimum and  
 1132 maximum deviations.

	O <sub>4</sub> AMF		O <sub>4</sub> dAMF	
	18 June	8 July	18 June	8 July
<b>Consistency spectral analysis versus RTM</b>				
Analysis of synthetic spectra	-1% / +1%	-1% / 0%	0% / 0%	0% / +1%
<b>Fit settings</b>				
Spectral range	-7% / -3%	-3% / 0%	-12% / -1%	-6% / -1%
Degree of polynomial	+0% / +4%	0% / +3%	0% / +6%	0% / +6%
Intensity offset*	+1% / +5%	+1% / +3%	+3% / +11%	+2% / +4%
Ring	+1% / +2%	-1% / +1%	+1% / +1%	-1% / +1%
Temperature dependence of NO <sub>2</sub> absorption	0% / 0%	0% / 0%	0% / 0%	0% / 0%
Wavelength dependence of NO <sub>2</sub> absorption	-1% / 0%	0% / 0%	-2% / -1%	-1% / 0%
Wavelength dependence of O <sub>4</sub> absorption	-1% / 0%	-1% / -1%	0% / +1%	-1% / -1%
Including H <sub>2</sub> O cross section	0% / 0%	0% / 0%	+1% / +1%	+1% / +1%
Including HCHO cross section	-3% / 0%	-1% / 0%	-6% / -4%	-3% / -2%
Different O <sub>4</sub> cross sections*	-2% / +1%	-2% / +1%	-3% / +3%	-3% / +3%
<b>Temperature dependence of the O<sub>4</sub> absorption</b>				
Analysis using two O <sub>4</sub> cross sections for different temperatures <sup>†</sup>	0% / 0%	+2% / +2%	+4% / +4%	+1% / +1%
Analysis of synthetic spectra for different surface temperatures	-1% / 0%	-1% / +2%	+4% / +4%	+1% / +1%
<b>Analysis from different instruments and groups</b>				
Different groups and analyses <sup>‡</sup>	-6% / +5%	-6% / +5%	-12% / +7%	-12% / +7%
<b>Total uncertainty</b>				
Average deviation (from results for standard settings)	-4.5%	-0.5%	+1%	-1.5%
Range of uncertainty	±7.0%	±6.5%	±12.5%	±10.8%

1133 \*here the case ‘no offset’ is not considered

1134 †here the case of the non-shifted Greenblatt O<sub>4</sub> cross section is not considered

1135 ‡here only the results for the measured spectra in the spectral range 352 – 387 nm are  
 1136 considered. (temperatures on 18 June: 27–31 °C; 8 July: 20–30 °C)

1137 \*The results for 18 June are also taken for 8 July due to the lack of measurements on 8 July

1138



## References

- Acarreta, J. R., De Haan, J. F., and Stammes, P.: Cloud pressure retrieval using the O<sub>2</sub>-O<sub>2</sub> absorption band at 477 nm, *J. Geophys. Res.*, 109, D05204, doi:10.1029/2003JD003915, 2004.
- Bogumil, K., J. Orphal, T. Homann, S. Voigt, P. Spietz, O. C. Fleischmann, A. Vogel, M. Hartmann, H. Bovensmann, J. Frerik and J. P. Burrows, Measurements of Molecular Absorption Spectra with the SCIAMACHY Pre-Flight Model: Instrument Characterization and Reference Data for Atmospheric Remote-Sensing in the 230-2380 nm Region, *J. Photochem. Photobiol. A.*, 157, 167-184, 2003.
- Chandrasekhar S. Radiative Transfer. New York: Dover Publications Inc.; 1960.
- Chandrasekhar S. Selected papers, vol. 2. New York: University of Chicago Press, 1989.
- Clémer, K., Van Roozendaal, M., Fayt, C., Hendrick, F., Hermans, C., Pinardi, G., Spurr, R., Wang, P., and De Mazière, M.: Multiple wavelength retrieval of tropospheric aerosol optical properties from MAXDOAS measurements in Beijing, *Atmos. Meas. Tech.*, 3, 863-878, doi:10.5194/amt-3-863-2010, 2010.
- Dee, D. P., Uppala, S. M., Simmons, A. J., Berrisford, P., Poli, P., Kobayashi, S., Andrae, U., Balmaseda, M. A., Balsamo, G., Bauer, P., Bechtold, P., Beljaars, A. C. M., van de Berg, L., Bidlot, J., Bormann, N., Delsol, C., Dragani, R., Fuentes, M., Geer, A. J., Haimberger, L., Healy, S. B., Hersbach, H., Hólm, E. V., Isaksen, I., Kållberg, P., Köhler, M., Matricardi, M., McNally, A. P., Monge-Sanz, B. M., Morcrette, J.-J., Park, B.-K., Peubey, C., de Rosnay, P., Tavolato, C., Thépaut, J.-N., and Vitart, F.: The ERA-Interim reanalysis: configuration and performance of the data assimilation system, *Q. J. Roy. Meteorol. Soc.*, 137, 553-597, doi:10.1002/qj.828, 2011.
- Deutschmann, T., Beirle, S., Frieß, U., Grzegorski, M., Kern, C., Kritten, L., Platt, U., Pukite, J., Wagner, T., Werner, B., and Pfeilsticker, K.: The Monte Carlo Atmospheric Radiative Transfer Model McArtim: Introduction and Validation of Jacobians and 3D Features, *J. Quant. Spectrosc. Ra.*, 112, 1119-1137, doi:10.1016/j.jqsrt.2010.12.009, 2011.
- Dubovik, O., Holben, B. N., Eck, T. F., Smirnov, A., Kaufman, Y. J., King, M. D., Tanré, D., and Slutsker, I.: Variability of absorption and optical properties of key aerosol types observed in worldwide locations, *J. Atmos. Sci.*, 59, 590-608, 2002.
- Erle F., K. Pfeilsticker, and U. Platt, On the influence of tropospheric clouds on zenith-scattered-light measurements of stratospheric species, *Geophys. Res. Lett.*, 22, 2725- 2728, 1995.
- Fleischmann, O. C., Hartmann, M., Burrows, J. P., and Orphal, J.: New ultraviolet absorption cross-sections of BrO at atmospheric temperatures measured by time-windowing Fourier transform spectroscopy, *J. Photoch. Photobio. A*, 168, 117-132, 2004.
- Franco, B., Hendrick, F., Van Roozendaal, M., Müller, J.-F., Stavrakou, T., Marais, E. A., Bovy, B., Bader, W., Fayt, C., Hermans, C., Lejeune, B., Pinardi, G., Servais, C., and Mahieu, E.: Retrievals of formaldehyde from ground-based FTIR and MAX-DOAS observations at the





- 1189 Jungfraujoch station and comparisons with GEOS Chem and IMAGES model simulations,  
1190 Atmos. Meas. Tech., 8, 1733-1756, <https://doi.org/10.5194/amt-8-1733-2015>, 2015.
- 1191
- 1192 Frieß, F., P. S. Monks, J. J. Remedios, A. Rozanov, R. Sinreich, T. Wagner, and U. Platt,  
1193 MAX-DOAS O4 measurements: A new technique to derive information on atmospheric  
1194 aerosols. (II) Modelling studies, J. Geophys. Res., 111, D14203,  
1195 doi:10.1029/2005JD006618, 2006.
- 1196
- 1197 Frieß, U., Klein Baltink, H., Beirle, S., Clémer, K., Hendrick, F., Henzing, B., Irie, H., de  
1198 Leeuw, G., Li, A., Moerman, M. M., van Roozendaal, M., Shaiganfar, R., Wagner, T., Wang,  
1199 Y., Xie, P., Yilmaz, S., and Zieger, P.: Intercomparison of aerosol extinction profiles retrieved  
1200 from MAX-DOAS measurements, Atmos. Meas. Tech., 9, 3205-3222,  
1201 <https://doi.org/10.5194/amt-9-3205-2016>, 2016.
- 1202
- 1203 Gielen, C., Hendrick, F., Pinardi, G., De Smedt, I., Fayt, C., Hermans, C., Stavrakou, T.,  
1204 Bauwens, M., Müller, J.-F., Ndenzako, E., Nzohabonayo, P., Akimana, R., Niyonzima, S.,  
1205 Van Roozendaal, M., and De Mazière, M.: Characterisation of Central-African aerosol and  
1206 trace-gas emissions based on MAX-DOAS measurements and model simulations over  
1207 Bujumbura, Burundi, Atmos. Chem. Phys. Discuss., <https://doi.org/10.5194/acp-2016-1104>,  
1208 in review, 2017.
- 1209
- 1210 Greenblatt G.D., Orlando, J.J., Burkholder, J.B., and Ravishankara, A.R.: Absorption  
1211 measurements of oxygen between 330 and 1140 nm, J. Geophys. Res., 95, 18577-18582,  
1212 1990.
- 1213
- 1214 Hendrick, F., Van Roozendaal, M., Kylling, A., Petritoli, A., Rozanov, A., Sanghavi, S.,  
1215 Schofield, R., von Friedeburg, C., Wagner, T., Wittrock, F., Fonteyn, D., and De Mazière, M.:  
1216 Intercomparison exercise between different radiative transfer models used for the  
1217 interpretation of ground-based zenith-sky and multi-axis DOAS observations, Atmos. Chem.  
1218 Phys., 6, 93-108, doi:10.5194/acp-6-93-2006, 2006.
- 1219
- 1220 Hendrick, F., Müller, J.-F., Clémer, K., Wang, P., De Mazière, M., Fayt, C., Gielen, C.,  
1221 Hermans, C., Ma, J. Z., Pinardi, G., Stavrakou, T., Vlemmix, T., and Van Roozendaal, M.:  
1222 Four years of ground-based MAX-DOAS observations of HONO and NO<sub>2</sub> in the Beijing area,  
1223 Atmos. Chem. Phys., 14, 765-781, <https://doi.org/10.5194/acp-14-765-2014>, 2014.
- 1224
- 1225 Heue, K.-P., Riede, H., Walter, D., Brenninkmeijer, C. A. M., Wagner, T., Frieß, U., Platt, U.,  
1226 Zahn, A., Stratmann, G., and Ziereis, H.: CARIBIC DOAS observations of nitrous acid and  
1227 formaldehyde in a large convective cloud, Atmos. Chem. Phys., 14, 6621-6642,  
1228 <https://doi.org/10.5194/acp-14-6621-2014>, 2014.
- 1229
- 1230 Hönninger, G., von Friedeburg, C., and Platt, U.: Multi Axis Differential Optical Absorption  
1231 Spectroscopy (MAX-DOAS), Atmos. Chem. Phys., 4, 231-254, 2004.
- 1232
- 1233 Holben, B. N., Tanre, D., Smirnov, A., Eck, T. F., Slutsker, I., Abuhassan, N., Newcomb, W.  
1234 W., Schafer, J., Chatenet, B., Lavenue, F., Kaufman, Y. J., Vande Castle, J., Setzer, A.,  
1235 Markham, B., Clark, D., Frouin, R., Halthore, R., Karnieli, A., O'Neill, N. T., Pietras, C.,  
1236 Pinker, R. T., Voss, K., and Zibordi, G.: An emerging ground-based aerosol climatology:  
1237 Aerosol Optical Depth from AERONET, J. Geophys. Res., 106, 12067-12097, 2001.
- 1238



- 1239 Irie, H., Kanaya, Y., Akimoto, H., Iwabuchi, H., Shimizu, A., and Aoki, K.: First retrieval of  
1240 tropospheric aerosol profiles using MAX-DOAS and comparison with lidar and sky  
1241 radiometer measurements, *Atmos. Chem. Phys.*, 8, 341–350, doi:10.5194/acp-8-341-2008,  
1242 2008.
- 1243
- 1244 Irie, H., Takashima, H., Kanaya, Y., Boersma, K. F., Gast, L., Wittrock, F., Brunner, D.,  
1245 Zhou, Y., and Van Roozendaal, M.: Eight-component retrievals from ground-based MAX-  
1246 DOAS observations, *Atmos. Meas. Tech.*, 4, 1027–1044, [https://doi.org/10.5194/amt-4-1027-](https://doi.org/10.5194/amt-4-1027-2011)  
1247 2011, 2011.
- 1248
- 1249 Irie, H., Nakayama, T., Shimizu, A., Yamazaki, A., Nagai, T., Uchiyama, A., Zaizen, Y.,  
1250 Kagamitani, S., and Matsumi, Y.: Evaluation of MAX-DOAS aerosol retrievals by coincident  
1251 observations using CRDS, lidar, and sky radiometer in Tsukuba, Japan, *Atmos. Meas. Tech.*,  
1252 8, 2775–2788, <https://doi.org/10.5194/amt-8-2775-2015>, 2015.
- 1253
- 1254 Kanaya, Y., Irie, H., Takashima, H., Iwabuchi, H., Akimoto, H., Sudo, K., Gu, M., Chong, J.,  
1255 Kim, Y. J., Lee, H., Li, A., Si, F., Xu, J., Xie, P.-H., Liu, W.-Q., Dzhola, A., Postlyakov, O.,  
1256 Ivanov, V., Grechko, E., Terpuogova, S., and Panchenko, M.: Long-term MAX-DOAS  
1257 network observations of NO<sub>2</sub> in Russia and Asia (MADRAS) during the period 2007–2012:  
1258 instrumentation, elucidation of climatology, and comparisons with OMI satellite observations  
1259 and global model simulations, *Atmos. Chem. Phys.*, 14, 7909–7927,  
1260 <https://doi.org/10.5194/acp-14-7909-2014>, 2014.
- 1261
- 1262 Krautwurst, S.: Charakterisierung eines neu aufgebauten MAXDOAS-Systems und  
1263 Interpretation von ersten Messergebnissen zu dem Spurenstoff NO<sub>2</sub>, Diplomarbeit,  
1264 Fachhochschule Coburg, Coburg, Germany, 2010.
- 1265
- 1266 Lampel, J., Frieß, U., and Platt, U.: The impact of vibrational Raman scattering of air on  
1267 DOAS measurements of atmospheric trace gases, *Atmos. Meas. Tech.*, 8, 3767–3787,  
1268 <https://doi.org/10.5194/amt-8-3767-2015>, 2015.
- 1269
- 1270 Lampel, J., Pöhler, D., Polyansky, O. L., Kyuberis, A. A., Zobov, N. F., Tennyson, J., Lodi,  
1271 L., Frieß, U., Wang, Y., Beirle, S., Platt, U., and Wagner, T.: Detection of water vapour  
1272 absorption around 363 nm in measured atmospheric absorption spectra and its effect on  
1273 DOAS evaluations, *Atmos. Chem. Phys.*, 17, 1271–1295, [https://doi.org/10.5194/acp-17-](https://doi.org/10.5194/acp-17-1271-2017)  
1274 1271-2017, 2017.
- 1275
- 1276 Lorente, A., Folkert Boersma, K., Yu, H., Dörner, S., Hilboll, A., Richter, A., Liu, M.,  
1277 Lamsal, L. N., Barkley, M., De Smedt, I., Van Roozendaal, M., Wang, Y., Wagner, T., Beirle,  
1278 S., Lin, J.-T., Krotkov, N., Stammes, P., Wang, P., Eskes, H. J., and Krol, M.: Structural  
1279 uncertainty in air mass factor calculation for NO<sub>2</sub> and HCHO satellite retrievals, *Atmos.*  
1280 *Meas. Tech.*, 10, 759–782, <https://doi.org/10.5194/amt-10-759-2017>, 2017.
- 1281
- 1282 Meller, R. and G. K. Moortgat, Temperature dependence of the absorption cross sections of  
1283 formaldehyde between 223 and 323 K in the wavelength range 225–375 nm, *J. Geophys. Res.*,  
1284 105, 7089–7101, 2000.
- 1285
- 1286 Merlaud, A., Van Roozendaal, M., Theys, N., Fayt, C., Hermans, C., Quennehen, B.,  
1287 Schwarzenboeck, A., Ancellet, G., Pommier, M., Pelon, J., Burkhardt, J., Stohl, A., and De  
1288 Mazière, M.: Airborne DOAS measurements in Arctic: vertical distributions of aerosol



- 1289 extinction coefficient and NO<sub>2</sub> concentration, *Atmos. Chem. Phys.*, 11, 9219–9236,  
1290 doi:10.5194/acp-11-9219-2011, 2011.  
1291  
1292 Ortega, I., Berg, L. K., Ferrare, R. A., Hair, J. W., Hostetler, C. A., and Volkamer, R.:  
1293 Elevated aerosol layers modify the O<sub>2</sub>-O<sub>2</sub> absorption measured by ground-based MAX-  
1294 DOAS, *J. Quant. Spectrosc. Ra.*, 176, 34–49, doi:10.1016/j.jqsrt.2016.02.021, 2016.  
1295  
1296 Paur, R. J. and Bass, A. M.: The Ultraviolet Cross-Sections of Ozone: II. Results and  
1297 temperature dependence, in: *Atmospheric ozone; Proc. Quadrennial Ozone Symposium*,  
1298 edited by: Zeferos, C. S. and Ghazi, A., Halkidiki Greece, 1984, Dordrecht: Reidel, D., 611–  
1299 615, 1984.  
1300  
1301 Peters, E., Wittrock, F., Großmann, K., Frieß, U., Richter, A., and Burrows, J. P.:  
1302 Formaldehyde and nitrogen dioxide over the remote western Pacific Ocean: SCIAMACHY  
1303 and GOME-2 validation using ship-based MAX-DOAS observations, *Atmos. Chem. Phys.*,  
1304 12, 11179–11197, <https://doi.org/10.5194/acp-12-11179-2012>, 2012a.  
1305  
1306 Peters, E., Wittrock, F., Großmann, K., Frieß, U., Richter, A., and Burrows, J. P.:  
1307 Formaldehyde and nitrogen dioxide over the remote western Pacific Ocean: SCIAMACHY  
1308 and GOME-2 validation using ship-based MAX-DOAS observations, *Atmos.*  
1309 *Chem. Phys.*, 12, 11179–11197, <https://doi.org/10.5194/acp-12-11179-2012>, 2012b.  
1310  
1311 Pinardi, G., Van Roozendaal, M., Abuhassan, N., Adams, C., Cede, A., Clémer, K., Fayt, C.,  
1312 Frieß, U., Gil, M., Herman, J., Hermans, C., Hendrick, F., Irie, H., Merlaud, A., Navarro  
1313 Comas, M., Peters, E., Piders, A. J. M., Puertedura, O., Richter, A., Schönhardt, A.,  
1314 Shaiganfar, R., Spinei, E., Strong, K., Takashima, H., Vrekoussis, M., Wagner, T., Wittrock,  
1315 F., and Yilmaz, S.: MAX-DOAS formaldehyde slant column measurements during CINDI:  
1316 intercomparison and analysis improvement, *Atmos. Meas. Tech.*, 6, 167–185,  
1317 <https://doi.org/10.5194/amt-6-167-2013>, 2013.  
1318  
1319 Polyansky, O.L., A.A. Kyuberis, N.F. Zobov, J. Tennyson, S.N. Yurchenko and L. Lodi  
1320 ExoMol molecular line lists XXX: a complete high-accuracy line list for water, *Mon. Not. R.*  
1321 *astr. Soc.*, submitted, 2018.  
1322  
1323 Prados-Roman, C., Butz, A., Deutschmann, T., Dorf, M., Kritten, L., Minikin, A., Platt, U.,  
1324 Schlager, H., Sihler, H., Theys, N., Van Roozendaal, M., Wagner, T., and Pfeilsticker, K.:  
1325 Airborne DOAS limb measurements of tropospheric trace gas profiles: case studies on the  
1326 profile retrieval of O<sub>4</sub> and BrO, *Atmos. Meas. Tech.*, 4, 1241–1260, doi:10.5194/amt-4-1241-  
1327 2011, 2011.  
1328  
1329 Puķīte, J., Kühl, S., Deutschmann, T., Platt, U., and Wagner, T.: Extending differential optical  
1330 absorption spectroscopy for limb measurements in the UV, *Atmos. Meas. Tech.*, 3, 631–653,  
1331 doi:10.5194/amt-3-631-2010, 2010.  
1332  
1333 Schreier, S. F., Richter, A., Wittrock, F., and Burrows, J. P.: Estimates of free-tropospheric  
1334 NO<sub>2</sub> and HCHO mixing ratios derived from high-altitude mountain MAX-DOAS  
1335 observations at midlatitudes and in the tropics, *Atmos. Chem. Phys.*, 16, 2803–2817,  
1336 <https://doi.org/10.5194/acp-16-2803-2016>, 2016.  
1337



- 1338 Serdyuchenko, A., Gorshelev, V., Weber, M., Chehade, W., and Burrows, J. P.: High spectral  
1339 resolution ozone absorption cross-sections – Part 2: Temperature dependence, Atmos. Meas.  
1340 Tech., 7, 625-636, <https://doi.org/10.5194/amt-7-625-2014>, 2014.
- 1341
- 1342 Seyler, A., Wittrock, F., Kattner, L., Mathieu-Üffing, B., Peters, E., Richter, A., Schmolke, S.,  
1343 and Burrows, J. P.: Monitoring shipping emissions in the German Bight using MAX-DOAS  
1344 measurements, Atmos. Chem. Phys., 17, 10997-11023, [https://doi.org/10.5194/acp-17-10997-](https://doi.org/10.5194/acp-17-10997-2017)  
1345 2017, 2017.
- 1346
- 1347 Sneep, M., de Haan, J. F., Stammes, P., Wang, P., Vanbauce, C., Joiner, J., Vasilkov, A. P.,  
1348 and Levelt, P. F.: Three-way comparison between OMI and PARASOL cloud pressure  
1349 products, J. Geophys. Res., 113, D15S23, doi:10.1029/2007JD008694, 2008.
- 1350
- 1351 Solomon, S., A. L. Schmeltekopf, and R. W. Sanders, On the interpretation of zenith sky  
1352 absorption measurements, *J. Geophys. Res.*, 92, 8311-8319, 1987.
- 1353
- 1354 Spinei, E., Cede, A., Herman, J., Mount, G. H., Eloranta, E., Morley, B., Baidar, S., Dix, B.,  
1355 Ortega, I., Koenig, T., and Volkamer, R.: Ground-based direct-sun DOAS and airborne  
1356 MAX-DOAS measurements of the collision-induced oxygen complex, O<sub>2</sub>O<sub>2</sub>, absorption with  
1357 significant pressure and temperature differences, Atmos. Meas. Tech., 8, 793-809,  
1358 <https://doi.org/10.5194/amt-8-793-2015>, 2015.
- 1359
- 1360 Spurr RJD, Kurosu TP, Chance KV. A linearized discrete ordinate radiative transfer model  
1361 for atmospheric remote sensing retrieval. *JQSRT* 2001;68:689–735.
- 1362
- 1363 Spurr, R., LIDORT and VLIDORT: Linearized Pseudo-Spherical Scalar and Vector Discrete  
1364 Ordinate Radiative Transfer Models for Use in Remote Sensing Retrieval Problems, *Light*  
1365 *Scattering Reviews*, Vol. 3, edited by: Kokhanovsky, A., Springer, Berlin Heidelberg,  
1366 Germany, 2008.
- 1367
- 1368 Stamnes K, Tsay S-C, Wiscombe W, Jayaweera K. Numerically stable algorithm for discrete  
1369 ordinate method radiative transfer in multiple scattering and emitting layered media. *Appl Opt*  
1370 1988; 27:2502-9.
- 1371
- 1372 Thalman, R. and Volkamer, R.: Temperature dependent absorption cross-sections of O<sub>2</sub>–O<sub>2</sub>  
1373 collision pairs between 340 and 630 nm and at atmospherically relevant pressure, *Phys.*  
1374 *Chem. Chem. Phys.*, 15, 15371, doi:10.1039/c3cp50968k, 2013.
- 1375
- 1376 United States Committee on Extension to the Standard Atmosphere: U.S. Standard  
1377 Atmosphere, 1976, National Oceanic and Atmospheric Administration, National Aeronautics  
1378 and Space Administration, United States Air Force, Washington D.C., 1976.
- 1379
- 1380 Vandaele, A. C., C. Hermans, P. C. Simon, M. Carleer, R. Colin, S. Fally, M.-F. Mérienne, A.  
1381 Jenouvrier, and B. Coquart, Measurements of the NO<sub>2</sub> Absorption Cross-section from 42000  
1382 cm<sup>-1</sup> to 10000 cm<sup>-1</sup> (238-1000 nm) at 220 K and 294 K, *J. Quant. Spectrosc. Radiat.*  
1383 *Transfer*, 59, 171-184, 1997.
- 1384
- 1385 Vlemmix, T., Piters, A. J. M., Berkhout, A. J. C., Gast, L. F. L., Wang, P., and Levelt, P. F.:  
1386 Ability of the MAX-DOAS method to derive profile information for NO<sub>2</sub>: can the boundary  
1387 layer and free troposphere be separated?, Atmos. Meas. Tech., 4, 2659-2684,  
1388 <https://doi.org/10.5194/amt-4-2659-2011>, 2011.



- 1389  
1390 Vlemmix, T., Hendrick, F., Pinardi, G., De Smedt, I., Fayt, C., Hermans, C., Pitters, A., Wang,  
1391 P., Levelt, P., and Van Roozendaal, M.: MAX-DOAS observations of aerosols, formaldehyde  
1392 and nitrogen dioxide in the Beijing area: comparison of two profile retrieval approaches,  
1393 Atmos. Meas. Tech., 8, 941-963, <https://doi.org/10.5194/amt-8-941-2015>, 2015.  
1394  
1395 Wagner, T., F. Erle, L. Marquard, C. Otten, K. Pfeilsticker, T. Senne, J. Stutz, and U. Platt,  
1396 Cloudy sky optical paths as derived from differential optical absorption spectroscopy  
1397 observations, *J. Geophys. Res.*, 103, 25307-25321, 1998.  
1398  
1399 Wagner, T., B. Dix, C.v. Friedeburg, U. Frieß, S. Sanghavi, R. Sinreich, and U. Platt MAX-  
1400 DOAS O4 measurements – a new technique to derive information on atmospheric aerosols.  
1401 (I) Principles and information content, *J. Geophys. Res.*, 109, doi: 10.1029/2004JD004904,  
1402 2004.  
1403  
1404 Wagner, T., J. P. Burrows, T. Deutschmann, B. Dix, C. von Friedeburg, U. Frieß, F.  
1405 Hendrick, K.-P. Heue, H. Irie, H. Iwabuchi, Y. Kanaya, J. Keller, C. A. McLinden, H. Oetjen,  
1406 E. Palazzi, A. Petritoli, U. Platt, O. Postylakov, J. Pukite, A. Richter, M. van Roozendaal, A.  
1407 Rozanov, V. Rozanov, R. Sinreich, S. Sanghavi, F. Wittrock, Comparison of Box-Air-Mass-  
1408 Factors and Radiances for Multiple-Axis Differential Optical Absorption Spectroscopy  
1409 (MAX-DOAS) Geometries calculated from different UV/visible Radiative Transfer Models,  
1410 Atmos. Chem. Phys., 7, 1809-1833, 2007.  
1411  
1412 Wagner, T., Deutschmann, T., and Platt, U.: Determination of aerosol properties from MAX-  
1413 DOAS observations of the Ring effect, Atmos. Meas. Tech., 2, 495-512, 2009.  
1414  
1415 Wagner, T., Beirle, S., Deutschmann, T., and Penning de Vries, M.: A sensitivity analysis of  
1416 Ring effect to aerosol properties and comparison to satellite observations, Atmos. Meas.  
1417 Tech., 3, 1723-1751, doi:10.5194/amt-3-1723-2010, 2010.  
1418  
1419 Wang, T., Hendrick, F., Wang, P., Tang, G., Clémer, K., Yu, H., Fayt, C., Hermans, C.,  
1420 Gielen, C., Müller, J.-F., Pinardi, G., Theys, N., Brenot, H., and Van Roozendaal, M.:  
1421 Evaluation of tropospheric SO<sub>2</sub> retrieved from MAX-DOAS measurements in Xianghe,  
1422 China, Atmos. Chem. Phys., 14, 11149-11164, <https://doi.org/10.5194/acp-14-11149-2014>,  
1423 2014.  
1424  
1425 Wang, S., Cuevas, C. A., Frieß, U., and Saiz-Lopez, A.: MAX-DOAS retrieval of aerosol  
1426 extinction properties in Madrid, Spain, Atmos. Meas. Tech., 9, 5089-5101,  
1427 <https://doi.org/10.5194/amt-9-5089-2016>, 2016.  
1428  
1429 Wang, Y., Beirle, S., Lampel, J., Koukouli, M., De Smedt, I., Theys, N., Li, A., Wu, D., Xie,  
1430 P., Liu, C., Van Roozendaal, M., Stavrakou, T., Müller, J.-F., and Wagner, T.: Validation of  
1431 OMI, GOME-2A and GOME-2B tropospheric NO<sub>2</sub>, SO<sub>2</sub> and HCHO products using MAX-  
1432 DOAS observations from 2011 to 2014 in Wuxi, China: investigation of the effects of priori  
1433 profiles and aerosols on the satellite products, Atmos. Chem. Phys., 17, 5007-5033,  
1434 <https://doi.org/10.5194/acp-17-5007-2017>, 2017a.  
1435  
1436 Wang, Y., Lampel, J., Xie, P., Beirle, S., Li, A., Wu, D., and Wagner, T.: Ground-based  
1437 MAX-DOAS observations of tropospheric aerosols, NO<sub>2</sub>, SO<sub>2</sub> and HCHO in Wuxi, China,  
1438 from 2011 to 2014, Atmos. Chem. Phys., 17, 2189-2215, doi:10.5194/acp-17-2189-2017,  
1439 2017b.

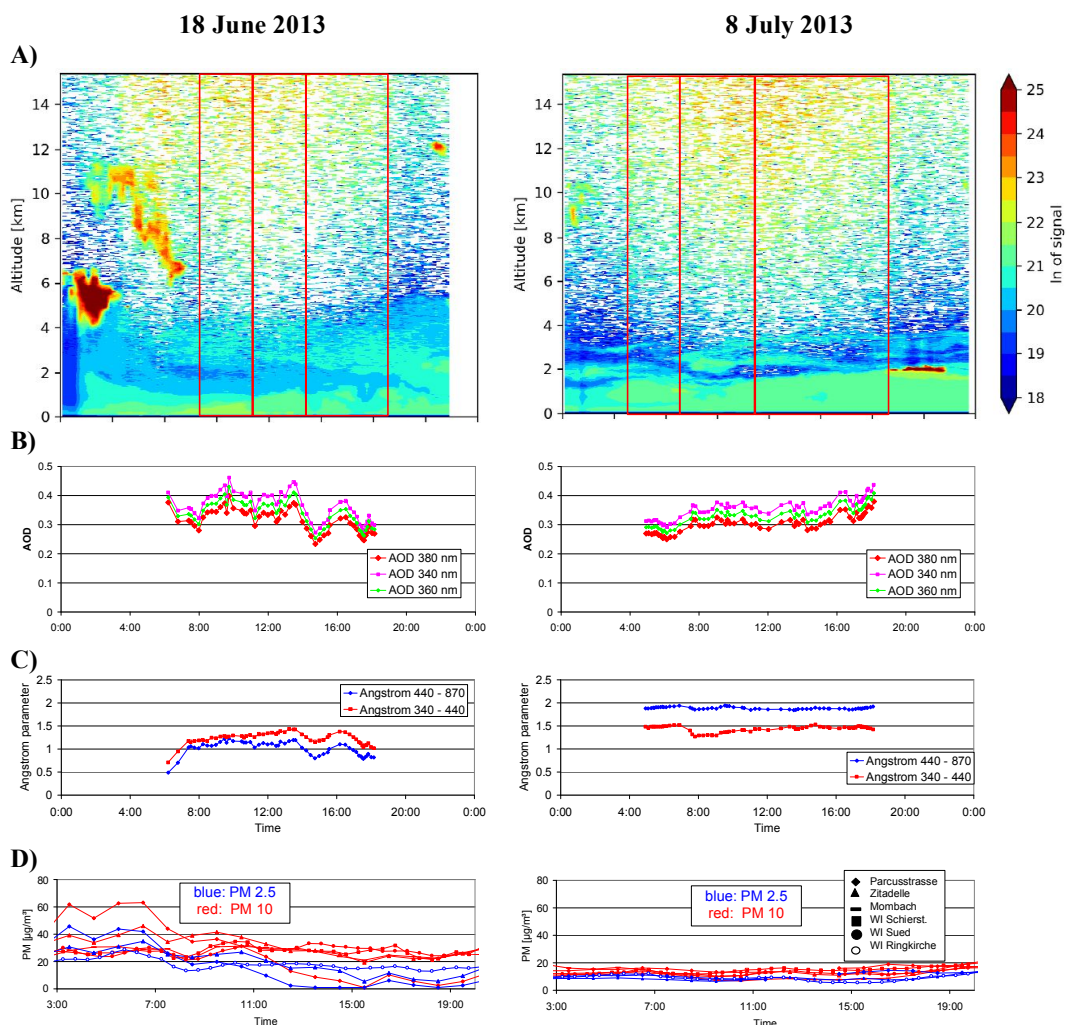


- 1440  
1441 Wang, Y., Beirle, S., Hendrick, F., Hilboll, A., Jin, J., Kyuberis, A. A., Lampel, J., Li, A.,  
1442 Luo, Y., Lodi, L., Ma, J., Navarro, M., Ortega, I., Peters, E., Polyansky, O. L., Remmers, J.,  
1443 Richter, A., Puentedura, O., Van Roozendaal, M., Seyler, A., Tennyson, J., Volkamer, R.,  
1444 Xie, P., Zobov, N. F., and Wagner, T.: MAX-DOAS measurements of HONO slant column  
1445 densities during the MAD-CAT campaign: inter-comparison, sensitivity studies on spectral  
1446 analysis settings, and error budget, Atmos. Meas. Tech., 10, 3719-3742,  
1447 <https://doi.org/10.5194/amt-10-3719-2017>, 2017c.  
1448  
1449 Wiegner, M. and Geiß, A.: Aerosol profiling with the Jenoptik ceilometer CHM15kx, Atmos.  
1450 Meas. Tech., 5, 1953-1964, <https://doi.org/10.5194/amt-5-1953-2012>, 2012.  
1451  
1452 Winterrath, T., T. P. Kurosu, A. Richter and J. P. Burrows, Enhanced O<sub>3</sub> and NO<sub>2</sub> in  
1453 thunderstorm clouds: convection or production?, Geophys. Res. Lett., No. 26, pp. 1291-1294,  
1454 1999.  
1455  
1456 Wittrock, F., H. Oetjen, A. Richter, S. Fietkau, T. Medeke, A. Rozanov, J. P. Burrows  
1457 MAX-DOAS measurements of atmospheric trace gases in Ny-Ålesund - Radiative transfer  
1458 studies and their application, Atmos. Chem. Phys., 4, 955-966, 2004  
1459  
1460 Zieger, P., Weingartner, E., Henzing, J., Moerman, M., de Leeuw, G., Mikkilä, J., Ehn, M.,  
1461 Petäjä, T., Clémer, K., van Roozendaal, M., Yilmaz, S., Frieß, U., Irie, H., Wagner, T.,  
1462 Shaiganfar, R., Beirle, S., Apituley, A., Wilson, K., and Baltensperger, U.: Comparison of  
1463 ambient aerosol extinction coefficients obtained from in-situ, MAX-DOAS and LIDAR  
1464 measurements at Cabauw, Atmos. Chem. Phys., 11, 2603-2624, [https://doi.org/10.5194/acp-](https://doi.org/10.5194/acp-11-2603-2011)  
1465 [11-2603-2011](https://doi.org/10.5194/acp-11-2603-2011), 2011.  
1466  
1467  
1468  
1469  
1470  
1471  
1472  
1473  
1474  
1475  
1476  
1477  
1478  
1479  
1480  
1481  
1482  
1483  
1484  
1485  
1486  
1487  
1488  
1489  
1490





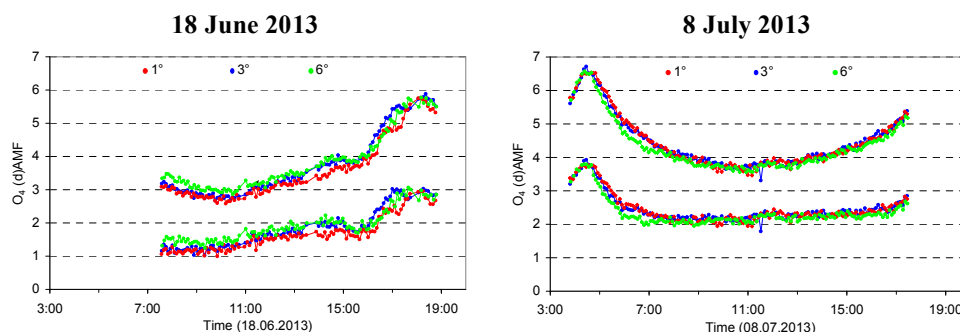
1491 **Figures**  
 1492



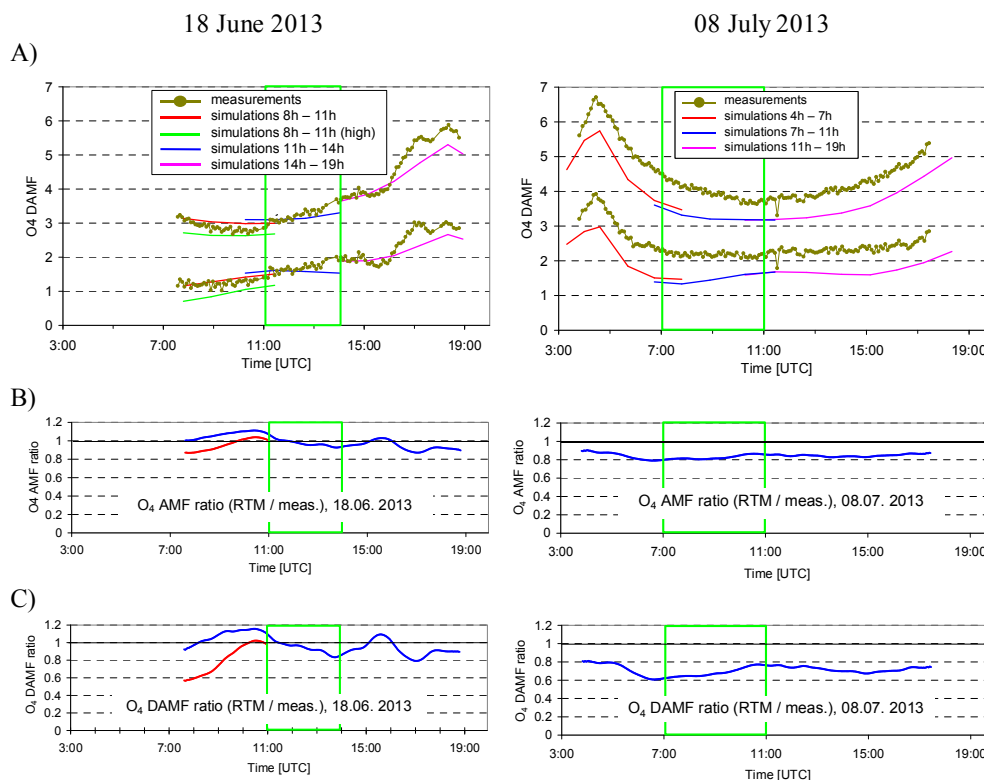
1493 Fig. 1 Various aerosol properties on the two selected days (left: 18 June 2013; right: 8 July  
 1494 2013). A) Aerosol backscatter profiles from ceilometer measurements; B) AOD at 340, 360,  
 1495 and 380 nm (360 values are interpolated from 340 and 380 nm) from AERONET sun  
 1496 photometer measurements; C) Ångström parameters for two wavelength pairs (340 – 440 nm  
 1497 and 440 – 870 nm) from AERONET sun photometer measurements; D) Surface in situ  
 1498 measurements of PM<sub>2.5</sub> and PM<sub>10</sub> measured at different air quality monitoring stations in  
 1499 Mainz and the nearby city of Wiesbaden .



1507



1508 Fig. 2 O<sub>4</sub> AMFs (upper lines) and dAMFs (lower lines) for 1°, 3°, and 6° elevation angles  
 1509 derived from the MPIC MAX-DOAS measurements on the two selected days. Interestingly,  
 1510 on 18 June the lowest values are in general found for the lowest elevation angles, which is an  
 1511 indication for the high aerosol load close to the surface.  
 1512  
 1513



1514 Fig. 3 A) Comparison of O<sub>4</sub> (d)AMFs from MAX-DOAS measurements and forward model  
 1515 simulations for the two selected days. The green rectangle indicates the middle periods on  
 1516 both days, which are the focus of the quantitative comparison. The green line on 18 June  
 1517 represents forward model results for a modified aerosol profile (see text). In B) and C) the  
 1518 ratios of the simulated and measured AMFs and dAMFs are shown, respectively. The red line  
 1519 on 18 June represents the ratios for the modified aerosol scenario.

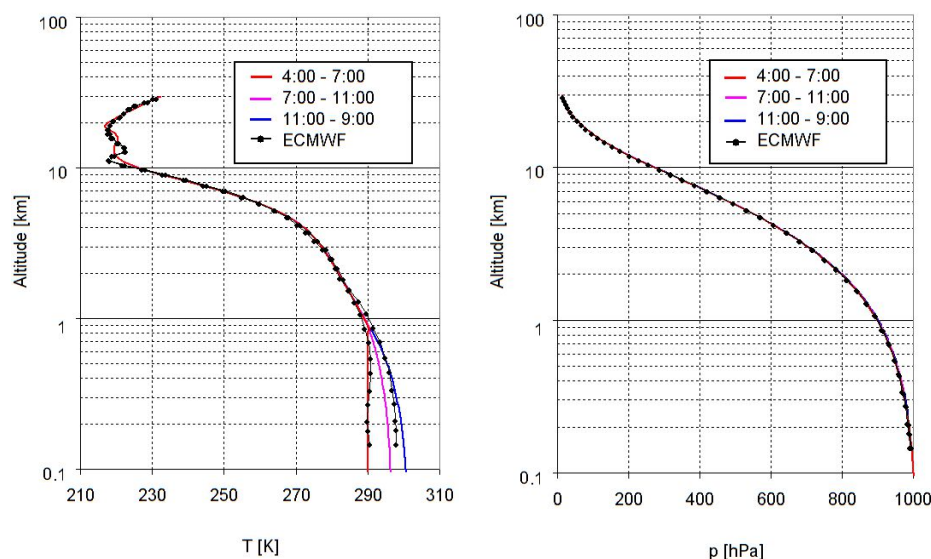


Fig. 4 Extracted temperature (left) and pressure (right) profiles for the three periods on 8 July 2013. Also shown are ECMWF profiles above Mainz for 6:00 and 18:00. To better account for the diurnal variation of the temperatures near the surface, below 1 km the temperature is linearly interpolated between the surface measurements and the ECMWF temperatures at 1 km (for details see text). Note that the altitude is given relative to the height of the measurement site (150 m).

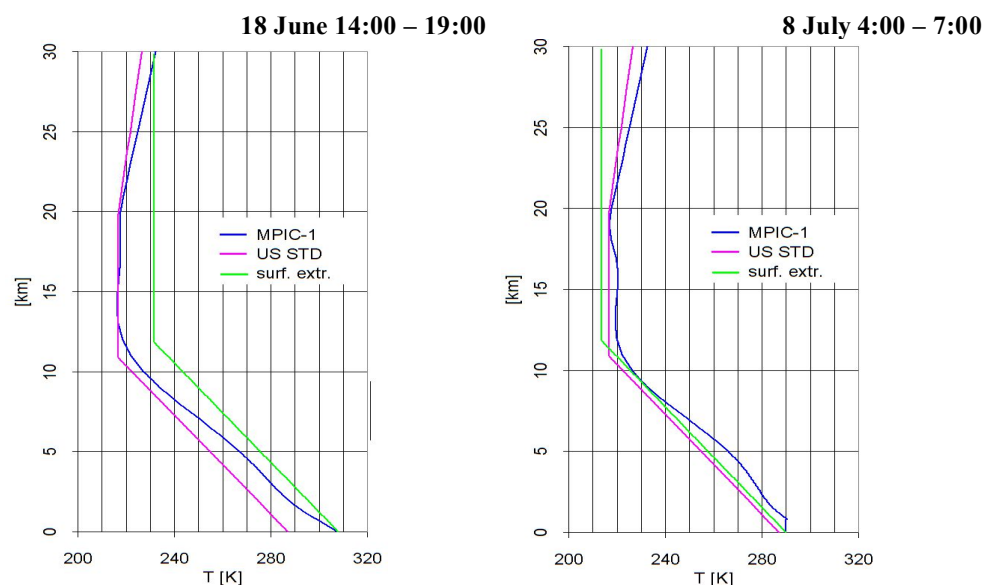
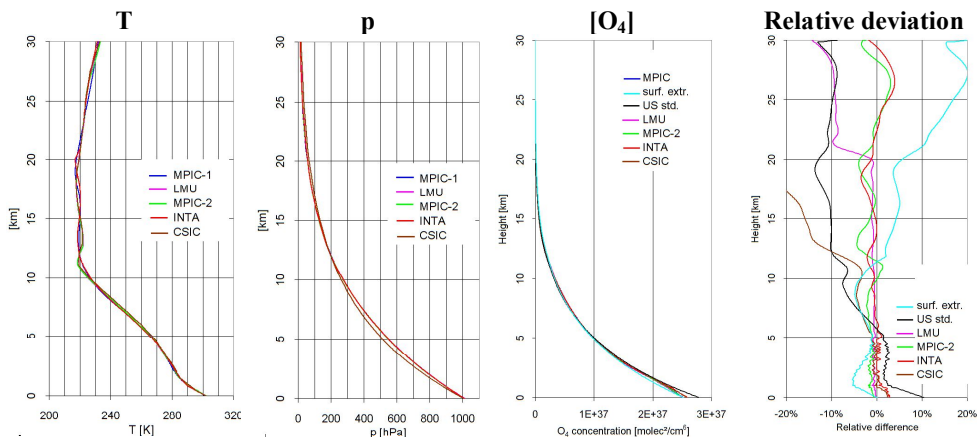


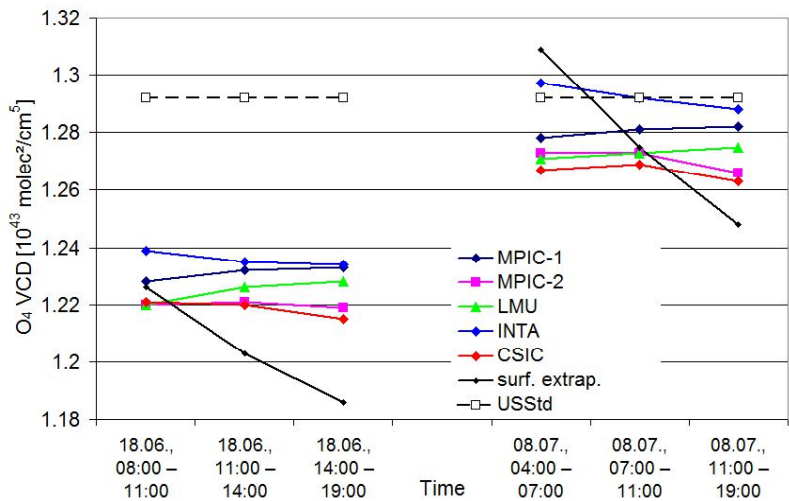
Fig. 5 Temperature profiles extracted in different ways for two periods (Left: 18 June 14:00 – 19:00; right: 8 July 4:00 – 7:00). The blue profiles are extracted from in situ measurements and ECMWF profiles as described in the text. The green profiles are extracted from the surface temperatures and assuming a constant lapse rate of  $-6.5\text{ K / km}$  up to 12 km and a constant temperature above. The pink curves represent the temperature profile from the US standard atmosphere.



1533



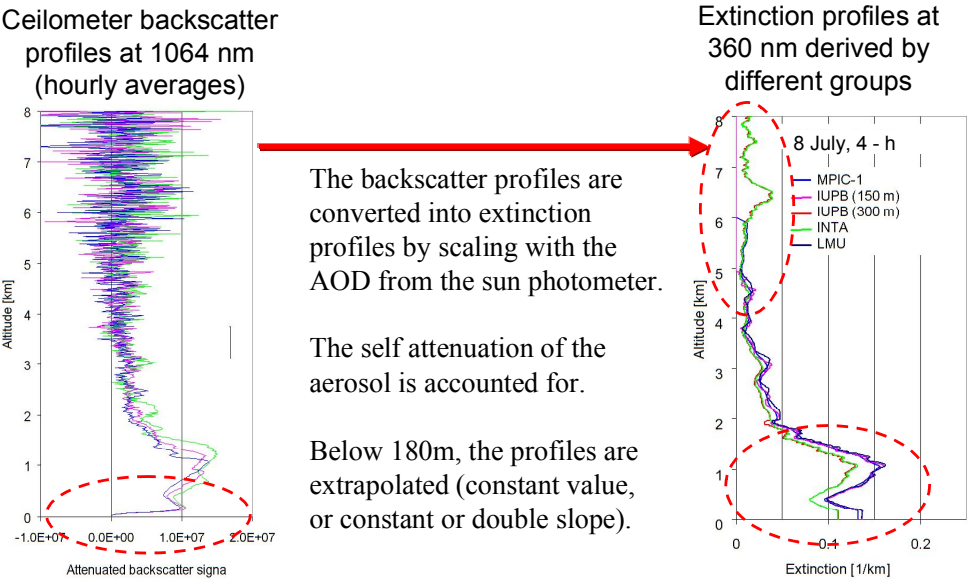
1534 Fig. 6 Comparison of the vertical profiles of temperature, pressure and O<sub>4</sub> concentration  
1535 (expressed as the square of the O<sub>2</sub> concentration) for 8 July, 11:00 – 19:00, extracted by the  
1536 different groups. In the right figure the relative deviations of the O<sub>4</sub> concentration compared to the MPIC  
1537 standard extraction are shown. There, also the profiles derived from the extrapolation from the surface values and the US  
1538 standard atmosphere are included.  
1539  
1540



1541  
1542  
1543 Fig. 7 Comparison of the O<sub>4</sub> VCDs for the selected periods on both days calculated from the  
1544 profiles extracted by the different groups. Also the results for the profiles extrapolated from  
1545 the surface values and the US standard atmosphere are shown.  
1546  
1547  
1548  
1549  
1550  
1551  
1552



1553



1554

1555

1556

1557

1558

1559

1560

1561

1562

1563

1564

1565

1566

1567

1568

1569

1570

1571

1572

1573

1574

1575

1576

1577

1578

1579

1580

1581

1582

1583

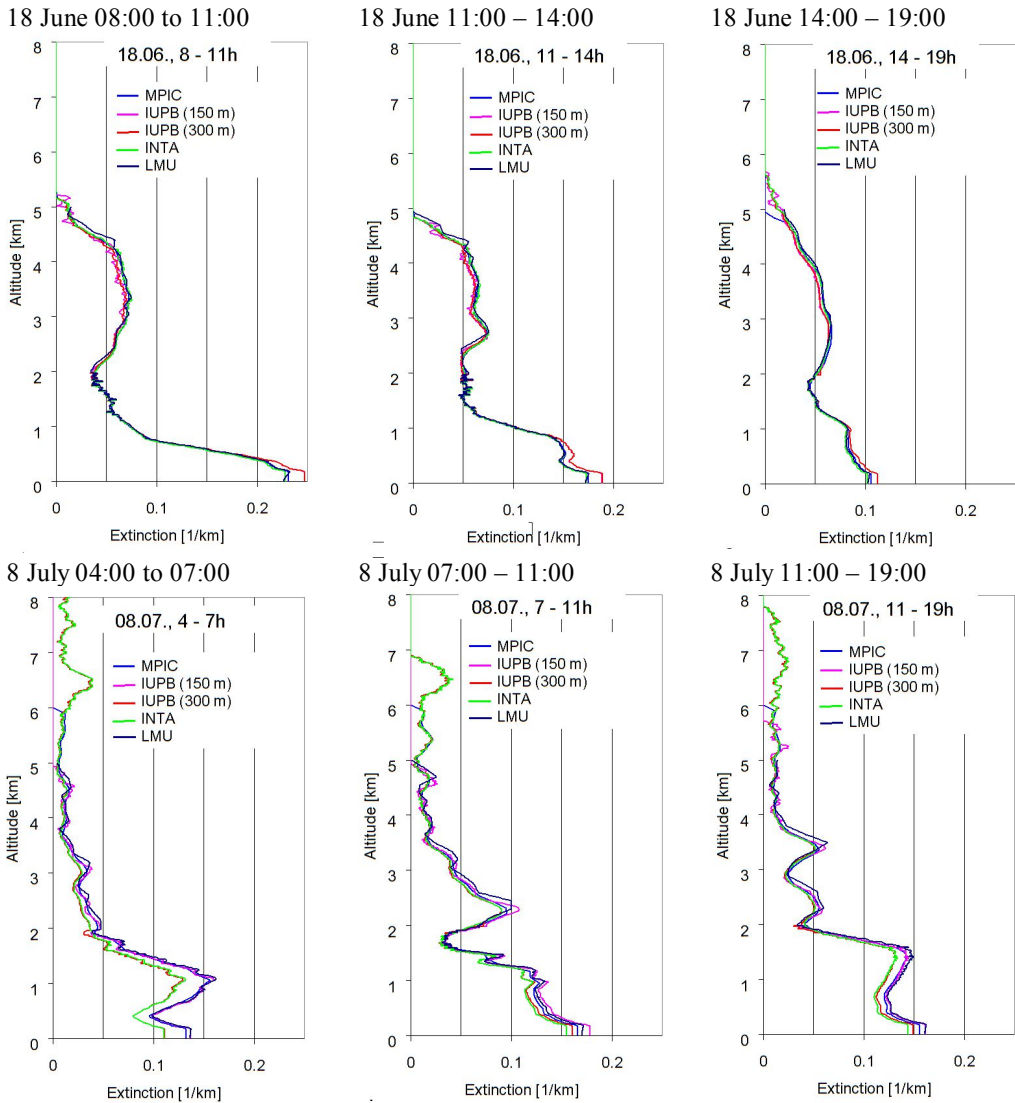
1584

Fig. 8 Left: Hourly averaged backscatter profiles from the ceilometer measurements for the period 4:00 – 7:00 on 8 July 2013. Below 180 m the values rapidly decrease to zero due to the missing overlap between the outgoing beam and the field of view of the telescope. Right: Aerosol extinction profiles extracted by the different groups from the ceilometer profiles (assuming a constant extinction below 180 m). The red circles indicate the height intervals with the largest deviations (IUPB 150 m and IUPB 300 m indicate profile extractions with different widths of the smoothing kernels: Hanning windows of 150 and 300 m, respectively).





1585  
1586

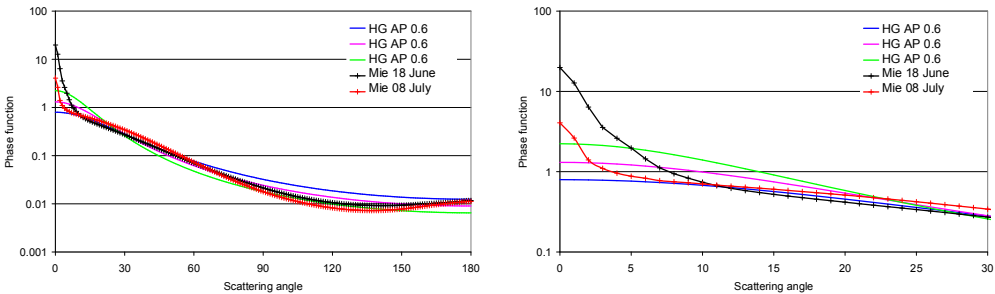


1587 Fig. 9 Comparison of the aerosol extinction profiles extracted by the different groups for all  
1588 three periods on both days.  
1589

1590  
1591  
1592  
1593  
1594  
1595  
1596  
1597  
1598

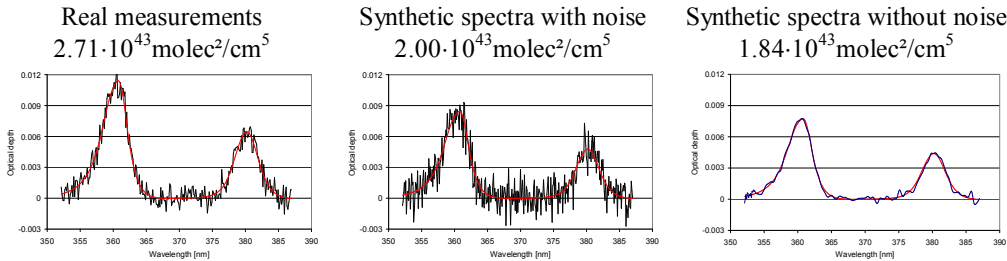


1599  
1600



1601 Fig. 10 Comparison of different aerosol phase functions used in the radiative transfer  
1602 simulations. The right figure is a zoom of the left figure.

1603  
1604  
1605  
1606



1607 Fig. 11 Spectral analysis results for a real measurement from the MPIC instrument (left) and a  
1608 synthetic spectrum with and without noise. Spectra are taken from 8 July 2013 at 11:26  
1609 (elevation angle = 1°). The derived O<sub>4</sub> dSCD is shown above the individual plots.

1610  
1611  
1612  
1613  
1614  
1615  
1616  
1617  
1618  
1619  
1620  
1621  
1622  
1623  
1624  
1625  
1626  
1627  
1628  
1629  
1630

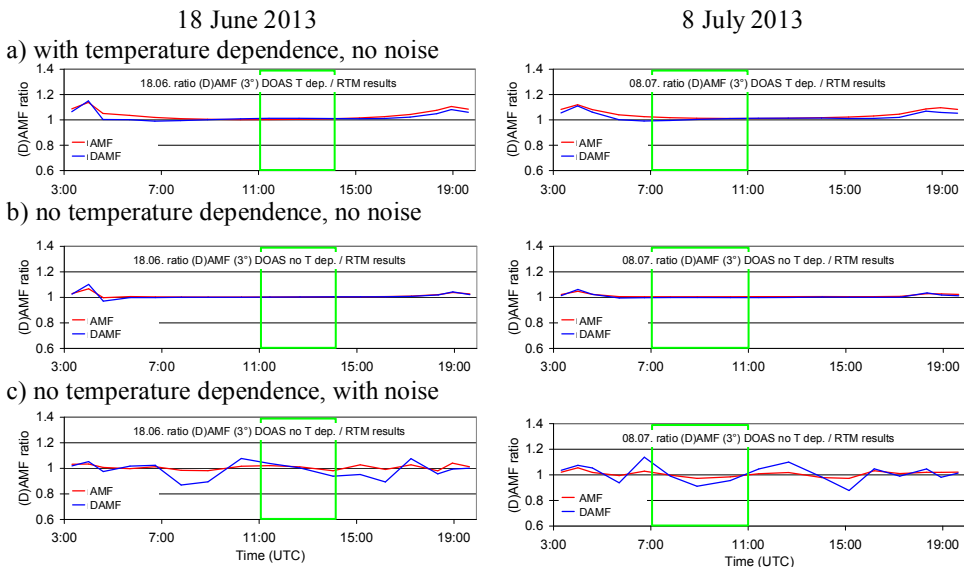


Fig. 12 Ratio of the O<sub>4</sub> (d)AMFs derived from synthetic spectra versus those obtained from radiative transfer simulations at 360 nm for both selected days.

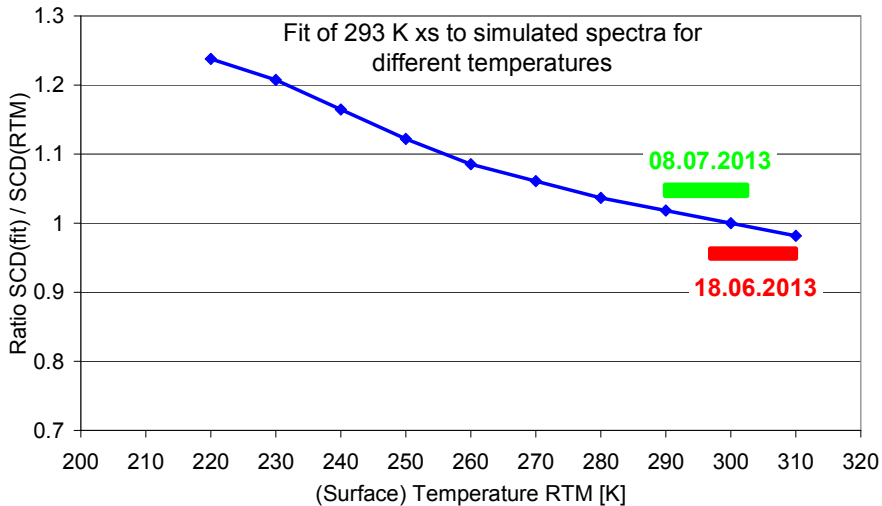
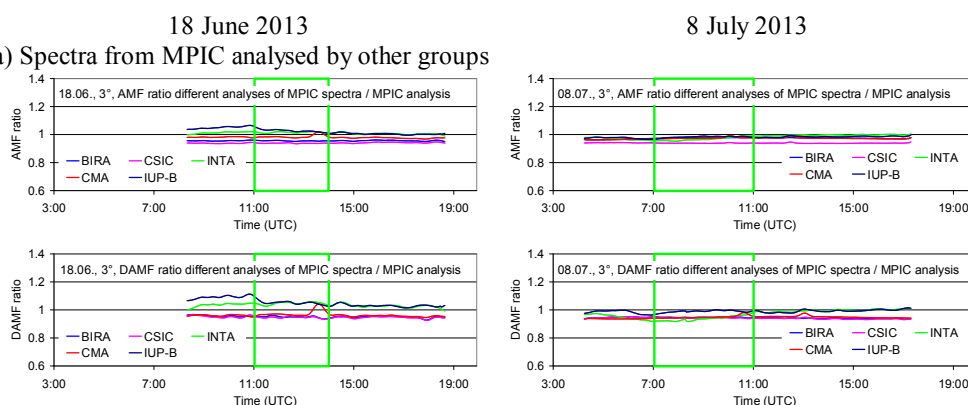


Fig. 13 Ratio of the O<sub>4</sub> dAMF obtained from simulated spectra for different surface temperatures by the corresponding O<sub>4</sub> dAMFs derived from radiative transfer simulations. The results represent MAX-DOAS observations at low elevation angles (2° to 3°).



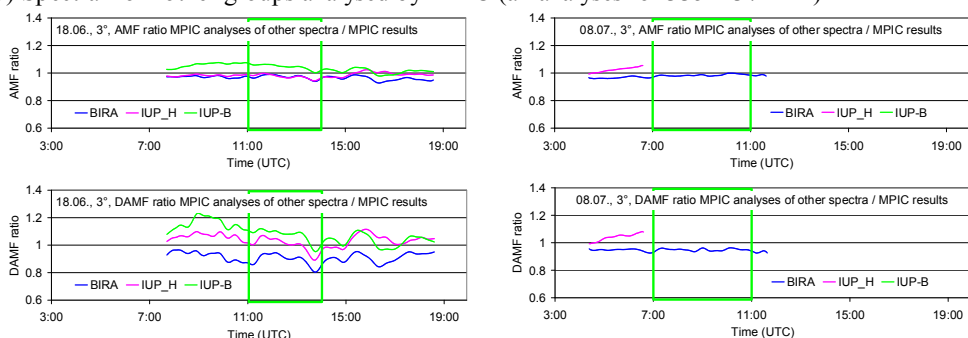
1647  
1648

1649 a) Spectra from MPIC analysed by other groups



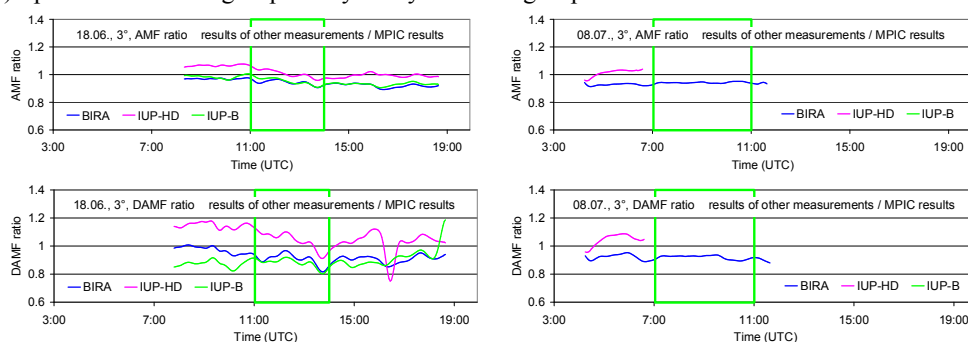
1650  
1651

b) Spectra from other groups analysed by MPIC (all analyses for 335 – 374 nm)



1652  
1653

c) Spectra from other groups analysed by the same groups



1654  
1655  
1656  
1657  
1658  
1659  
1660  
1661  
1662  
1663  
1664

Fig. 14 a) Ratio of the O<sub>4</sub> (d)AMFs derived from MPIC spectra when analysed by other groups versus those analysed by MPIC for both selected days; b) Ratio of the O<sub>4</sub> (d)AMFs derived from spectra measured and analysed by other groups (using different wavelength ranges and settings) versus those for the MPIC instrument analysed by MPIC; c) Ratio of the O<sub>4</sub> (d)AMFs derived from spectra measured by other groups but analysed by MPIC versus those for the MPIC instrument analysed by MPIC (using the spectral range 335 – 374 nm for all instruments).

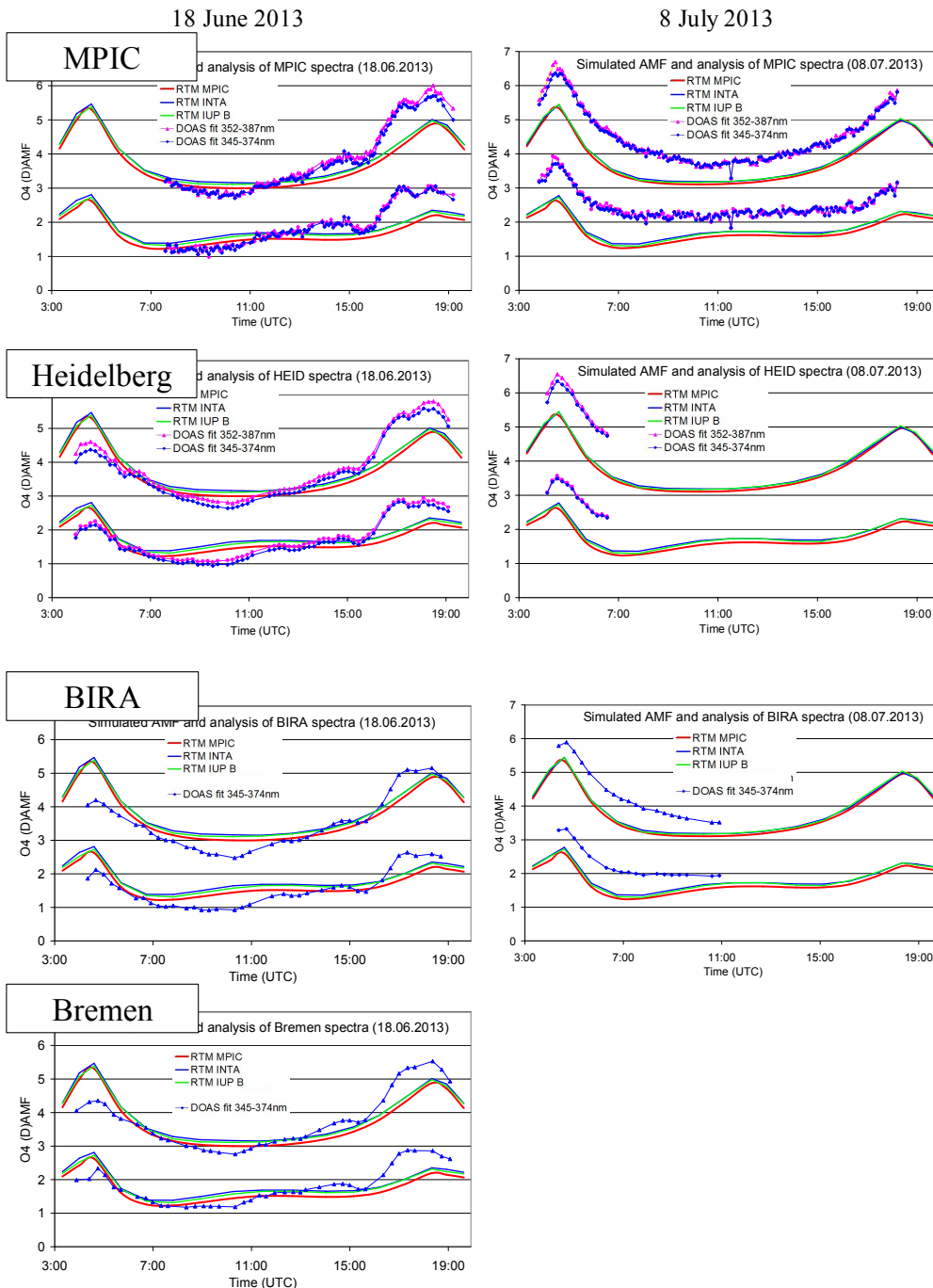


Fig. 15 Comparison of measured and simulated  $O_4$  (d)AMFs for both selected days. Measurements are from 4 different instruments, but analysed by MPIC using the standard settings (see Table 7). Simulations are performed by three different groups using Mie phase functions and otherwise the standard settings (see Table 6).



## Appendix A1 Settings used for the simulation of synthetic spectra

Table A1 Vertical resolution used in radiative transfer simulations for different altitude ranges.

Lower boundary [km]	Upper boundary [km]	Vertical resolution [km]
0	0.5	0.02
0.5	2	0.1
2	12	0.2
12	25	1
25	45	2
45	100	5
100	1000	900

Table A2 Dependence of SZA and relative azimuth angle on time (UTC) for the standard viewing direction ( $51^\circ$  with respect to North).

Time (UTC)	SZA	RAZI
03:19	90	-0.1
04:00	85	7.7
04:36	80	14.2
05:42	70	26
06:44	60	37.5
07:48	50	50.1
08:54	40	66.2
10:16	30	94.6
11:26	26	129
12:40	30	163.3
14:02	40	191.8
15:09	50	207.9
16:11	60	220.5
17:14	70	232
18:20	80	243.8
18:56	85	250.3
19:38	90	258





Table A3 Trace gas profiles and cross sections used for the simulation of the synthetic spectra.

Trace gas	Vertical profile	Cross section (reference and T)
O <sub>4</sub>	Derived from temperature and pressure profiles during. 18.06.: average profiles 11:00 – 14:00 08.07.: average profiles 7:00 – 11:00	Thalman and Volkamer (2013) (203, 223, 253, 273, 293 K)*
HCHO	18.06.: 0-1000m, constant concentration of $2 \cdot 10^{11}$ molec/cm <sup>3</sup> (about 8 ppb) 08.07.: 0-1000m, constant concentration of $1 \cdot 10^{11}$ molec/cm <sup>3</sup> (about 4 ppb)	Meller and Moortgat (2000) (298 K)
NO <sub>2</sub>	Troposphere 18.06.: 0-500m, constant concentration of $4 \cdot 10^{11}$ molec/cm <sup>3</sup> (about 16 ppb) 08.07.: 0-500m, constant concentration of $2 \cdot 10^{11}$ molec/cm <sup>3</sup> (about 8 ppb) Stratosphere: Gaussian profile with maximum at 25 km, and FWHM of 16 km, VCD = $5 \cdot 10^{15}$ molec/cm <sup>2</sup>	Vandaele et al. (1997) (220, 294 K)
O <sub>3</sub>	Troposphere (0-8km): constant concentration $6 \cdot 10^{11}$ molec/cm <sup>3</sup> (about 24 ppb) Stratosphere: Gaussian profile with maximum at 22 km, and FWHM of 15 km, VCD = 314 DU	Serdyuchenko et al. (2014) (193 – 293 K in steps of 10 K)**

\*The temperature dependence is either considered or a constant temperature of 293 K is assumed (see text for details).

\*\*The temperature dependence was parameterised according to Paur and Bass (1984).

1697  
1698  
1699  
1700  
1701  
1702  
1703  
1704  
1705

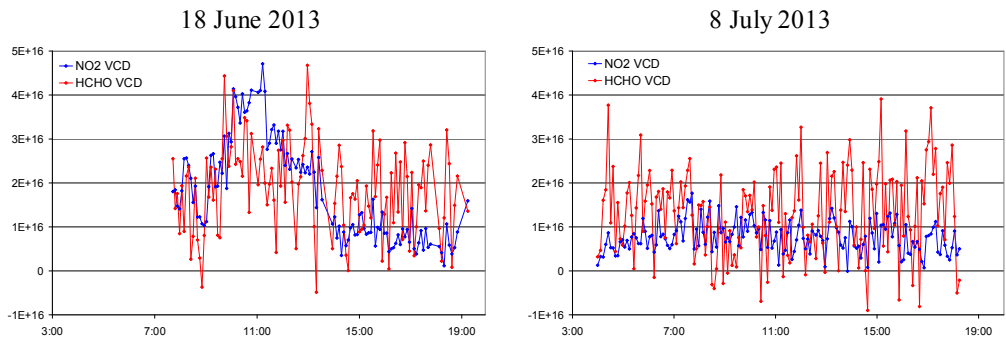


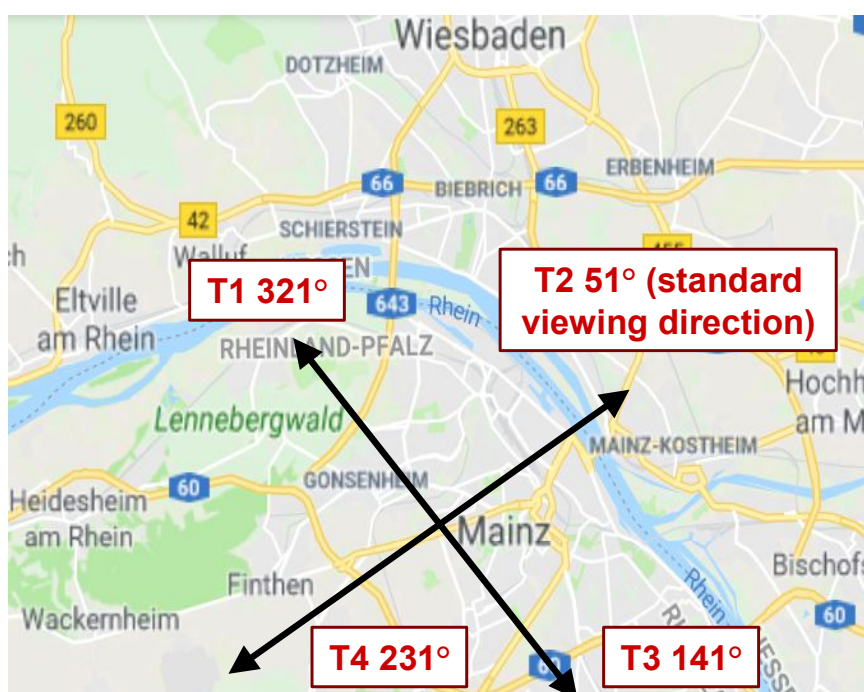
Fig. A1 Tropospheric VCDs of NO<sub>2</sub> (blue) and HCHO (red) derived from measurements at 30° elevation using the geometric approximation.

1706  
1707  
1708  
1709



1710 **Appendix A2 Comparison of measured and simulated O<sub>4</sub> (d)AMFs for all azimuth and**  
 1711 **elevation angles of the MPIC MAX-DOAS measurements.**  
 1712

1713 The settings for the simulation of the synthetic spectra are given in Table 6 and Tables A1,  
 1714 A2, and A3 in appendix 1. Measurements are analysed using the standard settings (see Table  
 1715 7).  
 1716  
 1717



1718  
 1719 Fig. A2 Azimuth viewing directions of the 4 telescopes (T1 to T4) of the MPIC MAX-DOAS  
 1720 instrument. The azimuth angles are defined with respect to North (map: © google maps).  
 1721  
 1722



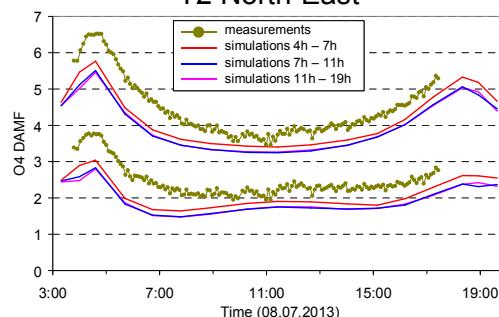
### T1 North-West

For T1 and T4 azimuth direction, no measurements at 1° elevation were possible due to obstacles.

### T4 South-West

For T1 and T4 azimuth direction, no measurements at 1° elevation were possible due to obstacles.

### T2 North-East



### T3 South-East

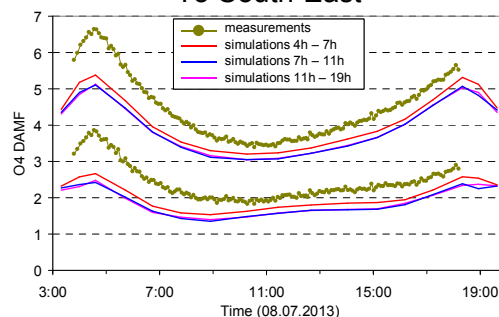
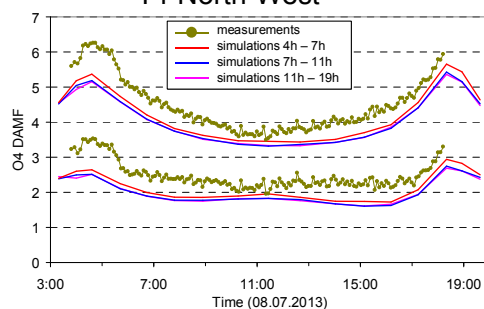
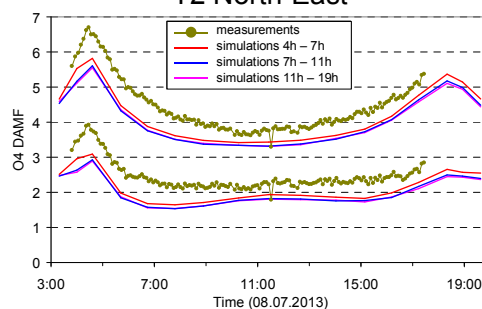


Fig. A3a Comparison results for 1° elevation angles on 8 July 2013. The upper lines indicate the O<sub>4</sub> AMFs, the lower lines the O<sub>4</sub> dAMFs (see also Fig. 2 and 3).

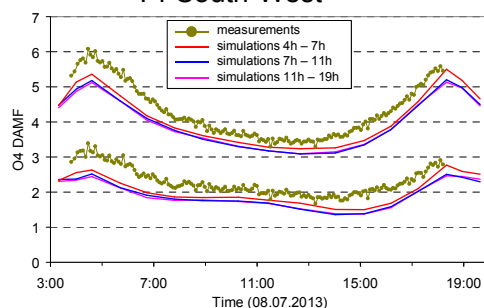
### T1 North-West



### T2 North-East



### T4 South-West



### T3 South-East

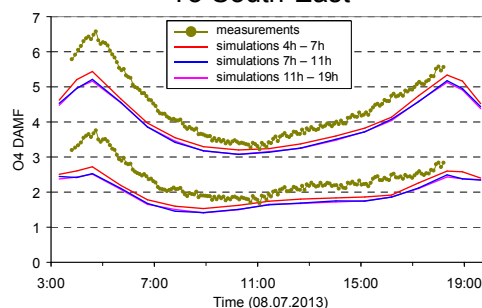
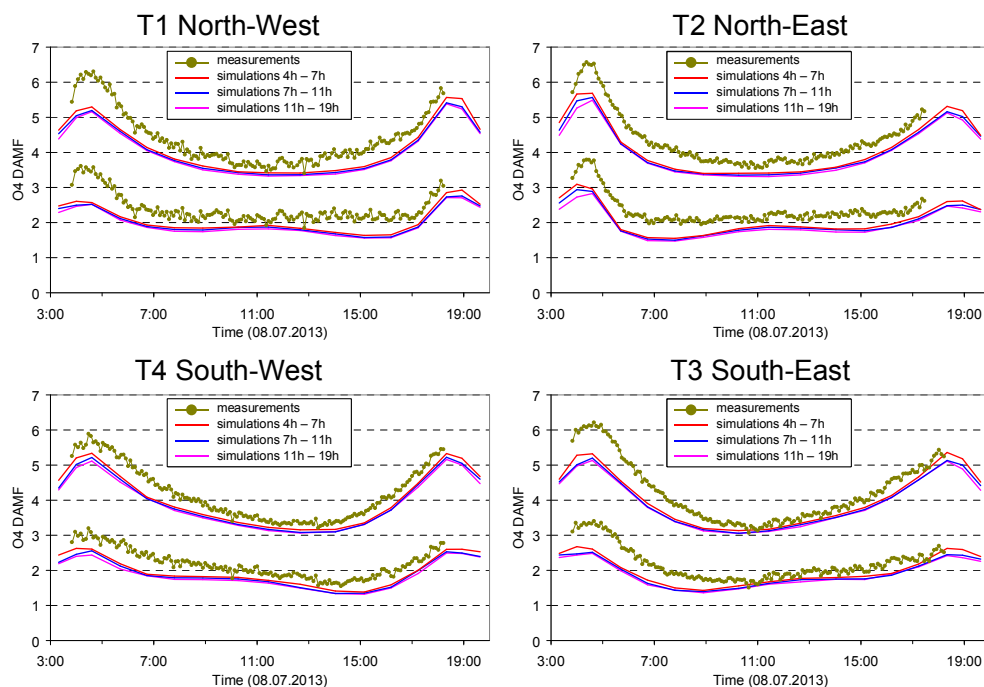


Fig. A3b Comparison results for 3° elevation angles on 8 July 2013.

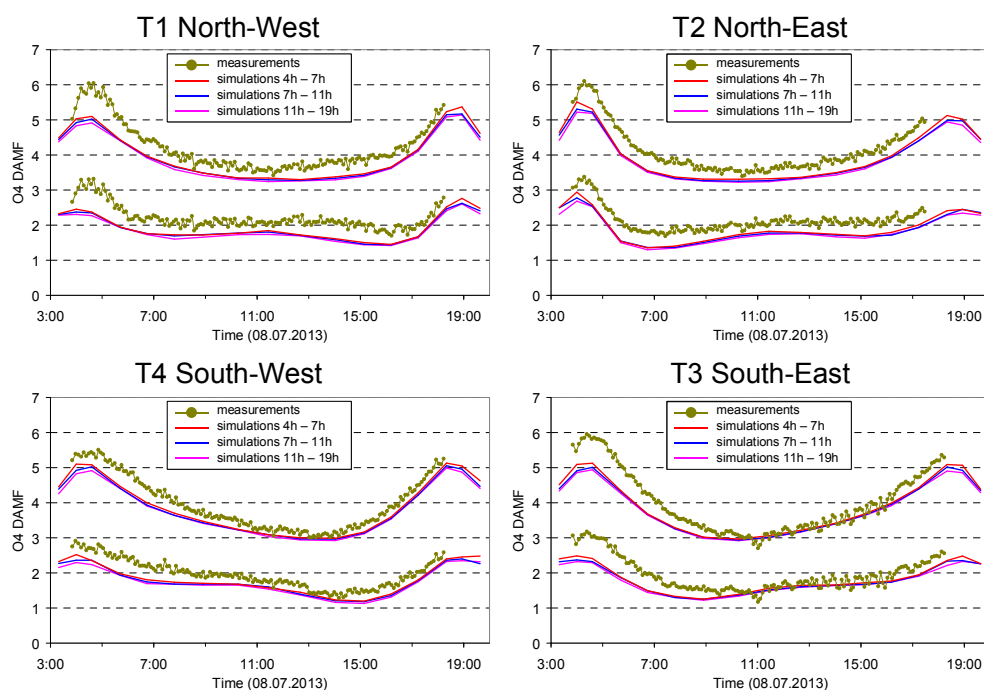


1729



1730  
1731  
1732

Fig. A3c Comparison results for 6° elevation angles on 8 July 2013.



1733  
1734  
1735

Fig. A3d Comparison results for 10° elevation angles on 8 July 2013.

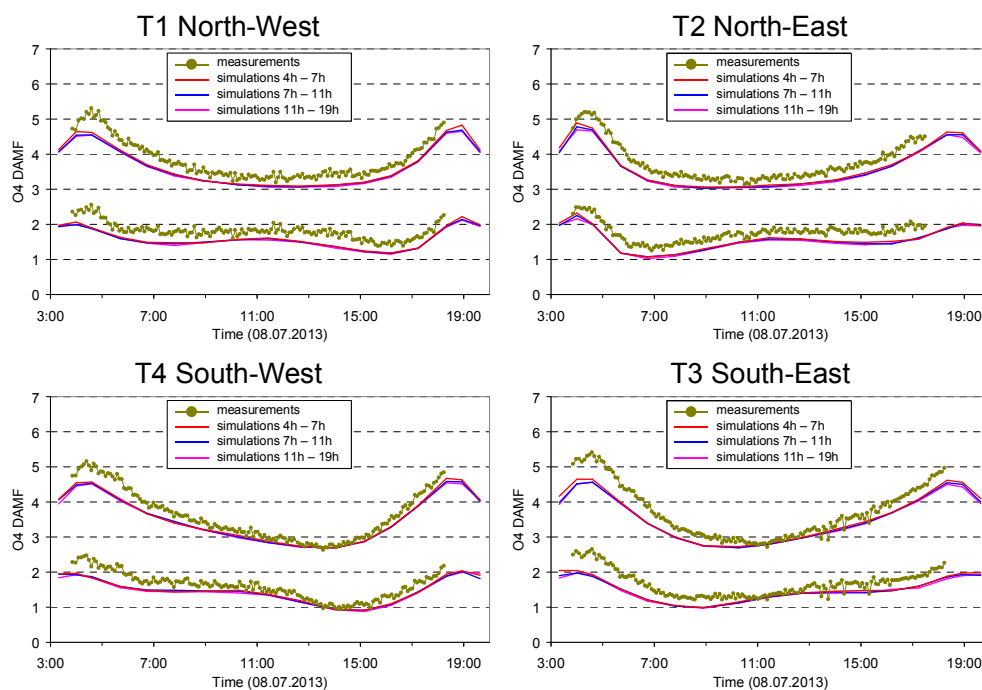


Fig. A3e Comparison results for 15° elevation angles on 8 July 2013.

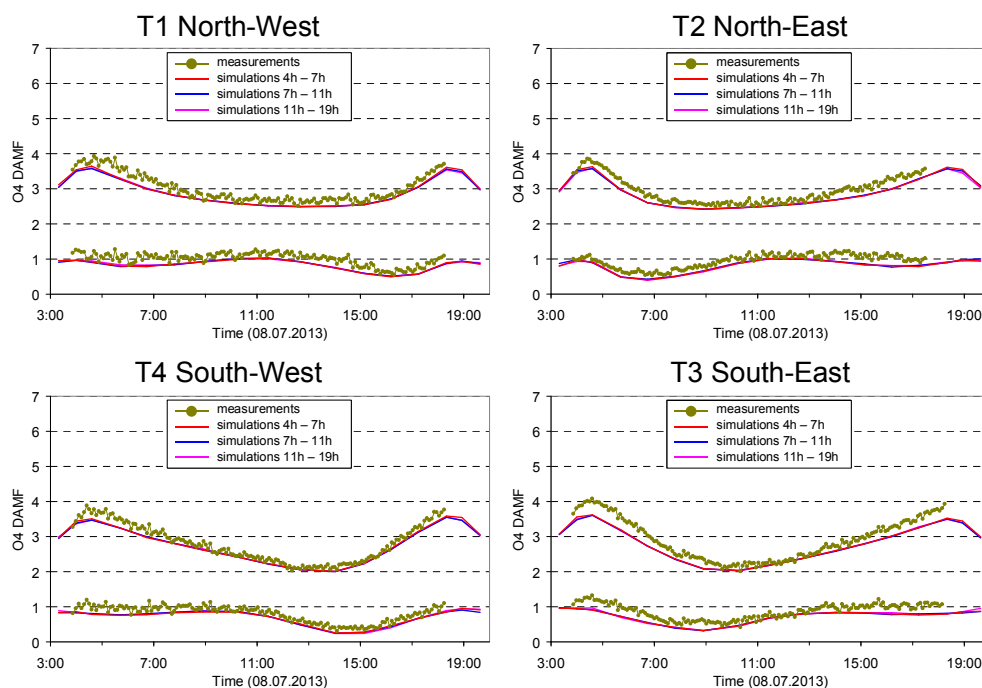


Fig. A3f Comparison results for 30° elevation angles on 8 July 2013.

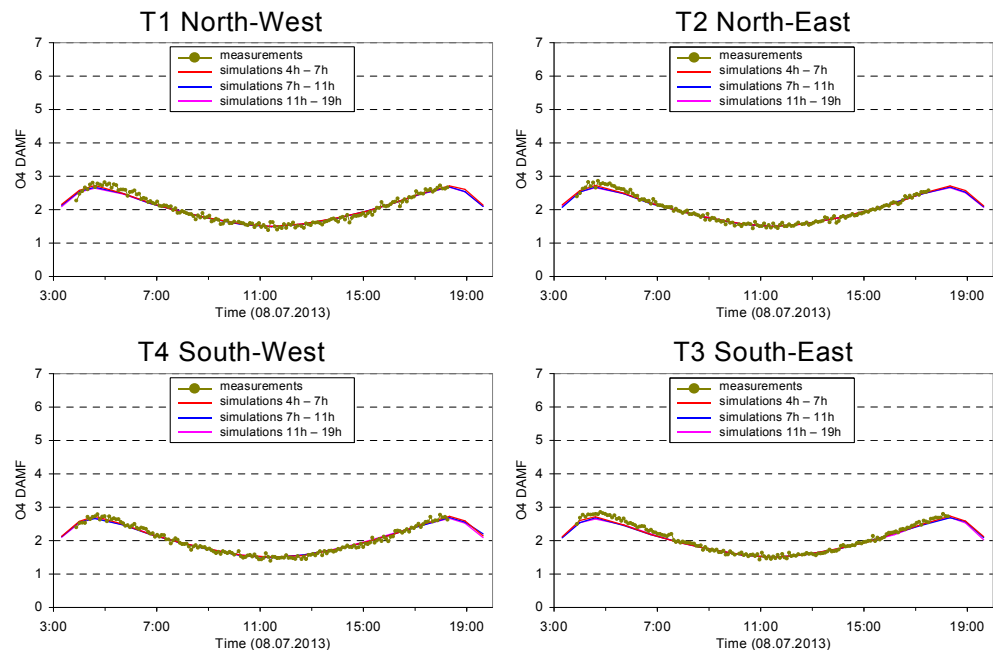


Fig. A3g Comparison results (only O<sub>4</sub> AMFs) for 90° elevation angles on 8 July 2013.

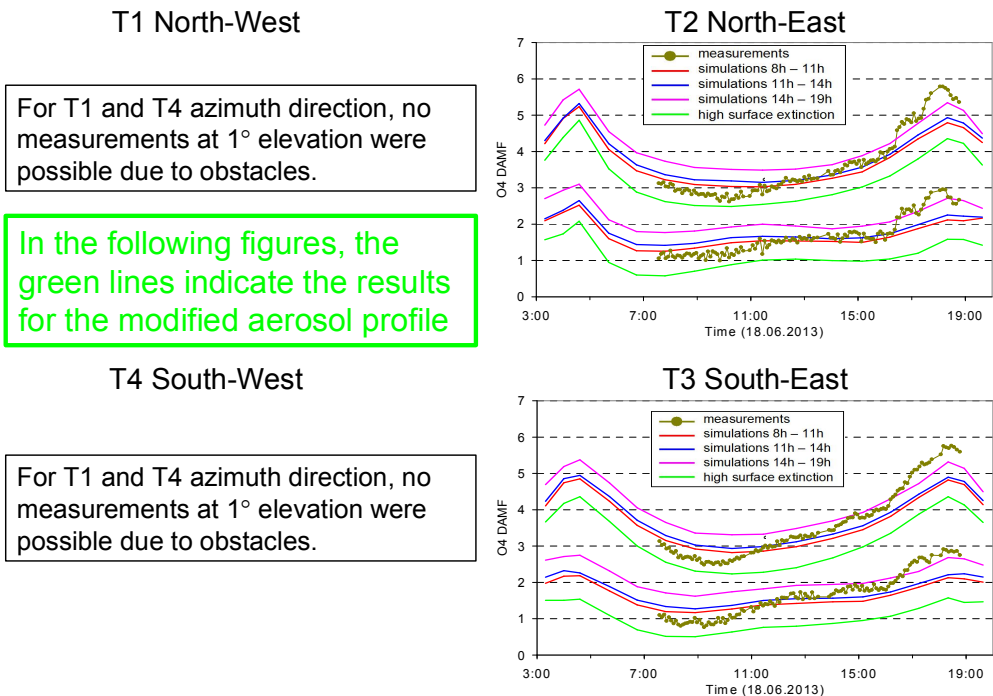


Fig. A4a Comparison results for 1° elevation angles on 18 June 2013 including the RTM results for the modified aerosol extinction profile (green line).



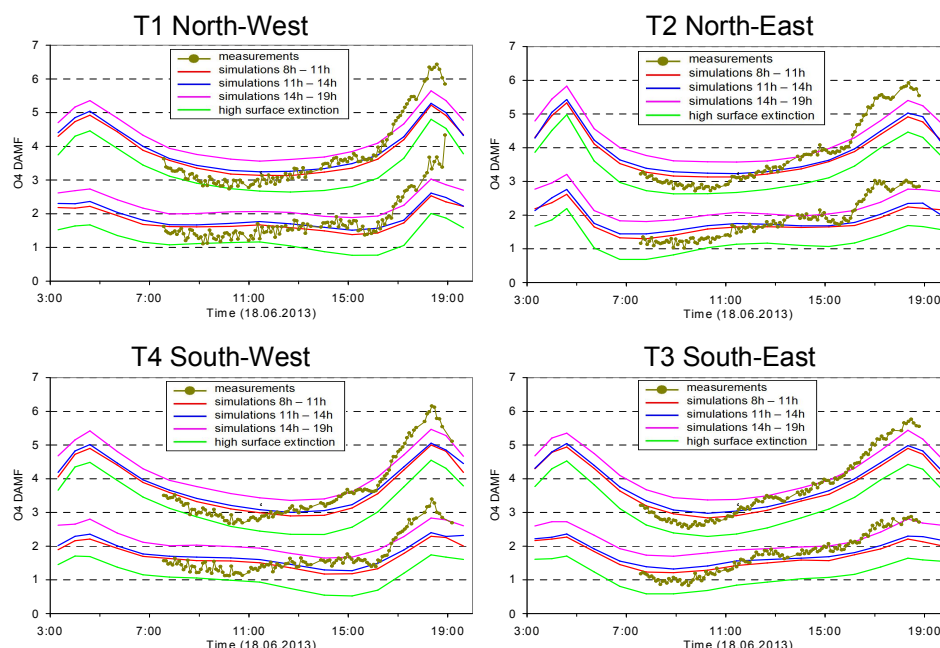


Fig. A4b Comparison results for 3° elevation angles on 18 June 2013 including the RTM results for the modified aerosol extinction profile (green line)..

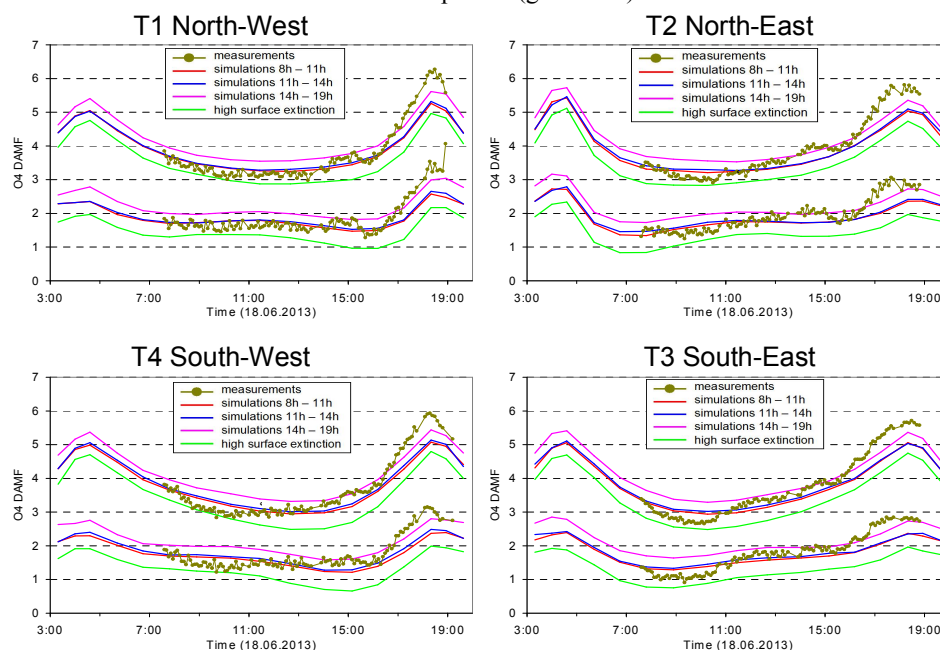


Fig. A4c Comparison results for 6° elevation angles on 18 June 2013 including the RTM results for the modified aerosol extinction profile (green line)..

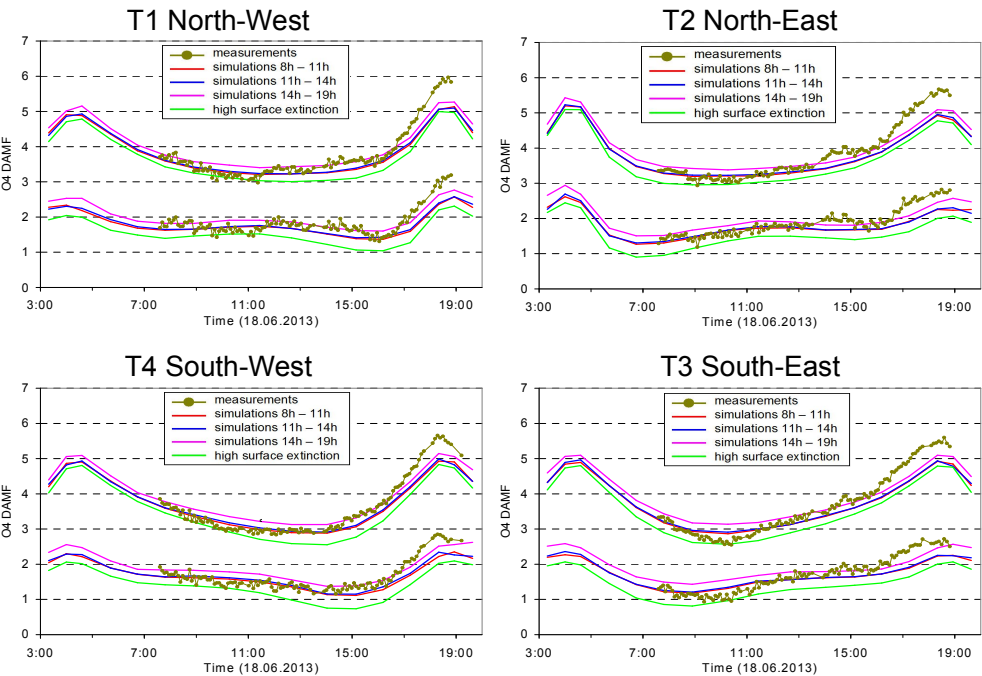


Fig. A4d Comparison results for 10° elevation angles on 18 June 2013 including the RTM results for the modified aerosol extinction profile (green line).

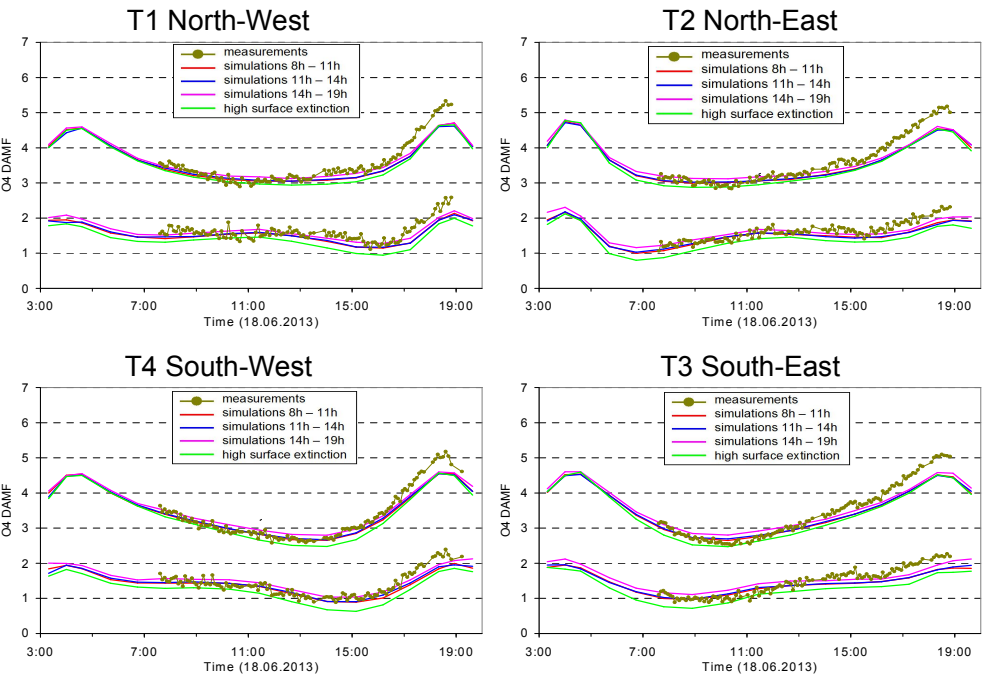


Fig. A4e Comparison results for 15° elevation angles on 18 June 2013 including the RTM results for the modified aerosol extinction profile (green line).

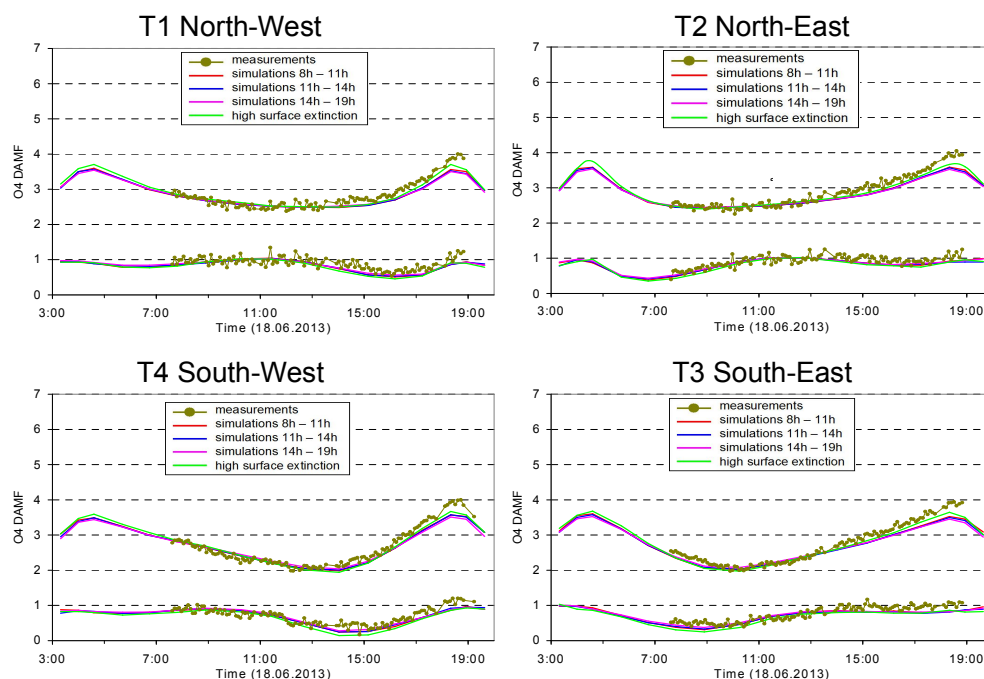


Fig. A4f Comparison results for 30° elevation angles on 18 June 2013 including the RTM results for the modified aerosol extinction profile (green line)..

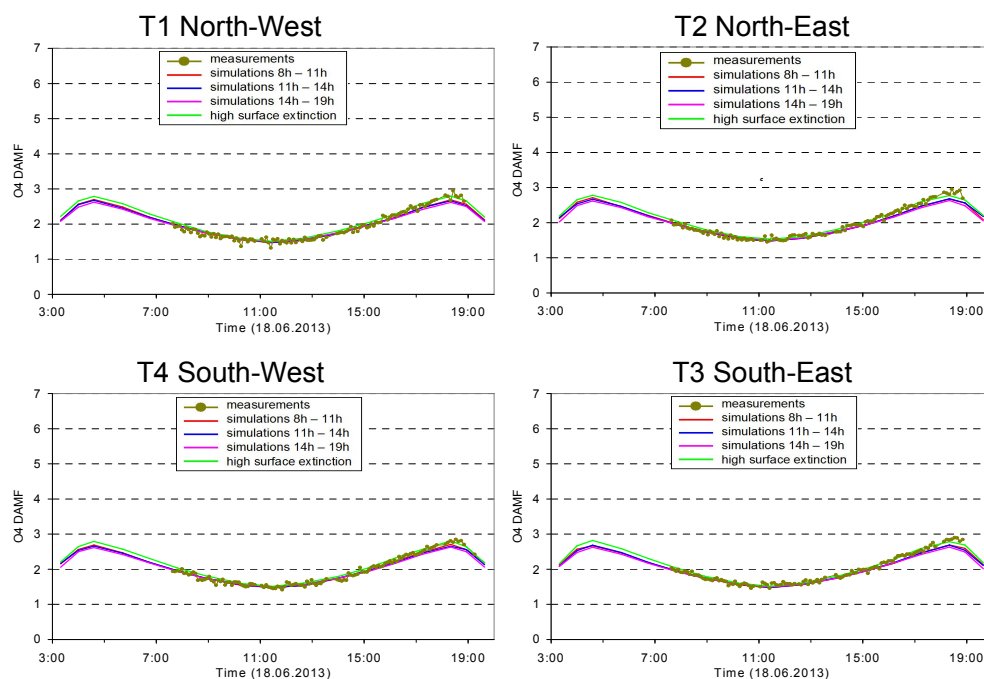


Fig. A4g Comparison results (only O<sub>4</sub> AMFs) for 90° elevation angles on 18 June 2013 including the RTM results for the modified aerosol extinction profile (green line).



Appendix A3 Comparison of the extracted height profiles of temperature, pressure and  $O_4$  concentration

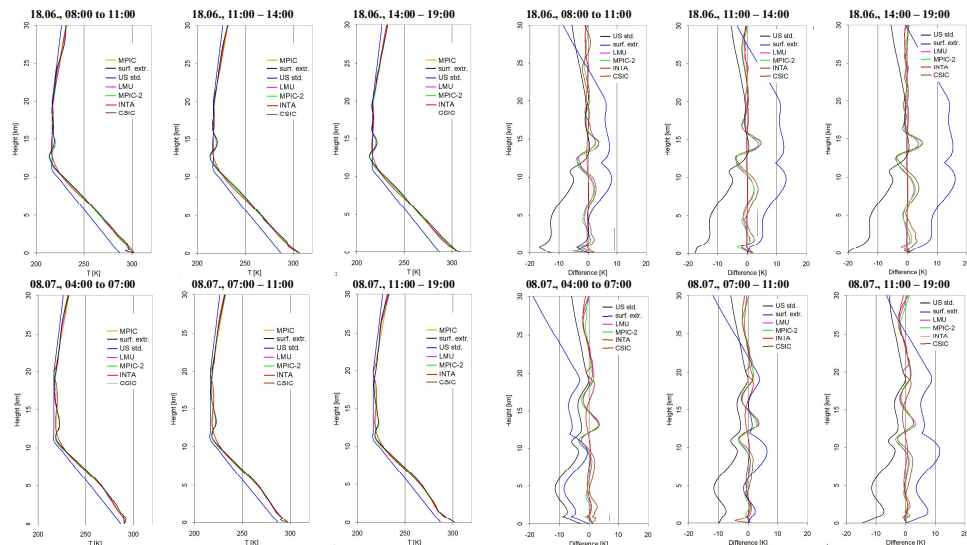


Fig. A5a Left: Comparison of temperature profiles extracted by the different groups (also shown are the profiles from the US standard atmosphere and the profiles extrapolated from the surface measurements). Right: Differences of these profiles compared to the MPIC standard extraction.

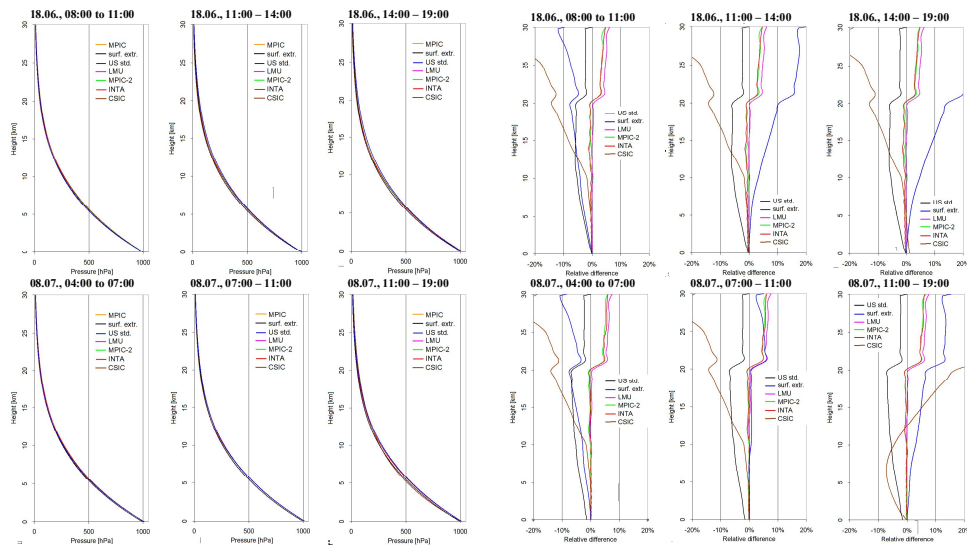
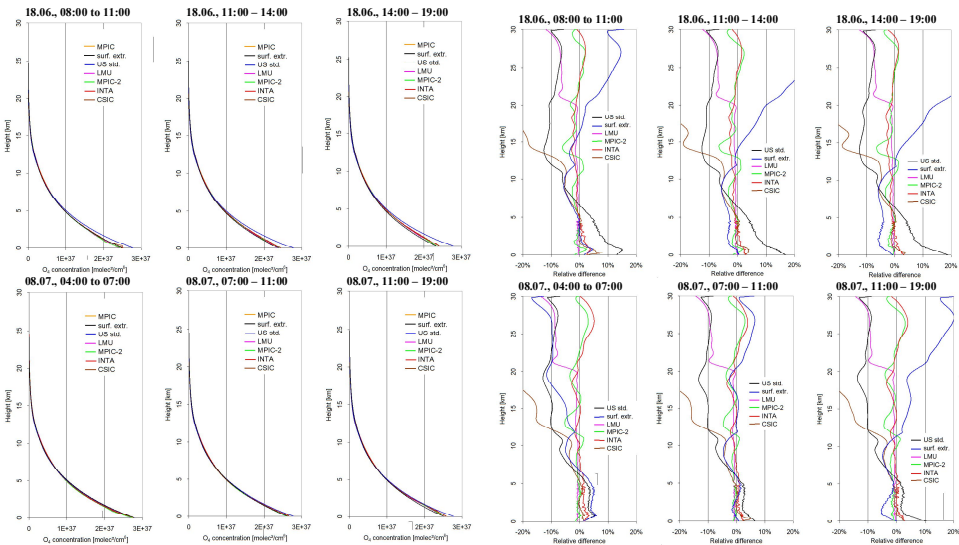


Fig. A5b Left: Comparison of pressure profiles extracted by the different groups (also shown are the profiles from the US standard atmosphere and the profiles extrapolated from the surface measurements). Right: Differences of these profiles compared to the MPIC standard extraction.



1786  
1787  
1788  
1789

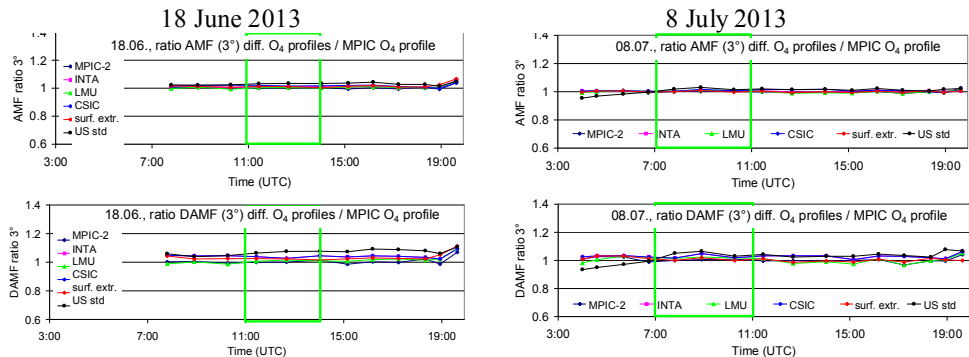


1790  
1791  
1792  
1793  
1794  
1795  
1796  
1797  
1798  
1799  
1800  
1801  
1802  
1803  
1804  
1805  
1806  
1807  
1808  
1809  
1810  
1811  
1812  
1813  
1814  
1815  
1816  
1817  
1818  
1819

Fig. A5c Left: Comparison of O<sub>4</sub> concentration profiles extracted by the different groups (also shown are the profiles from the US standard atmosphere and the profiles extrapolated from the surface measurements). Right: Differences of these profiles compared to the MPIC standard extraction.



1820 **Appendix A4 Results of the sensitivity studies of simulated and measured O<sub>4</sub> (d)MFs**  
1821  
1822



1823  
1824 Fig. A6 Ratio of the O<sub>4</sub> AMFs (top) and O<sub>4</sub> dAMFs (bottom) derived for different O<sub>4</sub> profiles  
1825 versus the standard O<sub>4</sub> profile (MPIC) for both selected days. Besides the O<sub>4</sub> profiles  
1826 extracted by the different groups, also the O<sub>4</sub> profiles derived from the US standard  
1827 atmosphere and for the extrapolation of the surface values are included.  
1828  
1829

1830  
1831  
1832  
1833  
1834  
1835 Table A4 Average ratios of O<sub>4</sub> (d)AMFs simulated for different O<sub>4</sub> profiles versus the results  
1836 for the standard settings (using the MPIC O<sub>4</sub> profiles) for the two middle periods on both  
1837 selected days.

	AMF ratios			dAMF ratios	
O <sub>4</sub> profile extraction	18 June 2013, 11:00 – 14:00	8 July 2013, 7:00 – 11:00		18 June 2013, 11:00 – 14:00	8 July 2013, 7:00 – 11:00
MPIC-2	1.00	1.00		1.00	1.00
INTA	1.01	1.01		1.02	1.01
LMU	1.00	1.00		1.01	1.02
CSIC	1.02	1.01		1.04	1.02
Lapse rate	1.01	1.00		1.02	1.01
US std. atm.	1.03	1.02		1.07	1.04

1838  
1839  
1840  
1841  
1842  
1843  
1844  
1845  
1846



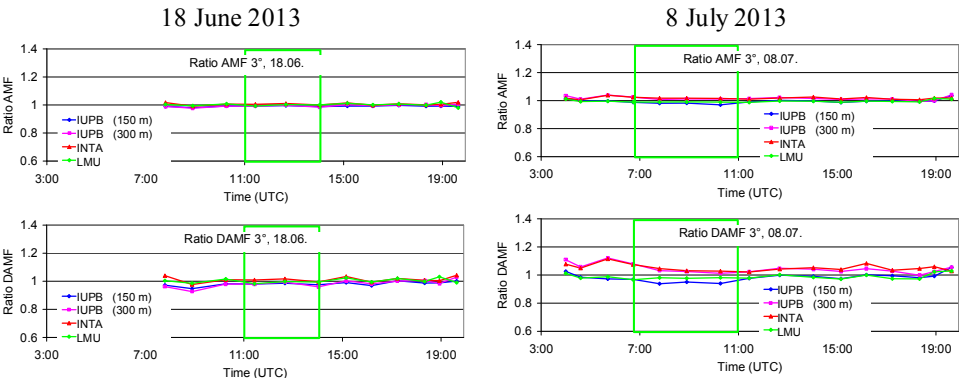


Fig. A7 Ratio of the O<sub>4</sub> AMFs (top) and O<sub>4</sub> dAMFs (bottom) derived for aerosol extinction profiles extracted by different groups versus the standard aerosol extinction profiles (MPIC) for both selected days.

Table A5 Average ratios of O<sub>4</sub> (d)AMFs simulated for different aerosol extinction profiles versus the results for the standard settings (using the MPIC aerosol extinction profiles) for the two middle periods on both selected days.

Aerosol profile extraction	AMF ratios			dAMF ratios	
	18 June 2013, 11:00 – 14:00	8 July 2013, 7:00 – 11:00		18 June 2013, 11:00 – 14:00	8 July 2013, 7:00 – 11:00
INTA	1.01	1.02		1.01	1.04
IUP-B 150 m	0.99	0.98		0.98	0.96
IUP-B 300 m	0.99	1.01		0.98	1.03
LMU	1.00	0.99		0.99	0.98

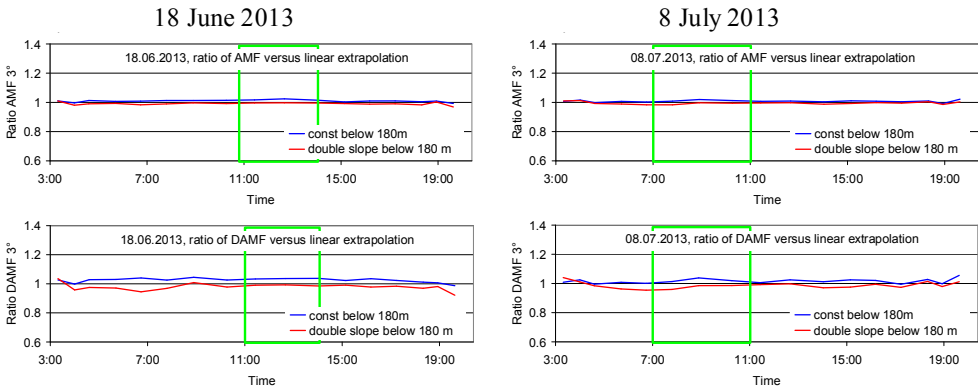


Fig. A8 Ratio of the O<sub>4</sub> AMFs (top) and O<sub>4</sub> dAMFs (bottom) derived for different extrapolations of the aerosol extinction profiles below 180 m versus those for the standard settings (linearly extrapolated profiles) for both selected days.



Table A6 Average ratios of  $O_4$  (d)AMFs simulated for aerosol extinction profiles with different extrapolations below 180 m versus the results for the standard settings (linear extrapolation) for the two middle periods on both selected days.

	AMF ratios			dAMF ratios	
Extrapolation below 180 m	18 June 2013, 11:00 – 14:00	8 July 2013, 7:00 – 11:00		18 June 2013, 11:00 – 14:00	8 July 2013, 7:00 – 11:00
Constant extinction	1.02	1.01		1.04	1.02
Double slope	1.00	0.99		0.99	0.98

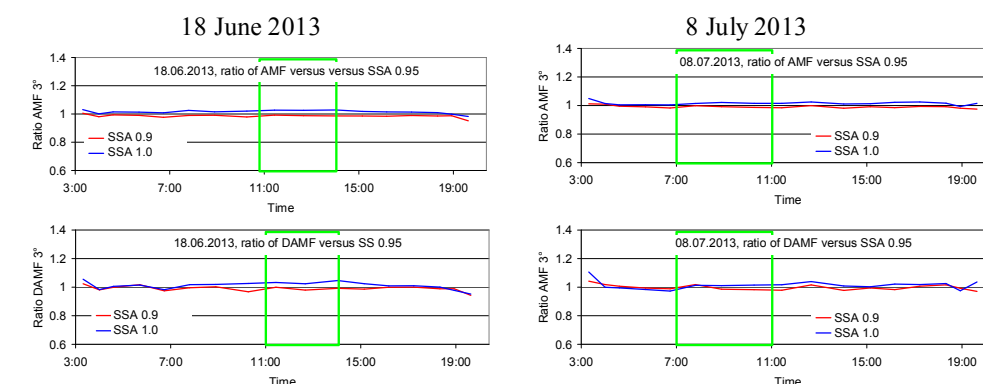


Fig. A9 Ratio of the  $O_4$  AMFs (top) and  $O_4$  dAMFs (bottom) derived for different aerosol single scattering albedos versus those for the standard settings (single scattering albedo of 0.95) for both selected days.

Table A7 Average ratios of  $O_4$  (d)AMFs simulated for different aerosol single scattering albedos (SSA) versus the results for the standard settings (single scattering albedo of 0.95) for the two middle periods on both selected days.

	AMF ratios			dAMF ratios	
Single scattering albedo	18 June 2013, 11:00 – 14:00	8 July 2013, 7:00 – 11:00		18 June 2013, 11:00 – 14:00	8 July 2013, 7:00 – 11:00
0.9	0.99	0.99		0.99	0.99
1.0	1.03	1.01		1.03	1.01

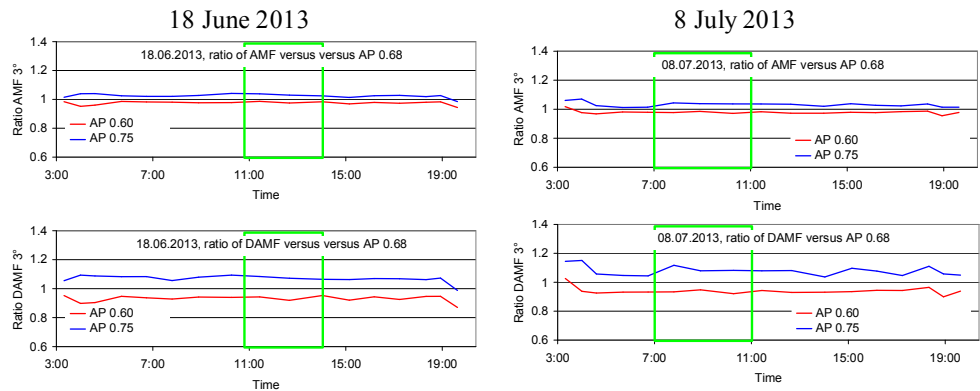


Fig. A10 Ratio of the  $O_4$  AMFs (top) and  $O_4$  dAMFs (bottom) derived for different aerosol phase functions (HG-parameterisation with different asymmetry parameters) versus those for the standard settings (asymmetry parameter of 0.68) for both selected days.

Table A8 Average ratios of  $O_4$  (d)AMFs simulated for different aerosol phase functions (HG-parameterisation with different asymmetry parameters (AP) versus the results for the standard settings (asymmetry parameter of 0.68) for the two middle periods on both selected days.

	AMF ratios			dAMF ratios	
Asymmetry parameter	18 June 2013, 11:00 – 14:00	8 July 2013, 7:00 – 11:00		18 June 2013, 11:00 – 14:00	8 July 2013, 7:00 – 11:00
0.6	0.98	0.98		0.94	0.94
0.75	1.03	1.03		1.08	1.07

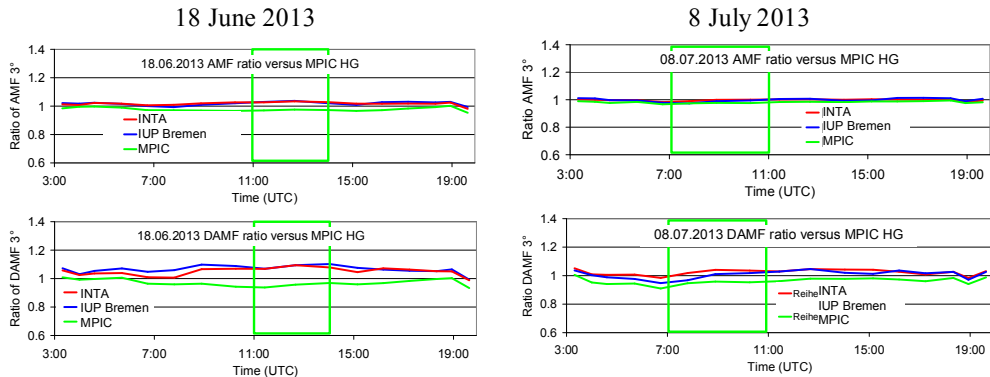


Fig. A11 Ratio of the  $O_4$  AMFs (top) and  $O_4$  dAMFs (bottom) simulated by INTA and IUP-Bremen and MPIC (SCIATRAN) for phase functions derived from the sun photometer measurements versus those simulated by MPIC using the Henyey Greenstein phase function for asymmetry parameter of 0.68 for both selected days.



Table A9 Average ratios of O<sub>4</sub> (d)AMFs simulated by INTA and IUP-Bremen and MPIC (SCIATRAN) for phase functions derived from the sun photometer measurements versus those simulated by MPIC using the Henyey Greenstein phase function for asymmetry parameter of 0.68 for the two middle periods on both selected days.

	AMF ratios			dAMF ratios	
Group (RTM)	18 June 2013, 11:00 – 14:00	8 July 2013, 7:00 – 11:00		18 June 2013, 11:00 – 14:00	8 July 2013, 7:00 – 11:00
INTA (LIDORT)	1.03	1.00		1.09	1.02
IUP-Bremen (SCIATRAN)	1.03	0.99		1.08	0.99
MPIC (SCIATRAN)	0.97	0.98		0.95	0.95

1911  
1912  
1913

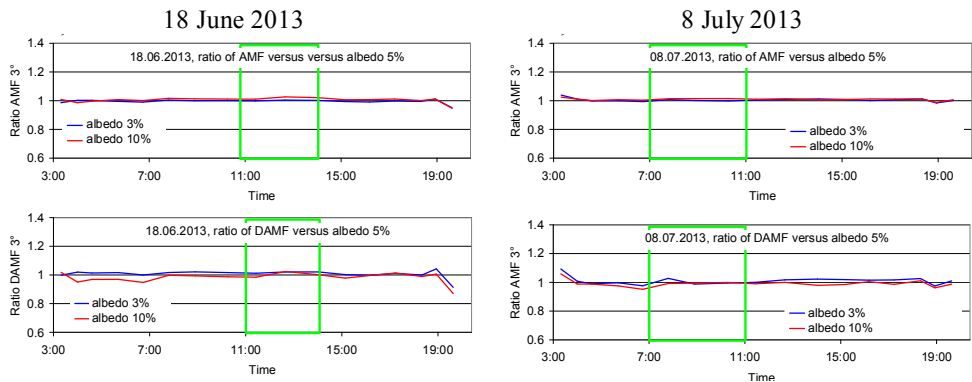


Fig. A12 Ratio of the O<sub>4</sub> AMFs (top) and O<sub>4</sub> dAMFs (bottom) for different surface albedos versus those for an albedo of 5 % for both selected days.

1914  
1915  
1916  
1917  
1918  
1919  
1920  
1921  
1922  
1923

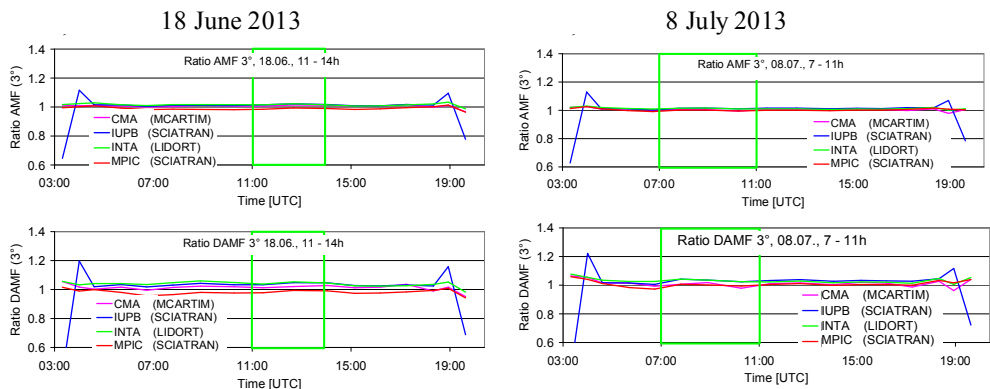
Table A12 Average ratios of O<sub>4</sub> (d)AMFs for different surface albedos versus those for an albedo of 5 % for the two middle periods on both selected days.

	AMF ratios			dAMF ratios	
Surface albedo	18 June 2013, 11:00 – 14:00	8 July 2013, 7:00 – 11:00		18 June 2013, 11:00 – 14:00	8 July 2013, 7:00 – 11:00
3 %	1.00	1.00		1.02	1.00
10 %	1.02	1.01		1.00	0.99

1924  
1925  
1926  
1927  
1928  
1929



1930



1931

1932

1933

1934

1935

1936

1937

1938

1939

1940

1941

Fig. A13 Ratio of the O<sub>4</sub> AMFs (top) and O<sub>4</sub> dAMFs (bottom) simulated by different groups using different radiative transfer models versus those for the MPIC simulations using MCARTIM for both selected days.

Table A11 Average ratios of O<sub>4</sub> (d)AMFs simulated by different groups using different radiative transfer models versus those for the MPIC simulations using MCARTIM for the two middle periods on both selected days.

Group (RTM)	AMF ratios			dAMF ratios	
	18 June 2013, 11:00 – 14:00	8 July 2013, 7:00 – 11:00		18 June 2013, 11:00 – 14:00	8 July 2013, 7:00 – 11:00
CMA (MACARTIM)	1.01	1.00		1.02	1.00
IUP-Bremen (SCIATRAN)	1.02	1.01		1.04	1.03
INTA (LIDORT)	1.02	1.01		1.05	1.03
MPIC (SCIATRAN)	0.99	1.00		0.99	1.00

1942

1943

1944

1945

1946

1947

1948

1949

1950

1951

1952

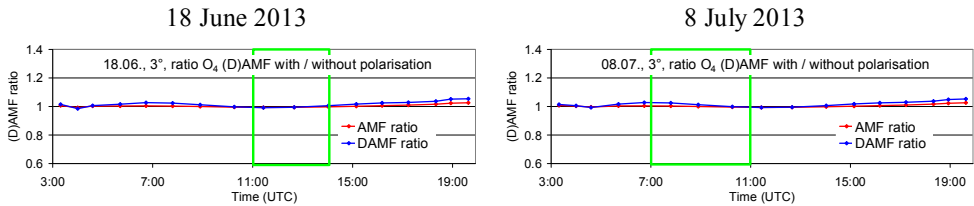
1953

1954

1955



1956



1957

1958

1959

1960

1961

1962

1963

1964

Fig. A14 Ratio of the O<sub>4</sub> (d)AMFs considering polarisation versus those without considering polarisation for both selected days.

Table A12 Average ratios of O<sub>4</sub> (d)AMFs considering polarisation versus those without considering polarisation for the two middle periods on both selected days.

	AMF ratios			dAMF ratios	
	18 June 2013, 11:00 – 14:00	8 July 2013, 7:00 – 11:00		18 June 2013, 11:00 – 14:00	8 July 2013, 7:00 – 11:00
Considering polarisation	1.00	1.00		1.00	1.01

1965

1966

1967

1968

1969

1970

1971

1972

1973

Table A13 Average ratios of O<sub>4</sub> (d)AMFs derived from synthetic spectra versus those obtained from radiative transfer simulations at 360 nm for the two middle periods on both selected days.

	AMF ratios			dAMF ratios	
Temperature dependence / noise	18 June 2013, 11:00 – 14:00	8 July 2013, 7:00 – 11:00		18 June 2013, 11:00 – 14:00	8 July 2013, 7:00 – 11:00
T dep. considered / no noise	1.01	1.02		1.01	1.00
no T dep. considered / no noise	1.00	1.01		1.00	1.00
no T dep. considered / noise	0.99	1.00		1.00	1.01

1974

1975

1976

1977

1978

1979

1980





1981

1982

1983

1984

1985

1986

1987

1988

1989

1990

1991

1992

1993

1994

1995

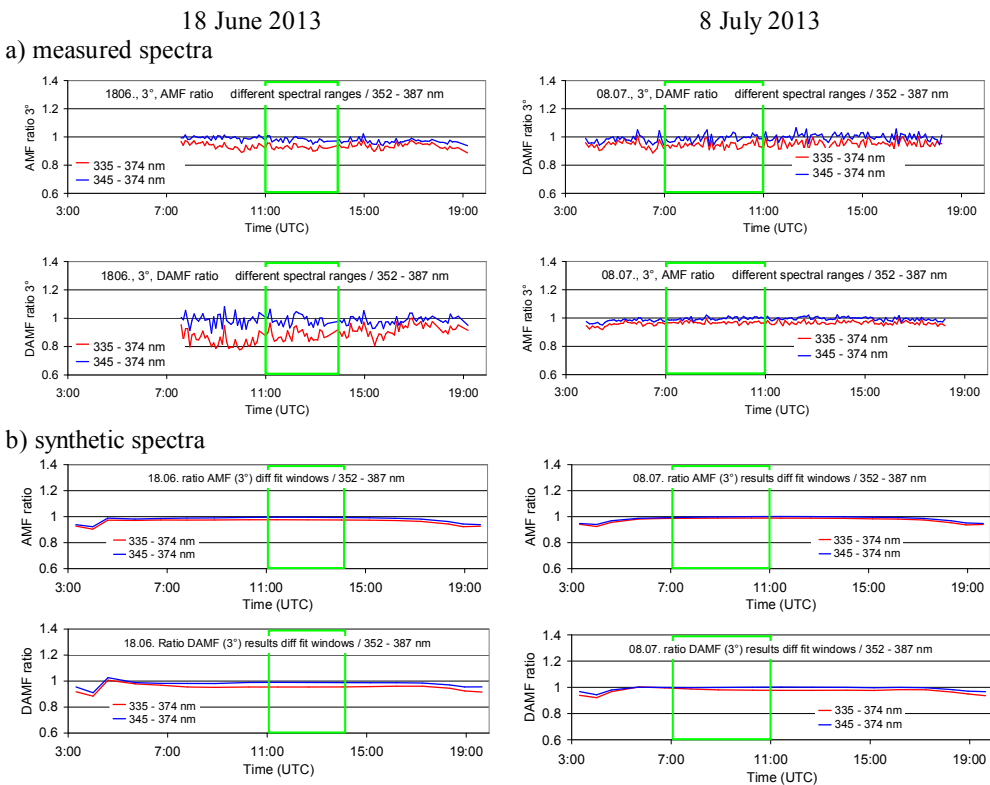


Fig. A15 Ratio of the O<sub>4</sub> (d)AMFs derived for different fit windows versus those for the standard fit window (352 – 387 nm) for both selected days (top: results for spectra measured by the MPIC instrument; bottom: results for synthetic spectra taking into account the temperature dependence of the O<sub>4</sub> cross section).

Table A14 Average ratios of O<sub>4</sub> (d)AMFs derived for different fit windows versus those for the standard fit window (352 – 387 nm) for the two middle periods on both selected days (top: results for spectra measured by the MPIC instrument; bottom: results for synthetic spectra taking into account the temperature dependence of the O<sub>4</sub> cross section).

	AMF ratios			dAMF ratios	
Spectral range	18 June 2013, 11:00 – 14:00	8 July 2013, 7:00 – 11:00		18 June 2013, 11:00 – 14:00	8 July 2013, 7:00 – 11:00
<b>Measured Spectra</b>					
335 – 374 nm	0.93	0.97		0.88	0.94
345 – 374 nm	0.98	1.00		0.99	0.99
<b>Synthetic Spectra</b>					
335 – 374 nm	0.98	0.99		0.95	0.98
345 – 374 nm	0.99	1.00		0.99	1.00



1996

1997

1998

1999

2000

2001

2002

2003

2004

2005

2006

2007

2008

2009

2010

2011

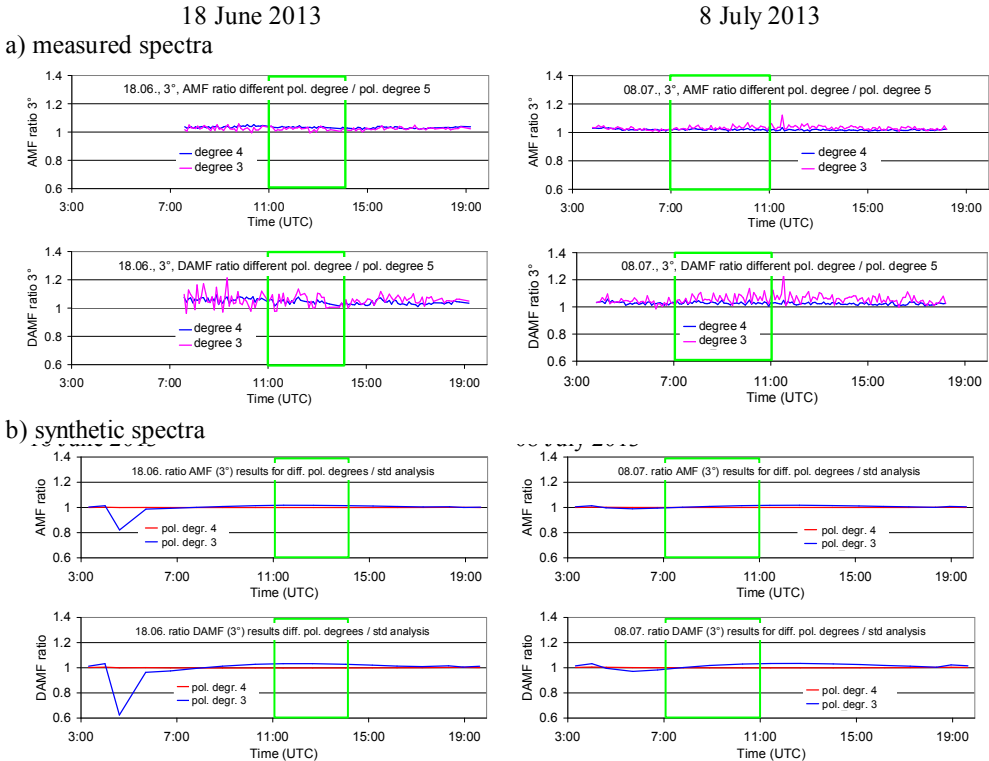


Fig. A16 Ratio of the O<sub>4</sub> (d)AMFs derived for different polynomials versus those for the standard analysis (polynomial degree 5) for both selected days (top: results for spectra measured by the MPIC instrument; bottom: results for synthetic spectra taking into account the temperature dependence of the O<sub>4</sub> cross section).

Table A15 Average ratios of O<sub>4</sub> (d)AMFs derived for different polynomials versus those for the standard analysis (polynomial degree 5) for the two middle periods on both selected days (top: results for spectra measured by the MPIC instrument; bottom: results for synthetic spectra taking into account the temperature dependence of the O<sub>4</sub> cross section).

	AMF ratios			dAMF ratios	
Degree of polynomial	18 June 2013, 11:00 – 14:00	8 July 2013, 7:00 – 11:00		18 June 2013, 11:00 – 14:00	8 July 2013, 7:00 – 11:00
Measured Spectra					
4	1.04	1.02		1.06	1.03
3	1.03	1.03		1.06	1.06
Synthetic Spectra					
4	1.00	1.00		1.00	1.00
3	1.02	1.01		1.03	1.01



2012

2013

2014

2015

2016

2017

2018

2019

2020

2021

2022

2023

2024

2025

2026

2027

2028

2029

2030

2031

2032

2033

2034

2035

2036

2037

2038

2039

2040

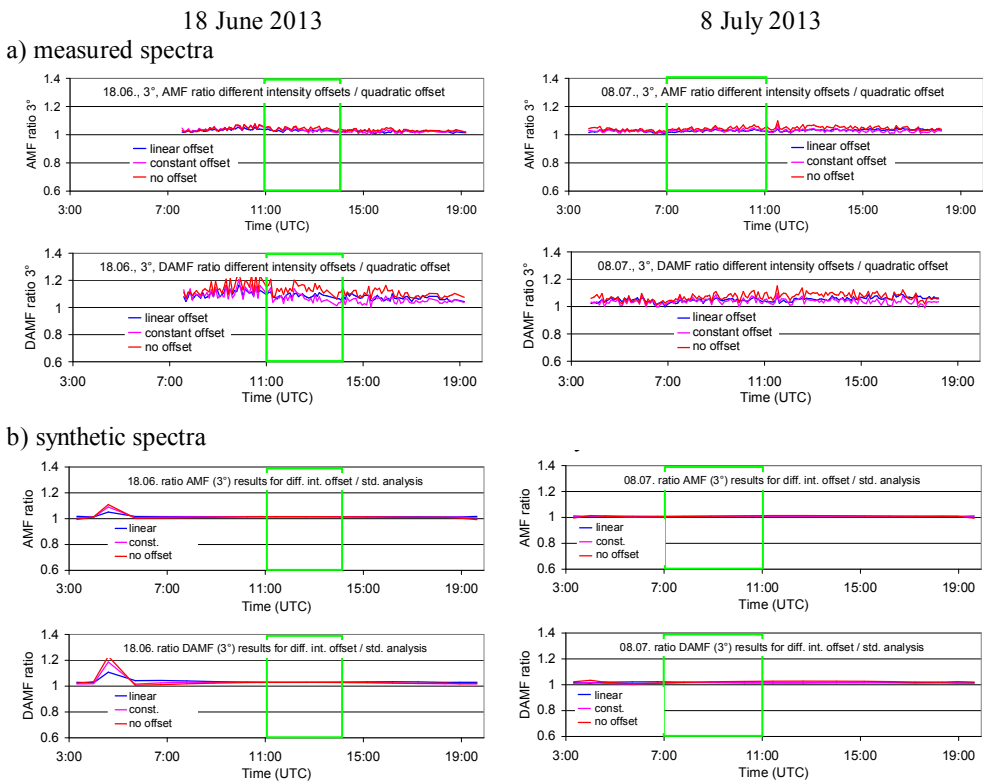


Fig. A17 Ratio of the  $O_4$  (d)AMFs derived for different intensity offsets versus those for the standard analysis (intensity offset of degree 2) for both selected days (top: results for spectra measured by the MPIC instrument; bottom: results for synthetic spectra taking into account the temperature dependence of the  $O_4$  cross section).



	AMF ratios			dAMF ratios	
Intensity offset	18 June 2013, 11:00 – 14:00	8 July 2013, 7:00 – 11:00		18 June 2013, 11:00 – 14:00	8 July 2013, 7:00 – 11:00
<b>Measured Spectra</b>					
Linear	1.04	1.03		1.11	1.05
Constant	1.05	1.03		1.11	1.04
No offset	1.05	1.05		1.16	1.07
<b>Synthetic Spectra</b>					
Linear	1.01	1.01		1.03	1.02
Constant	1.02	1.01		1.03	1.02
No offset	1.02	1.01		1.03	1.02

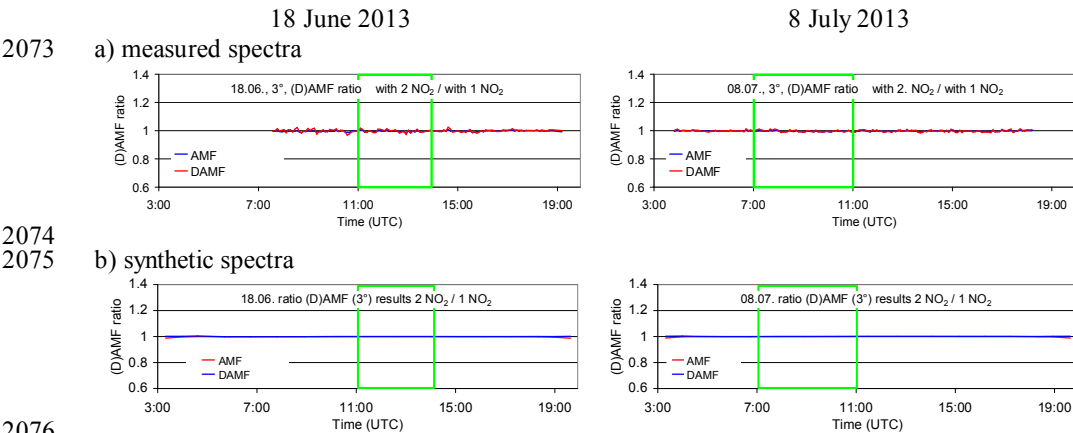
67



Table A17 Average ratios of O<sub>4</sub> (d)AMFs derived for the analysis with only one Ring spectrum versus those for the standard analysis (using two Ring spectra) for the two middle periods on both selected days (top: results for spectra measured by the MPIC instrument; bottom: results for synthetic spectra taking into account the temperature dependence of the O<sub>4</sub> cross section).

	AMF ratios			dAMF ratios	
Ring correction	18 June 2013, 11:00 – 14:00	8 July 2013, 7:00 – 11:00		18 June 2013, 11:00 – 14:00	8 July 2013, 7:00 – 11:00
<b>Measured Spectra</b>					
Only one Ring spectrum	1.02	0.99		1.01	0.99
<b>Synthetic Spectra</b>					
Only one Ring spectrum	1.01	1.01		1.01	1.01

2069  
2070  
2071  
2072



2074  
2075

Fig. A19 Ratio of the O<sub>4</sub> (d)AMFs derived for the analysis with a second NO<sub>2</sub> cross section (for 220 K) versus those for the standard analysis (only NO<sub>2</sub> cross section for 294 K) for both selected days (top: results for spectra measured by the MPIC instrument; bottom: results for synthetic spectra taking into account the temperature dependence of the O<sub>4</sub> cross section).

2076  
2077  
2078  
2079  
2080  
2081  
2082  
2083  
2084  
2085  
2086  
2087  
2088  
2089  
2090  
2091



Table A18 Average ratios of  $O_4$  (d)AMFs derived for the analysis with a second  $NO_2$  cross section (for 220 K) versus those for the standard analysis (only  $NO_2$  cross section for 294 K) for the two middle periods on both selected days (top: results for spectra measured by the MPIC instrument; bottom: results for synthetic spectra taking into account the temperature dependence of the  $O_4$  cross section).

	AMF ratios			dAMF ratios	
$NO_2$ cross sections	18 June 2013, 11:00 – 14:00	8 July 2013, 7:00 – 11:00		18 June 2013, 11:00 – 14:00	8 July 2013, 7:00 – 11:00
<b>Measured Spectra</b>					
294 & 220 K	1.00	1.00		1.00	1.00
<b>Synthetic Spectra</b>					
294 & 220 K	1.00	1.00		1.00	1.00

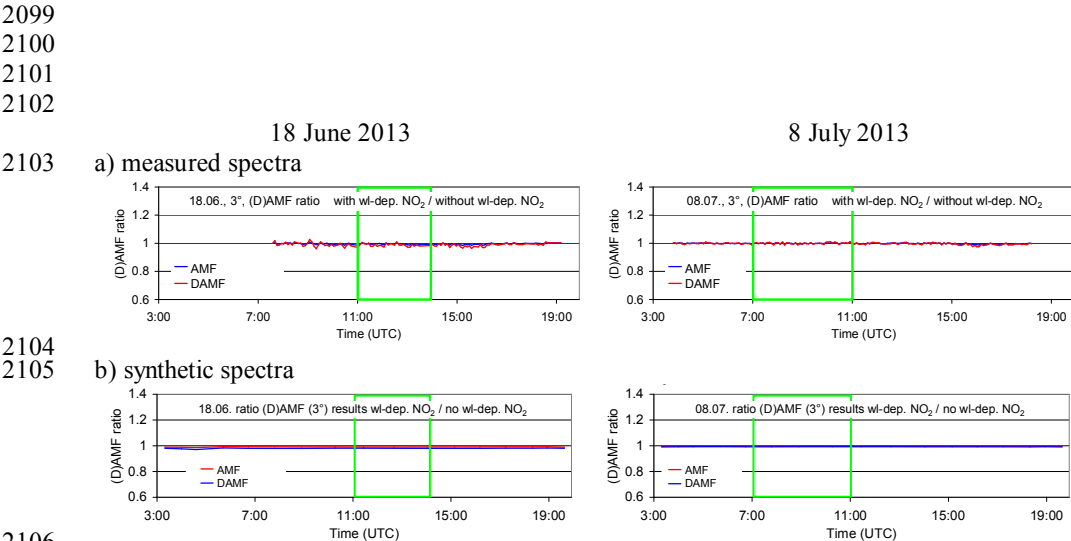


Fig. A20 Ratio of the  $O_4$  (d)AMFs derived for the analysis with a second  $NO_2$  cross section (cross section times wavelength) versus those for the standard analysis (only one  $NO_2$  cross section) for both selected days (top: results for spectra measured by the MPIC instrument; bottom: results for synthetic spectra taking into account the temperature dependence of the  $O_4$  cross section).

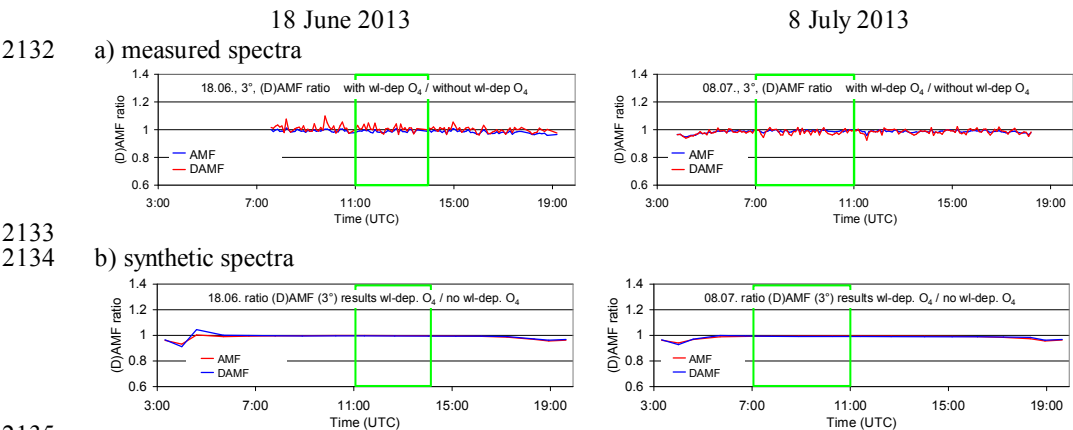




Table A19 Average ratios of O<sub>4</sub> (d)AMFs derived for the analysis with a second NO<sub>2</sub> cross section (cross section times wavelength) versus those for the standard analysis (only one NO<sub>2</sub> cross section) for the two middle periods on both selected days (top: results for spectra measured by the MPIC instrument; bottom: results for synthetic spectra taking into account the temperature dependence of the O<sub>4</sub> cross section).

	AMF ratios			dAMF ratios	
NO <sub>2</sub> wavelength dependence	18 June 2013, 11:00 – 14:00	8 July 2013, 7:00 – 11:00		18 June 2013, 11:00 – 14:00	8 July 2013, 7:00 – 11:00
<b>Measured Spectra</b>					
additional cross for wavelength dependence	1.00	1.00		0.99	1.00
<b>Synthetic Spectra</b>					
additional cross for wavelength dependence	0.99	1.00		0.98	0.99

2128  
2129  
2130  
2131



2133  
2134

Fig. A21 Ratio of the O<sub>4</sub> (d)AMFs derived for the analysis with a second O<sub>4</sub> cross section (accounting for the wavelength dependence) versus those for the standard analysis (only one O<sub>4</sub> cross section) for both selected days (top: results for spectra measured by the MPIC instrument; bottom: results for synthetic spectra taking into account the temperature dependence of the O<sub>4</sub> cross section).

2141  
2142  
2143  
2144  
2145  
2146



Table A20 Average ratios of O<sub>4</sub> (d)AMFs derived for the analysis with a second O<sub>4</sub> cross section (accounting for the wavelength dependence) versus those for the standard analysis (only one O<sub>4</sub> cross section) for the two middle periods on both selected days (top: results for spectra measured by the MPIC instrument; bottom: results for synthetic spectra taking into account the temperature dependence of the O<sub>4</sub> cross section).

	AMF ratios			dAMF ratios	
O <sub>4</sub> wavelength dependence	18 June 2013, 11:00 – 14:00	8 July 2013, 7:00 – 11:00		18 June 2013, 11:00 – 14:00	8 July 2013, 7:00 – 11:00
<b>Measured Spectra</b>					
additional cross for wavelength dependence	0.99	0.99		1.01	0.99
<b>Synthetic Spectra</b>					
additional cross for wavelength dependence	1.00	0.99		1.00	0.99

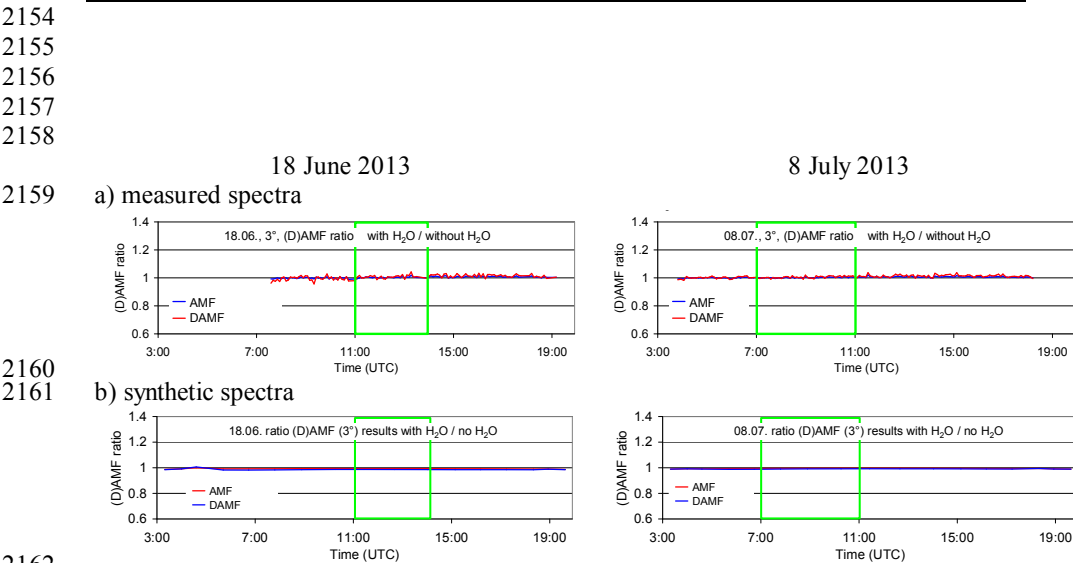


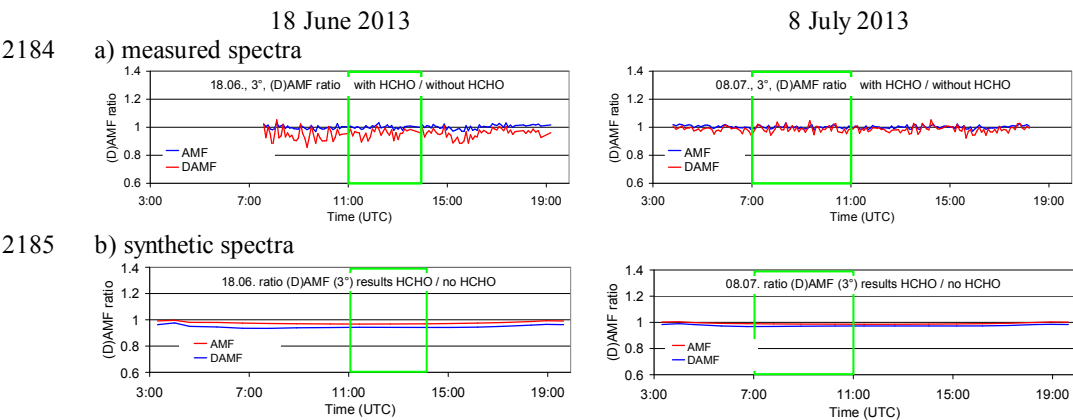
Fig. A22 Ratio of the O<sub>4</sub> (d)AMFs derived for the analysis including a H<sub>2</sub>O cross section versus those for the standard analysis (no H<sub>2</sub>O cross section) for both selected days (top: results for spectra measured by the MPIC instrument; bottom: results for synthetic spectra taking into account the temperature dependence of the O<sub>4</sub> cross section).



Table A21 Average ratios of O<sub>4</sub> (d)AMFs derived for the analysis including a H<sub>2</sub>O cross section versus those for the standard analysis (no H<sub>2</sub>O cross section) for the standard analysis (only one O<sub>4</sub> cross section) for the two middle periods on both selected days (top: results for spectra measured by the MPIC instrument; bottom: results for synthetic spectra taking into account the temperature dependence of the O<sub>4</sub> cross section).

	AMF ratios			dAMF ratios	
H <sub>2</sub> O cross section	18 June 2013, 11:00 – 14:00	8 July 2013, 7:00 – 11:00		18 June 2013, 11:00 – 14:00	8 July 2013, 7:00 – 11:00
<b>Measured spectra</b>					
H <sub>2</sub> O cross section included	1.00	1.00		1.01	1.01
<b>Synthetic Spectra</b>					
H <sub>2</sub> O cross section included	0.99	1.00		0.99	0.99

2181  
2182  
2183



2185

Fig. A23 Ratio of the O<sub>4</sub> (d)AMFs derived for the analysis including a HCHO cross section versus those for the standard analysis (no HCHO cross section) for both selected days (top: results for spectra measured by the MPIC instrument; bottom: results for synthetic spectra taking into account the temperature dependence of the O<sub>4</sub> cross section).

2186  
2187  
2188  
2189  
2190  
2191  
2192  
2193  
2194  
2195  
2196  
2197  
2198



2199  
 2200  
 2201  
 2202  
 2203  
 2204  
 2205

Table A22 Average ratios of O<sub>4</sub> (d)AMFs derived for the analysis including a HCHO cross section versus those for the standard analysis (no HCHO cross section) for the standard analysis (only one O<sub>4</sub> cross section) for the two middle periods on both selected days (top: results for spectra measured by the MPIC instrument; bottom: results for synthetic spectra taking into account the temperature dependence of the O<sub>4</sub> cross section).

	AMF ratios			dAMF ratios	
HCHO cross section	18 June 2013, 11:00 – 14:00	8 July 2013, 7:00 – 11:00		18 June 2013, 11:00 – 14:00	8 July 2013, 7:00 – 11:00
<b>Measured Spectra</b>					
HCHO cross section included	1.00	1.00		0.96	0.98
<b>Synthetic Spectra</b>					
HCHO cross section included	0.97	0.99		0.94	0.97

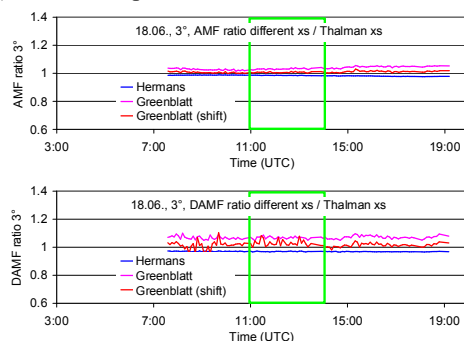
2206  
 2207  
 2208  
 2209  
 2210  
 2211  
 2212  
 2213  
 2214  
 2215  
 2216  
 2217  
 2218  
 2219  
 2220  
 2221  
 2222  
 2223  
 2224  
 2225  
 2226  
 2227  
 2228  
 2229  
 2230  
 2231  
 2232  
 2233  
 2234  
 2235



2236

2237

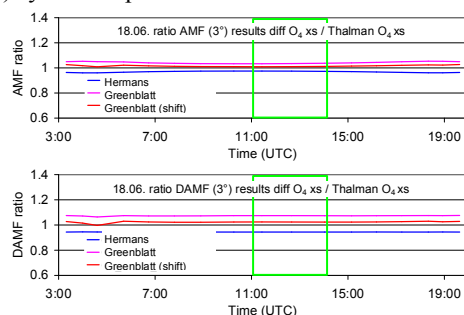
18 June 2013  
a) measured spectra



2238

2239

b) synthetic spectra



8 July 2013

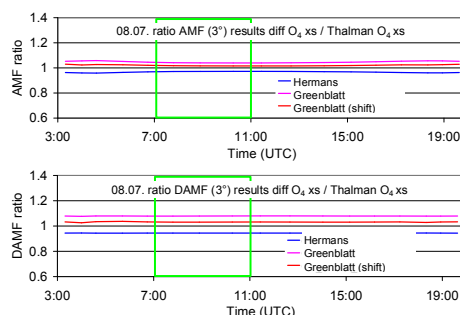
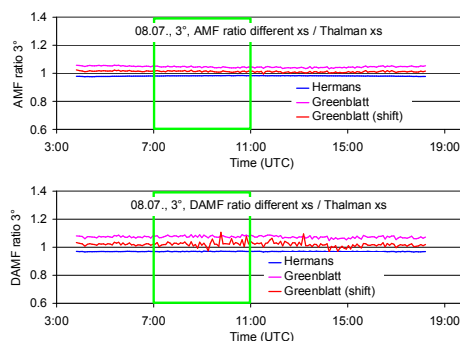


Fig. A24 Ratio of the  $O_4$  (d)AMFs derived for the analyses using different  $O_4$  cross sections versus those for the standard analysis (using the Thalman and Volkamer (2013) cross section) for both selected days (top: results for spectra measured by the MPIC instrument; bottom: results for synthetic spectra taking into account the temperature dependence of the  $O_4$  cross section).



Table A23 Average ratios of O<sub>4</sub> (d)AMFs derived for the analyses using different O<sub>4</sub> cross section versus those for the standard analysis (using the Thalman et al. cross section) for the standard analysis (only one O<sub>4</sub> cross section) for the two middle periods on both selected days (top: results for spectra measured by the MPIC instrument; bottom: results for synthetic spectra taking into account the temperature dependence of the O<sub>4</sub> cross section).

	AMF ratios			dAMF ratios	
O <sub>4</sub> cross section	18 June 2013, 11:00 – 14:00	8 July 2013, 7:00 – 11:00		18 June 2013, 11:00 – 14:00	8 July 2013, 7:00 – 11:00
<b>Measured spectra</b>					
Hermans	0.98	0.98		0.97	0.97
Greenblatt	1.03	1.04		1.07	1.08
Greenblatt shifted	1.01	1.01		1.03	1.03
<b>Synthetic Spectra</b>					
Hermans	0.97	0.97		0.94	0.94
Greenblatt	1.03	1.04		1.07	1.08
Greenblatt shifted	1.01	1.02		1.02	1.03

2271  
2272  
2273

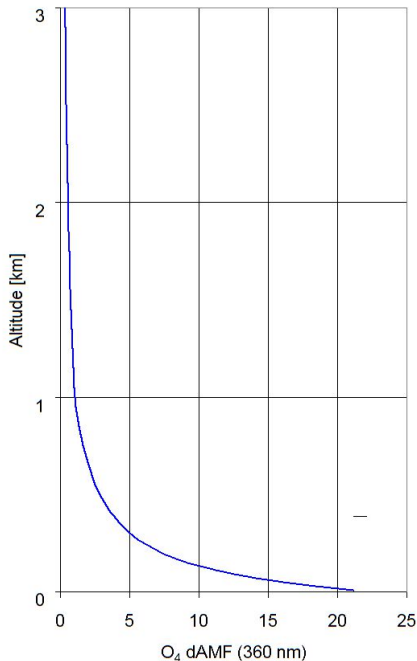


Fig. 25 O<sub>4</sub> differential box-AMFs (with 20m vertical resolution) used for the simulation of the temperature-dependent O<sub>4</sub> absorption spectra. They are averages of radiative transfer simulations for several scenarios. Simulations are performed for a surface albedo of 6 %, aerosol profiles with constant extinction between 0 and 1000m and different AOD (0.1, 0.3, 0.7) and for all combinations of SZA (40, 60°), relative azimuth angles (0, 90, 180°) and elevation angles (2° and 3°).

2274



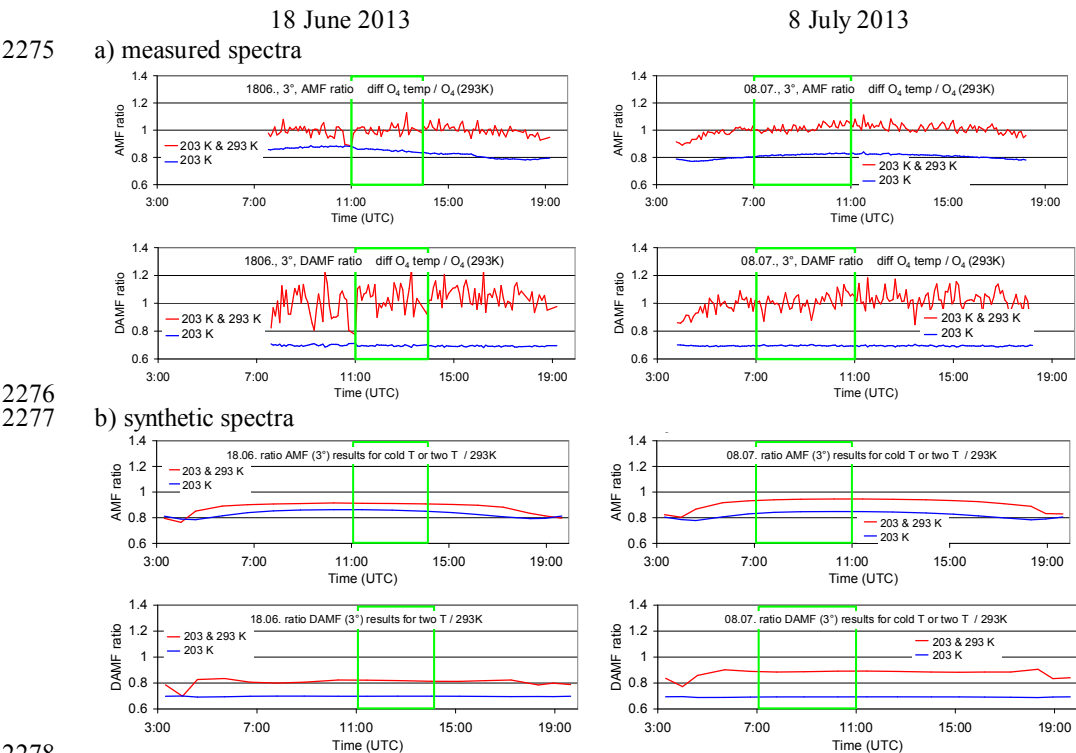


Fig. A26 Ratio of the O<sub>4</sub> (d)AMFs derived for O<sub>4</sub> cross sections at different temperatures (either 203 K or both 203 and 293 K) versus those for the standard analysis (using the O<sub>4</sub> cross section for 293 K) for both selected days (top: results for spectra measured by the MPIC instrument; bottom: results for synthetic spectra taking into account the temperature dependence of the O<sub>4</sub> cross section).



Table A24 Average ratios of O<sub>4</sub> (d)AMFs derived O<sub>4</sub> cross sections at different temperatures (either 203 K or both 203 and 293 K) versus those for the standard analysis (using the O<sub>4</sub> cross section for 293 K) for the two middle periods on both selected days (top: results for spectra measured by the MPIC instrument; bottom: results for synthetic spectra taking into account the temperature dependence of the O<sub>4</sub> cross section). For the simultaneous fit of both temperatures also the results for the spectral range 345 – 374 nm (one O<sub>4</sub> absorption band) are included.

	AMF ratios			dAMF ratios	
O <sub>4</sub> cross sections	18 June 2013, 11:00 – 14:00	8 July 2013, 7:00 – 11:00		18 June 2013, 11:00 – 14:00	8 July 2013, 7:00 – 11:00
<b>Measured Spectra</b>					
203 K	0.85	0.82		0.70	0.70
203 & 293 K	1.00	1.02		1.04	1.01
203 & 293 K (345 – 374 nm)	0.91	1.04		0.95	1.02
<b>Synthetic Spectra</b>					
203 K	0.86	0.84		0.70	0.69
203 & 293 K	0.91	0.94		0.82	0.89
203 & 293 K (345 – 374 nm)	0.99	1.00		0.99	1.00

2312  
2313  
2314  
2315  
2316  
2317  
2318  
2319  
2320  
2321  
2322  
2323  
2324  
2325  
2326  
2327  
2328  
2329  
2330  
2331  
2332  
2333  
2334  
2335  
2336  
2337



2338

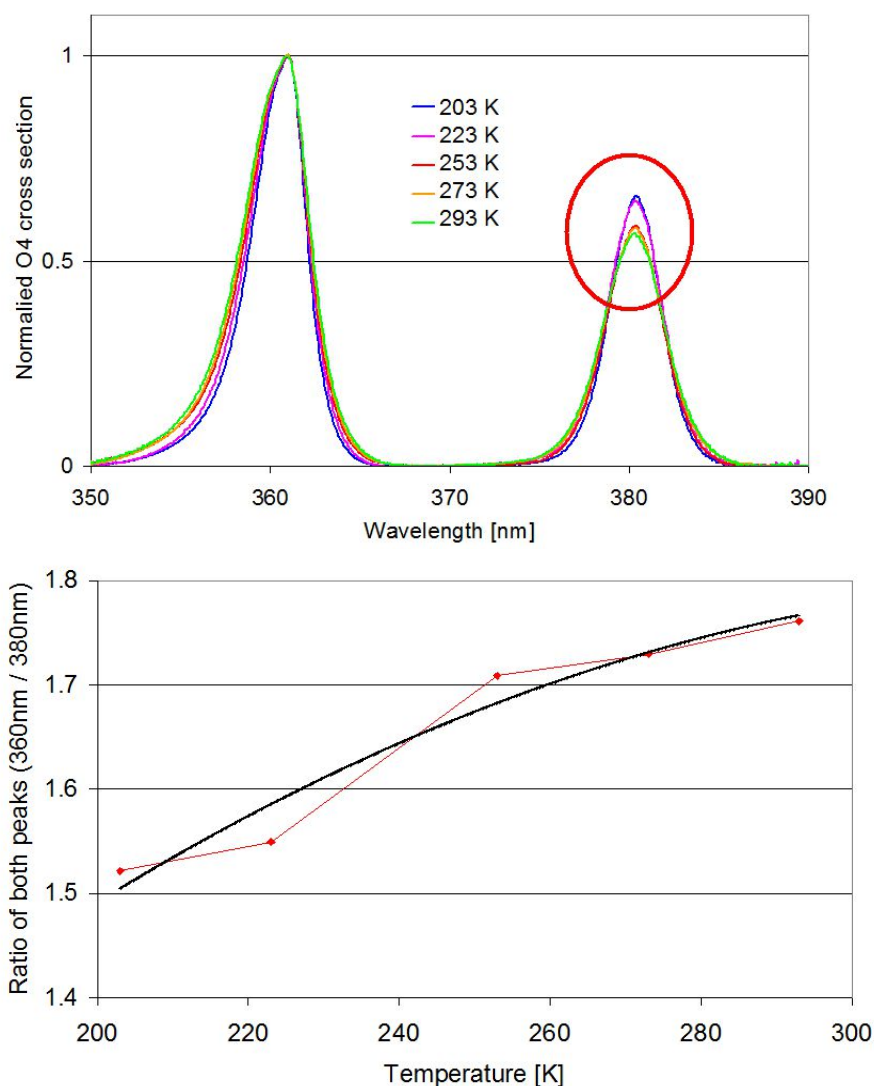
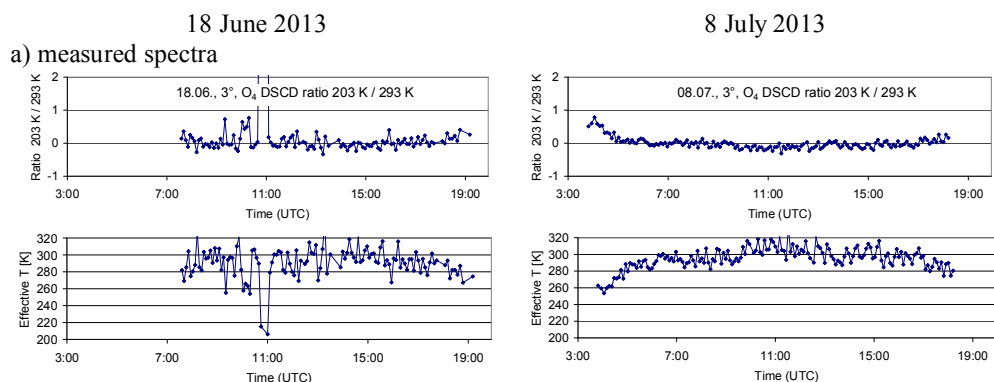


Fig. A27 Top: Comparison of the O<sub>4</sub> cross sections from Thalman and Volkamer (2013) for different temperatures. The cross sections are divided by the maximum values at 360 nm. After this normalisation, the resulting values at 380 nm fall into two groups (high values for 203 & 223K, low values for 253, 273, 293K). Bottom: Ratio of the peaks of the O<sub>4</sub> cross section at 360 nm and 380 nm as function of temperature (red points). The black curve is a fitted low order polynomial.

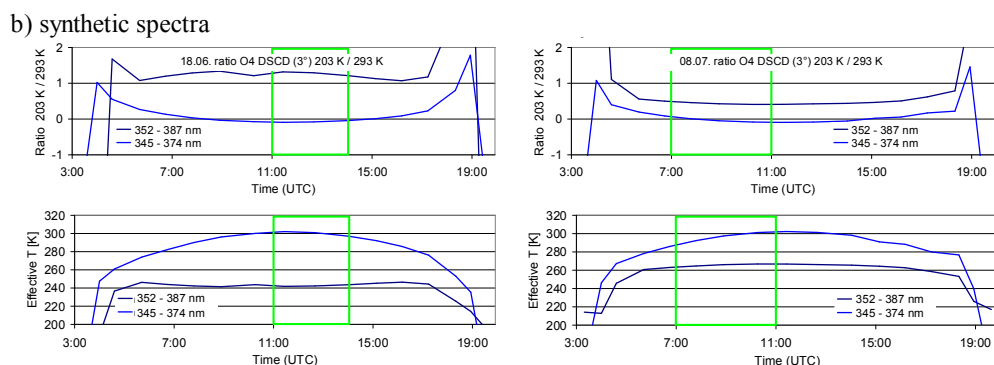


2352  
2353

2354



2355



2357

Fig. A28 Ratio of the derived O<sub>4</sub> dSCDs for 203 K and 293 K as well s the derived effective temperatures for the analyses with both cross sections included.

2358  
2359  
2360  
2361  
2362  
2363  
2364  
2365  
2366  
2367  
2368  
2369  
2370  
2371  
2372  
2373  
2374  
2375  
2376  
2377  
2378  
2379  
2380



Table A25 a) Average ratios of O<sub>4</sub> (d)AMFs derived from the analysis of MPIC spectra by different groups versus the analysis of MPIC spectra by MPIC (standard analysis). b) Average ratios of O<sub>4</sub> (d)AMFs derived from spectra of other groups analysed by MPIC versus the analysis of MPIC spectra by MPIC (using the same analysis settings and spectral range: 335 – 374 nm). c) Average ratios of O<sub>4</sub> (d)AMFs derived from spectra of other groups analysed by the same groups using individual analysis settings versus the analysis of MPIC spectra by MPIC (standard analysis).

MPIC (standard analysis).

	AMF ratios			dAMF ratios	
Measurements / Analysis	18 June 2013, 11:00 – 14:00	8 July 2013, 7:00 – 11:00		18 June 2013, 11:00 – 14:00	8 July 2013, 7:00 – 11:00
a) MPIC spectra analysed by other groups					
BIRA	0.96	0.98		0.95	0.95
IUP-B	1.03	0.98		1.05	0.99
INTA	1.02	0.97		1.05	0.94
CMA	0.97	0.98		0.98	0.95
CSIC	0.94	0.94		0.95	0.94
b) Other spectra analysed by MPIC (335 – 374 nm)					
BIRA	0.98	0.99		0.89	0.95
IUP-B	1.05			1.07	
IUP-HD	0.97			1.00	
c) Other spectra analysed by the same groups					
BIRA	0.94	0.94		0.91	0.92
IUP-B	0.95			0.88	
IUP-HD	1.01			1.04	



## Appendix A5 Extraction of aerosol extinction profiles

In this section, the procedure for the extraction of aerosol extinction profiles is described. The aerosol profiles are derived from the ceilometer measurements (yielding the profile information) in combination with the sun photometer measurements (yielding the vertically integrated aerosol extinction, the aerosol optical depth AOD).

The ceilometer raw data consist of range-corrected backscatter profiles averaged over 15 minutes. The profiles range from the surface to an altitude of 15360m with a height resolution of 15m. Here it is important to note that due to limited overlap of the outgoing Laser beam and the field of view of the telescope, no profile data is available below 180 m. The ceilometer profiles (hourly averages) are shown in Fig. A29 for both selected days.

The AERONET sun photometer data provide the AOD at different wavelengths (340, 360, 440, 500, 675, 870, and 1020 nm) in time intervals of 2 – 25 min if the direct sun is visible.

To determine profiles of aerosol extinction from the ceilometer backscatter data, several processing steps have to be performed. They are described in the sub-sections below.

### A) Smoothing and extrapolating of the ceilometer backscatter profiles

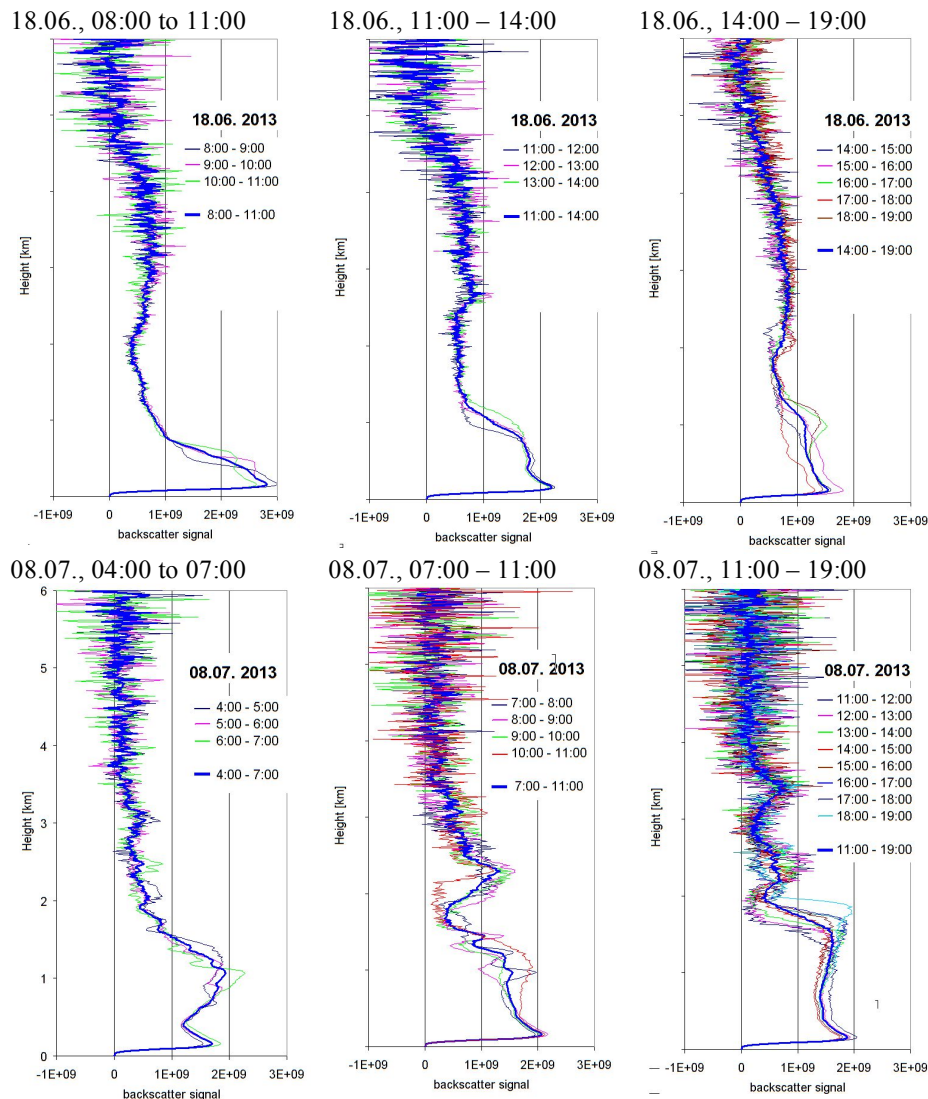
First, the ceilometer data are averaged over several hours to reduce the scatter. For that purpose on both days three time periods are identified, for which the backscatter profile show relatively small variations. The profiles for these periods are shown in Fig. A29. In addition to the temporal averaging, the profiles are also vertically smoothed above 2 km. Above altitudes between 5 to 6 km (depending on the period) the (smoothed) ceilometer backscatter profiles become zero. Thus the aerosol extinction profiles above these altitudes are set to zero. Below 180 m above the surface the ceilometer becomes ‘blind’ for the aerosol extinction because of the insufficient overlap between the outgoing laser beam and the field of view of the telescope. Thus the profiles have to be extrapolated down to the surface. This extrapolation constitutes an important source of uncertainty. To estimate the associated errors, the extrapolation is performed in three different ways:

- 1) The value below 180 m are set to the value measured at 180m.
- 2) The values below 180m are linearly extrapolated assuming the same slope below 180 m as between 180m and 240m.
- 3) The values below 180m are linearly extrapolated by the double slope between 180m and 240m.





2461



2462 Fig. A29 Range-corrected backscatter profiles (hourly averages) for the three selected periods  
2463 on both days. Also the averages over the whole periods are shown (thick lines).  
2464  
2465

2466 **B) Scaling of the Ceilometer profiles by sun photometer AOD at 1020 nm**

2467  
2468 The scaling of the ceilometer backscatter profiles by the AOD at 1020 nm is an intermediate  
2469 step, which is necessary for the correction of the aerosol self-extinction. The average AOD at  
2470 1020 nm for the different selected time periods on both days is shown in Table A26. In that  
2471 table also the average values at 380 nm are shown, which are used for a second scaling (see  
2472 below).  
2473 The backscatter profiles are vertically integrated and then the whole profiles are scaled by the  
2474 ratio:



$$\text{AOD}_{1020\text{nm}} / B_{\text{int}} \quad (\text{A1})$$

Here  $B_{\text{int}}$  indicates the integrated backscatter profile.

Note that the wavelength of the ceilometer measurements (1064 nm) is slightly different from the sun photometer measurements (1020 nm), but the difference of the AOD is negligible (typically < 4%).

Table A26 Average AOD at 1020 and 360 nm derived from the sun photometer.

Time	AOD 1020 nm	AOD 360 nm*
18.06.2013, 08:00 - 11:00	0.124	0.379
18.06.2013, 11:00 - 14:00	0.122	0.367
18.06.2013, 14:00 - 19:00	0.118	0.296
08.07.2013, 04:00 - 07:00	0.045	0.295
08.07.2013, 07:00 - 14:00	0.053	0.333
08.07.2013, 11:00 - 19:00	0.055	0.348

\*Average of AOD at 340 nm and 380 nm.

### C) Correction of the aerosol extinction

The photons received by the ceilometer have undergone atmospheric extinction. Here, Rayleigh scattering can be ignored because of the long wavelength of the ceilometer (optical depth below 2 km is < 0.001). However, while the extinction due to aerosol scattering is also small at these long wavelengths it systematically affects the ceilometer signal and has to be corrected. The extinction correction is performed according to the following formula:

$$\alpha_{i,\text{corr}} = \frac{\alpha_i}{\exp\left(-2 \cdot \sum_{z_0}^{z_{i-1}} \alpha_{j,\text{corr}} \cdot (z_j - z_{j-1})\right)} \quad (\text{A2})$$

Here  $\alpha_i$  represent the uncorrected extinction and  $\alpha_{i,\text{corr}}$  represents the corrected extinction at height layer  $i$  (with  $z_i$  is the lower boundary of that height layer). Equation C1 has to be subsequently applied to all height layers starting from the surface ( $z_0$ ). Note that the factor of two accounts for the extinction both paths between the instrument and the scattering altitude (way up and down). The extinction correction is performed at a vertical resolution of 15m. After the extinction correction, the profiles are scaled by the corresponding AOD at 360 nm (see table A26 In Fig. A30 the profiles with and without extinction correction are shown. The extinction correction slightly increases the values at higher altitudes and decreases the values close to the surface. The effect of the extinction correction is larger on 18 June 2013 (up to 12 %).

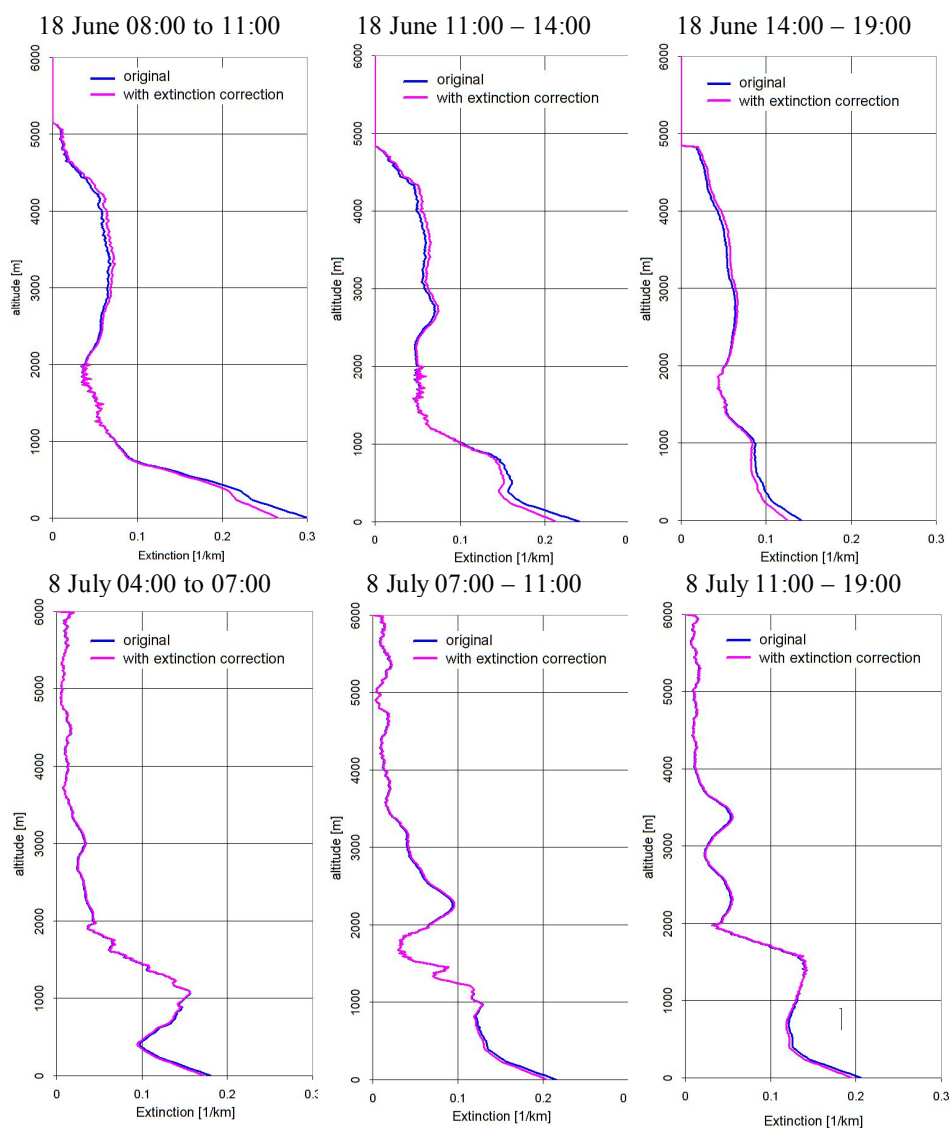


Fig. A30 Comparison of profiles (linear extrapolation below 180 m) without (blue) and with (magenta) extinction correction. Both profiles are scaled to the same total AOD (at 360 nm) determined from the sun photometer.

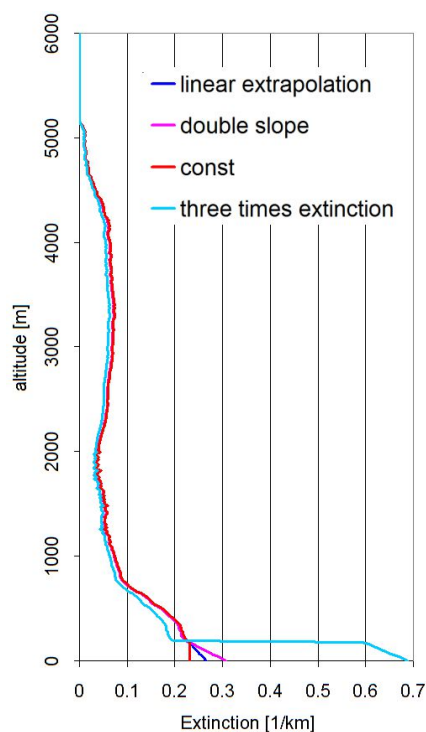


Fig. A31 Aerosol profile (light blue) with extreme extinction close to the surface (below 180 m, the altitude for which the ceilometer is sensitive) extracted for the first period (8:00 – 11:00) on 18 June 2013. Also shown are the profiles extrapolated below 180 as described above.